Fakultät für
Mathematik und Naturwissenschaften
Astroteilchenphysik

BERGISCHE
UNIVERSITÄT
WUPPERTAL

Simulation and measurement of the Forward Beam Monitor detector signal for the KATRIN experiment

DISSERTATION
zur Erlangung des Doktorgrades
doctor rerum naturalium
(Dr. rer. nat.)

Der Fachgruppe Physik vorgelegt von
Norman Haußmann
im April 2019

The PhD thesis can be quoted as follows:

urn:nbn:de:hbz:468-20191009-085446-9
[http://nbn-resolving.de/urn/resolver.pl?urn=urn%3Anbn%3Ade%3Ahbz%3A468-20191009-085446-9]

DOI: 10.25926/8q1y-6752
[https://doi.org/10.25926/8q1y-6752]

Gutachter:
Prof. Dr. Klaus Helbing, Bergische Universität Wuppertal
Dr. Markus Steidl, Karlsruher Institut für Technologie
Datum der Abgabe: 17. April 2019
Datum der mündlichen Prüfung: 06. August 2019

ABSTRACT

The aim of the KArlsruhe TRItium Neutrino (KATRIN) experiment is to measure the effective neutrino mass with a sensitivity of 0.2 eV (90 % C.L.). In order to achieve that, high precision beta spectroscopy from tritium beta decay is performed close to the endpoint of tritium. This requires a high luminosity source. To reach the sensitivity goal, the systematic uncertainties of the experiment, such as the stability of the beta Source, have to be known and kept at a low level. One component to monitor the source stability is the Forward Beam Monitor (FBM). The monitoring is done with two silicon *p*-*i*-*n*-diodes detecting the beta electrons from the Source.

The goal of this thesis is to simulate the expected detector signal of the FBM and compare against first measurements performed with the KATRIN experiment in summer 2018. In order to simulate the Forward Beam Monitor detector signal, a response matrix approach is utilized. Thus, the simulated beta emission spectrum is split into energy and polar angle bins. Each set of events is propagated separately through the experiment. As a beta electron is bent by magnetic fields and undergoes different scattering processes its polar angle and energy can be changed. This leads to a certain probability of beta electrons from an initial energy and polar angle bin to be distributed into different energy and polar angle bins. Probabilities are calculated for the propagation through each component of the experiment, which is essential for the simulation of the FBM detector signal.

The results of the rate simulation and the detected rate of beta electrons agree. The spectral shape and intensity of the beta electrons above 8 keV are also comparable. Additionally, the FBM is able to scan the transversal beta flux distribution on a two-dimensional plane. Therefore, the radial dependency of the rate is simulated, which also agrees with the measured rate.

In this thesis, the different steps that need to be taken in order to simulate the FBM detector spectrum are presented as well the simulation challenges. A new approach into simulating the scattered beta spectrum of the source, which can be utilized in future for neutrino mass analyses and source models, is also presented.

ZUSAMMENFASSUNG

Das Ziel des KArlsruhe TRItium Neutrino (KATRIN) Experiments ist es, die Neutrinomasse mit seiner Sensitivität von 0.2 eV (90 % C.L.) zu messen. Dies entspricht einer um eine Größenordnung erhöhten Sensitivität im Vergleich zu den Vorgängerexperimenten in Mainz und Troitsk. Für dieses Vorhaben wird eine radioaktive Quelle mit einer hohen Aktivität benötigt, deren, aus dem Betazerfall, emittierte Elektronen spektroskopiert werden.

Ein mögliches gasförmiges Isotop mit einem relativ niedrigen Endpunkt (ca. 18.6 keV) ist Tritium. In Karlsruhe, am KIT, steht das Tritium Labor Karlsruhe (TLK) zur Verfügung. Lediglich das TLK besitzt eine Lizenz für die erforderliche Menge Tritium in Deutschland und die Expertise.

Das Tritium wird in eine Quelle mit der Form eines Zylinders geleitet, der am vorderen und hinteren Ende offen ist. An beiden offenen Ausgängen der Quelle sind Turbomolekularpumpen installiert, die das Tritium, das in der Mitte der Quelle eingelassen wird, wieder herauspumpen. Die Tritiummoleküle bewegen sich durch Diffusion, von der Quellmitte zu den Pumpen. Das Tritium kann in der Quelle aufgrund des Betazerfalls ein Elektron emittieren, welches spektroskopiert werden kann. Hierzu wird das Elektron mittels Magnetfeldern aus der Quelle geführt und gelangt durch die Transportsektion in die Spektrometer (Vor- und Hauptspektrometer) und schließlich zum Hauptdetektor.

Eine Hauptkomponente von KATRIN ist der sogenannte MAC-E Filter (Magnetic-Adiabatic-Collimation with an Electrostatic filter), der für die Spektroskopie verantwortlich ist und auch die Sensitivität des Experiments auf die Elektronenenergie definiert. Hierzu wird das Elektron aus einem starken Magnetfeld (ca. 6 T) in ein schwaches Magnetfeld (ca. 3 G) überführt. Dabei ändert sich die transversale Komponente des Elektronenimpulses und wird in die longitudinale Komponente überführt. Hierdurch kann durch Anlegen eines elektrostatischen Potentials Elektronenfilterung durchgeführt werden. Elektronen, die die Filterbarriere überwinden, werden mittels eines Siliziumdetektors gezählt. Der Einfluss einer nicht-verschwindenden Neutrinomasse ist in der Nähe des Endpunktes von Tritium am signifikantesten. Daher wird die Spektroskopie in der Nähe des Tritium-Endpunkts durchgeführt.

Um die anvisierte Sensitivität von KATRIN zu erreichen, muss die Aktivität der Quelle stabil sein und der emittierte Fluss überwacht werden. Hierzu gibt es verschiedenste Systeme, eines davon ist der Forward Beam Monitor (FBM). Der FBM ist in der Transportsektion positioniert und kann mittels zweier Siliziumdetektoren den Elektronenstrom aus der Quelle überwachen und somit Rückschlüsse auf deren Stabilität geben. Die erforderliche Präzision für die Flussmessung

beträgt 0.1 %. Dies erfordert 10^6 detektierte Elektronen für die statistische Unsicherheit und soll in der Grössenordnung von einer Minute erfolgen. Der erwartete Elektronenfluss am Ort des FBM beträgt ca. 10^6 Elektronen pro Quadratmillimeter und Sekunde. Da die für den FBM entwickelte Datenaufnahmelektronik diese Raten nicht verarbeiten kann, werden Dioden mit einer Grösse von ungefähr $0.1\,\mathrm{mm}^2$ verwendet. Der FBM kann mit diesen Dioden jede Position im Elektronstrom erreichen und somit vermessen.

Die Intention dieser Arbeit ist es, das zu erwartende Detektorsignal des FBM zu simulieren, um den Detektor und die einzelnen KATRIN-Komponenten zu verstehen sowie diese Simulationsdaten mit der ersten Messphase im Sommer 2018 zu vergleichen.

Um dies zu erreichen, muss jede Komponente, welche die Elektronen zum FBM führt, untersucht und simuliert werden. Die Elektronen streuen sowohl an den Tritiummolekülen in der Quelle als auch an der Rückwand des Experiments. Ferner werden sie von unterschiedlich starken Magnetfeldern zum FBM Detektor geführt. Diese Effekte können den Polarwinkel und die Energie des Elektrons verändern und dementsprechend auch das detektierte Signal modifizieren.

In dieser Dissertation wird die Interaktion der Elektronen in der Quelle mit den Tritiummolekülen simuliert. Dies wird mittels Monte-Carlo Simulationen auf Grafikkarten realisiert. Desweiteren muss die sogenannte Rear-Section, sprich der hintere Teil des Experiments, simuliert werden. Am hinteren Ende befindet sich eine goldene Rückwand, die es den Elektronen ermöglicht an ihr zurückzustreuen und durch die Quelle in Richtung FBM transmittiert zu werden. In der Transportsektion können Elektronen durch die starken Magnetfelder auch zurückgestreut werden. Ist dies der Fall erreichen sie dementsprechend den FBM nicht. Elektronen, die am FBM ankommen, müssen die Totschicht des Siliziumdetektors passieren bevor sie im sensitiven Volumen detektiert werden. All diese Effekte werden in dieser Arbeit kombiniert und mit den gemessenen Daten aus der Messphase 2018 verglichen.

Die größte Unsicherheit in der Simulation stammt vom Detektor. Die sensitive Fläche des Detektors ist nicht homogen und verändert das detektierte Spektrum je näher Elektronen der (Dioden-)Randfläche kommen. Deswegen muss für das Detektorsignal ein numerisches, auf Messungen aufbauendes, Modell verwendet werden. Gleichwohl stimmen die simulierten Raten im Rahmen der Messgenauigkeit mit den gemessen Daten überein, auch die radiale Abhängigkeit der Rate kann reproduziert werden. Desweiteren kann das detektierte Elektronenspektrum ab 8 keV gut reproduziert werden.

CONTENTS

INTRODUCTION

The KATRIN (KArlsruhe TRItium Neutrino) experiment aims to measure the neutrino mass with a sensitivity of 0.2 eV [KAT05]. In order to improve predecessor experiments by a factor of 10 in sensitivity, a 100 times increase in number of events is required. Therefore, a high luminosity source is used inducing minimal systematic uncertainties, which is combined with a good energy resolution of the experiment. The latter one is performed by a Magnetic-Adiabatic-Collimation with an Electrostatic filter (MAC-E). It achieves an energy resolution of approximately 1 eV at an acceptance angle of about 50.7°. In order to fit the neutrino mass, the electrostatic filter is set to potentials close to the endpoint of tritium, which is the beta decay gas of the experiment. The electrons passing the electrostatic filter are counted by a silicon detector, the Focal Plane Detector (FPD).

As stated, the high luminosity source needs to induce small uncertainties onto the neutrino mass analysis of the experiment. Therefore, it is monitored continuously. One of the monitoring devices is the Forward Beam Monitor (FBM), initially developed at KIT and finalized and commissioned by the Wuppertal group.

The FBM is connected to a pump port in the transport section of the experiment. The transport section removes the tritium from the experiment, so it does not decay at later stages where it would induce background events. The FBM is made of an approximately 2 m long vacuum manipulator, which enables the FBM to be inserted and removed from the beam-line. Additionally, a rotary movement allows the FBM to move on a two-dimensional plane, allowing it to scan any position in the xy-plane of the electron flux, as the electrons are guided from the source to the FPD. The FBM can be positioned with a relative precision of approximately 0.1 mm

The FBM detector board is equipped with two silicon *p-i-n*-diodes to measure the beta rate and the tritium beta spectrum. Additionally, it has a temperature sensor and a Hall-sensor to monitor the magnetic field and the board temperature respectively. The Hall-sensor is also utilized to find the relative position of the FBM to the magnetic field and for comparison to simulation data of the FBM plane.

The goal of this work is to simulate the FBM detector signal for KATRIN tritium operation. In order to do so, the entire experiment from the beta decay in the source to the FBM diodes has to be simulated. The response matrix method is used to do so. The properties of the electron from beta decay, i.e. its energy and polar angle, are transferred bin wise step-by-step through the experiment. That means for instance: electrons from beta decay with an energy close to the endpoint and a large transverse momentum component have a certain probability of scattering off the tritium molecules in the source. If the electron scatters and thereby loses energy and

changes its polar angle it is transferred to a different energy and polar angle bin at the exit of the source. The method is explained in detail in chapter 3. The probabilities of an electron changing its properties is simulated for each section of the experiment leading up to the FBM.

One of the largest efforts for this thesis was to simulate the electron distribution after leaving the Source of KATRIN. While there is an analytical model close to the tritium endpoint for electrons leaving the source available, deep into the spectrum (on the order of several hundred eV to keV away from the tritium endpoint) no model exists. To model the beta spectrum a Monte Carlo approach is utilized in this work. In order to perform these simulations, GPUs (Graphics Processing Units) are used as they speed up the simulation significantly. This model can also be used for neutrino mass analysis and comparisons against analytical models. The method is presented in chapter 4.

The source of KATRIN is shaped like a tube, and electrons leaving the source in the forward direction, are guided through the Transport-Section to the FBM. Thereby, they undergo different magnetic field strengths defining the transmission probability of the electron through the source and also its polar angle at the position of the FBM. The electrons reaching the FBM detector still need to pass the dead-layer of the diode before entering the sensitive volume where they are finally detected.

Electrons, leaving the source in the rear direction have non-negligible probability to scatter off the golden Rear-Wall, and return to the source to be transmitted towards the FBM. The Rear-Wall is the rear-end for electrons in the experiment.

All these different stages need to be considered for the simulation of the FBM signal. In this thesis, all the stages are presented, as well as the expected FBM signal in chapter 5 and its combination in chapter 6.

In summer 2018, the first tritium was injected into the source and the FBM was able to demonstrate its stability and measurement capabilities. The tritium data is analyzed and compared against the simulated rate and spectrum in this work in chapter 7.

CHAPTER 1
NEUTRINOS

Neutrinos have been puzzling scientists for more than a century to date. And still, many questions about their nature are not answered which makes neutrino physics one of the most exciting fields in current research. One open question is the absolute mass of the neutrino, which the KArlsruhe TRItium Neutrino (KATRIN) experiment is attempting to answer.

Further open questions remain: is the neutrino a Dirac or Majorana particle? How did the neutrino influence the structure formation in the early universe?

This chapter is just a summary of the many interesting fields of neutrino physics. It gives a short introduction into a few fields of neutrino physics to the reader to understand the motivation for the KATRIN experiment.

This chapter starts with a brief overview of the history of neutrinos in section 1.1, proceeds with the neutrino in Standard model in section 1.2, the oscillation of neutrinos in section 1.3 and finishes with the hunt for the neutrino mass in section 1.4.

1.1. Brief history

Towards the end of the 19th century radio activity of matter was discovered [Bec01]. This was followed by the discovery in 1903 that radium has three different types of radiation [DSc03], namely the α-, β- and γ-rays, which "differ widely in their power of penetrating matter" [Bec01]. For the β-decay Chadwick and Scott discovered a continuous β-ray spectrum [Cha14; Sco35]. The spectrum measured by Scott is visualized in figure 1.1.

The continuous shape of the spectrum in contrast to the expected mono-energetic shape in the case of two-body decay could not be understood. In 1930 Pauli suggested a third particle, which he initially called "neutron" [Pau30] in an open letter to a group of in Tübingen. The particle is electrically neutral, as the name suggests, and has a spin of 1/2. He also estimated that the particle could have mass on the same order as the electron. Pauli was not overly confident in this theory so he he did not want to publicize his idea immediately. He expected the particle should have been found already if it existed [Pau30].

Nevertheless, the neutron as we know it today was discovered in 1932 [Cha32]. Therefore, Fermi, who picked up Pauli's idea, developed a coherent theory of the nuclear β-decay and called the missing particle "neutrino" [Fer34].

$$ {}^{A}_{Z}X \rightarrow {}^{A}_{Z+1}Y + e^{-} + \overline{\nu}_{\mathrm{e}} \tag{1.1} $$

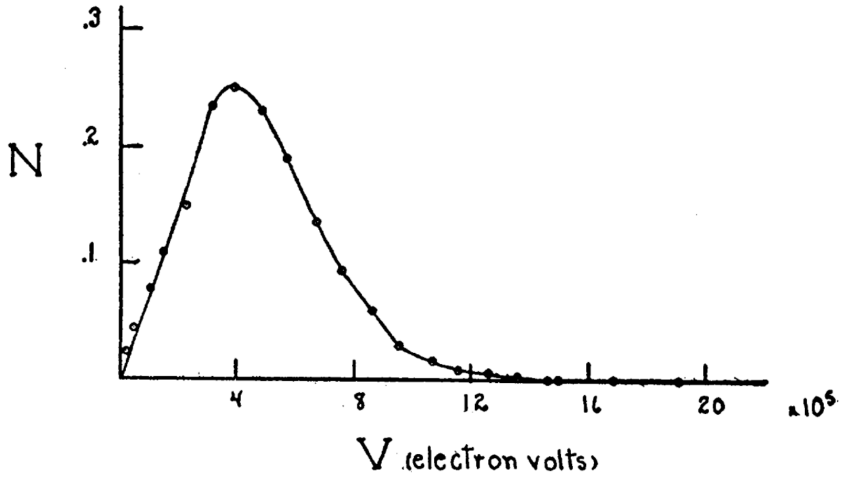

Figure 1.1.: *"Energy distribution curve of the beta-rays" [Sco35] of radium. Here, N denotes the amount of entries per voltage bin V. Figure taken from [Sco35].*

This theory can be seen as the groundwork of the KATRIN experiment. There, X denotes the mother nuclei, Y the daughter nuclei, and $\overline{\nu}_\mathrm{e}$ the anti-neutrino emitted in β^- decay.

It took more than twenty years before the neutrino was discovered by the *Poltergeist* experiment in 1956. It utilized the "anti-neutrino-induced inversion of neutron decay" [Rei+60]:

$$\overline{\nu}_e + p \rightarrow \beta^+ + n. \tag{1.2}$$

During that time it was not known that the neutrino has more than one flavor. The experiment was located at the Savannah River Plant and anti-neutrinos, fission products of a reactor, hit water targets to create a positron and neutron. Both products give gammas in further interactions with a delayed coincidence in the detector. The cross section of this process for anti-neutrinos was found to be $\sigma \approx 10^{-43}\,\mathrm{cm}^2$, which is in agreement with the theoretically expected value.

A few years later, in 1962 evidence for the muon neutrino was found at the Brookhaven Alternating Gradient Synchrotron (AGS). The considered neutrinos were involved in muon production and not electron production "and hence are very likely different from the neutrinos involved in β-decay" [Dan+62]. The tau-neutrino was discovered more recently in this century (in 2001) by the DONUT collaboration at Fermi-lab [Kod+01]. It was originally postulated in 1975 after the discovery of the tauon. Having found three generations of neutrinos agrees with the result found in [Dec+90] with the "number of light neutrino families" [Dec+90] being $N_\nu = 3.01 \pm 0.15(\mathrm{exp.}) \pm 0.05(\mathrm{theor.})$.

1.2. Standard model

The Standard Model (SM) of particle physics describes all known elementary particles and the strong-, weak-, and electromagnetic interactions between them. The particles are grouped into quarks and leptons, and the gauge bosons which are the force carriers. An overview is given in figure 1.2. The fermions, consisting of quarks and leptons, are split into three generations each. Neutrinos are neutral leptons and do not have electrical or color charge and hence only interact weakly, mediated by the Z and W bosons. The helicity of a particle is the projection of the spin onto the direction of the momentum. In 1957 Goldhaber showed that the helicity of neutrinos is negative or "left-handed" [GGS58] and it is "right-handed" for anti-neutrinos.

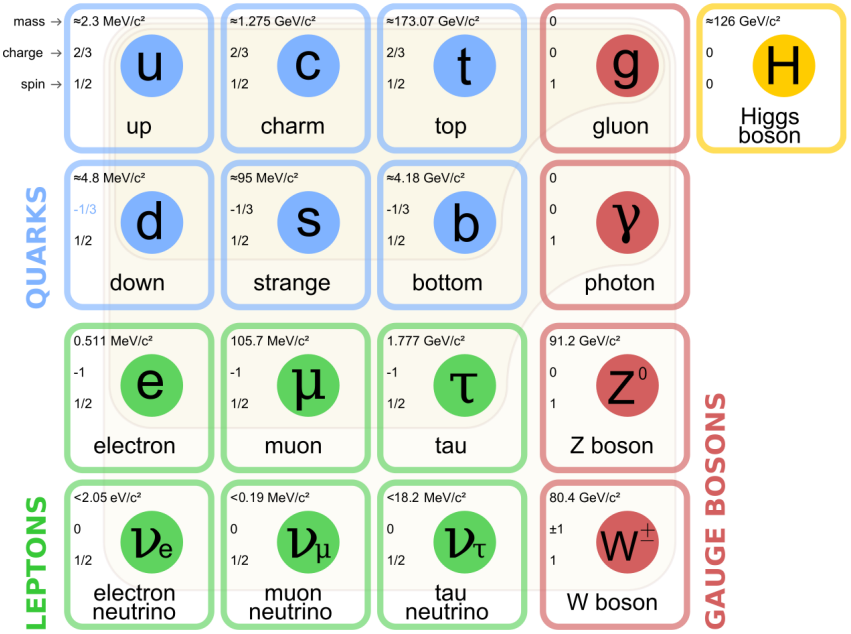

Figure 1.2.: *Visualization of the Standard Model of particle physics. In blue are the different quarks visualized and in green the leptons. The first three columns represent the fermion generations. In red the corresponding gauge bosons are visualized and in yellow the Higgs boson. Figure taken from [Kle14].*

Therefore, neutrinos are massless in the Standard Model of particle physics. However, neutrino oscillations have since been discovered. In order for a neutrino to change its flavor, it needs to experience time and therefore a non-zero mass is required as it would travel at the speed of light otherwise.

1.3. Neutrino oscillation

The discovery of neutrino oscillations, or in other words the transition of one neutrino flavor to another one after some propagation of the neutrino, requires a non-vanishing neutrino mass. In the SM neutrinos do not have mass and therefore neutrino oscillations can be considered as physics beyond the SM. One of the earliest hints towards neutrino oscillations was the solar neutrino problem, which is discussed in the next section.

1.3.1. Solar neutrino problem

An experiment to investigate the solar neutrino flux was the Homestake experiment placed in the Homestake mine. It was built from 1965 to 1967 and the goal was to measure the total neutrino flux above an energy of 0.814 MeV by the inverse beta process:

$$^{37}Cl + \nu \rightarrow e^{-} + ^{37}Ar \tag{1.3}$$

The experiment started in 1970 with a tank of 615 t of perchloroethylene. The resulting argon from inverse beta decay had to be extracted by helium purging and decayed by electron capture with a 35 d half-life which was detected in a gas proportional counter [Dav94] [Bah64]. The experiment found a lack of approximately 2/3 of the expected neutrino flux. Therefore, in 1994, Raymond Davis states: “It is well known that the Homestake average neutrino capture rate is a factor of approximately three below the standard model value”.

The Homestake experiment was superseded by SAGE [Abd+02] and Gallex [Ham+99], which themselves was succeeded by GNO [Alt+05]. These experiments are based on Gallium detectors and confirmed the Homestake results. A complementary measurement was performed at Kamiokande [Fuk+96] which is based on water as the target material and the neutrino electron scattering is observed. They could confirm that the neutrinos originate from the Sun, but also found the disappearance of atmospheric neutrinos travelling through the Earth and therefore claimed to have found neutrino oscillations [Fuk+98].

Since the deficit of solar neutrinos was discovered in all experiments theories emerged explaining the measured signal. One of those theories was the oscillation of neutrinos already predicted in 1967 by Pontecorvo [Pon68]. It assumes that neutrinos can change their flavor and therefore as predecessor experiments were only sensitive to electron neutrinos the flux of neutrinos predicted by the model of the Sun could still be correct.

The confirmation of neutrino oscillations and therefore also the predicted neutrino flux from the Sun was done by the Sudbury neutrino observatory (SNO) in 2001 [Bog+00] [Ahm+02]. The experiment is made of a water Cherenkov detector utilizing 1 kt of heavy water D_2O as a detection medium in a spherical volume. The emitted Cherenkov light, from the emerged particle (e.g. electron) which is traveling faster than the speed of light in the medium, is detected by photo-multiplier tubes (PMT). The advantage of SNO is its sensitivity to all neutrino flavors, by not only being sensitive to the charged current (CC) interaction (gauge boson $W^{\pm}$), but also elastic scattering (ES) and neutral current (NC) (gauge boson Z) interactions:

$$\nu_{\mathrm{x}} + e^- \rightarrow \nu_x + e^- \quad \text{(ES)} \tag{1.4}$$

$$\nu_{\mathrm{e}} + d \rightarrow e^- + p + p \quad \text{(CC)} \tag{1.5}$$

$$\nu_{\mathrm{x}} + d \rightarrow \nu_{\mathrm{x}} + n + p \quad \text{(NC)} \tag{1.6}$$

The obtained results were consistent with the expected flux of neutrinos from the Sun and therefore confirmed neutrino oscillations [Aha+05].

1.3.2. Theory of neutrino oscillations

The interested reader can find a detailed description of the neutrino oscillation theory in [Sue15] and [Jun15]. This section is a short summary of the theory presented in the latter one. The idea of neutrino oscillation was already discussed in the 1960s/1970s [Pon68; BP78]. The different flavor states of a neutrino $|\nu_\alpha\rangle$ ($\alpha = e, \mu, \tau$) can be expressed as a mixture of their mass eigenstates $|\nu_i\rangle$ ($i = 1, 2, 3$) by the Pontecorvo-Maki-Nakagawa-Sakata (PMNS) unitary mixing matrix U:

$$|\nu_\alpha\rangle = \sum_i U^*_{\alpha,i} |\nu_i\rangle \tag{1.7}$$

which can be written as:

$$U = \begin{pmatrix} 1 & 0 & 0 \\ 0 & c_{23} & s_{23} \\ 0 & -s_{23} & c_{23} \end{pmatrix} \begin{pmatrix} c_{13} & 0 & s_{13}e^{-i\delta} \\ 0 & 1 & 0 \\ -s_{13}e^{i\delta} & 0 & c_{13} \end{pmatrix} \begin{pmatrix} c_{12} & s_{12} & 0 \\ -s_{12} & c_{12} & 0 \\ 0 & 0 & 1 \end{pmatrix} \tag{1.8}$$

with $c_{ij} = \cos\theta_{ij}$ and $s_{ij} = \sin\theta_{ij}$. The angles θ_{ij} represent the mixing angles while δ represents the CP violation phase. This matrix can be extended by $diag(1, e^{-i\frac{\alpha_{21}}{2}}, e^{i\frac{\alpha_{31}}{2}})$ with α_{21} and α_{31} being the Majorana CP violation phases in the case that the neutrino is a Majorana particle,

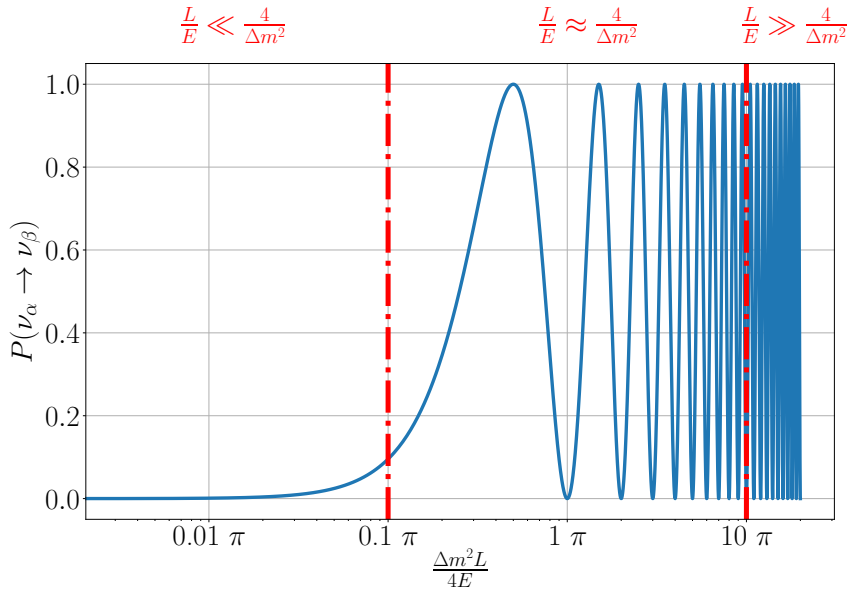

Figure 1.3.: *Visualization of the transition probability of ν_α to ν_β. The amplitude of the transition is assumed to be one. The figure is split into three regions to indicate the influence of* L/E. *Figure inspired from [Zub04].*

i.e. if the neutrino is its own anti-particle [Tan+18]. If we assume a neutrino in the flavor state α, which is produced at the time $t = 0$ and propagates as a free particle in vacuum it can be described by:

$$|\nu_\alpha(t, L)\rangle = \sum_i U^*_{\alpha,i} e^{-i(E_i t - pL)} |\nu_i\rangle \tag{1.9}$$

with t and L being the travelled time and distance. If the mass eigenstates propagate with the same momentum at relativistic energies, this equation can be re-written as:

$$|\nu_\alpha(t, L)\rangle = \sum_i U^*_{\alpha,i} e^{-i\frac{m_i^2}{2E}L} |\nu_i\rangle \tag{1.10}$$

which shows, that the mass eigenstates evolve independently of one another. The probability to observe a neutrino from the initial flavor α in a different flavor β after some travel distance can be calculated as follows:

$$P(\alpha \to \beta) = |\langle \nu_\beta | \nu_\alpha(L) \rangle|^2 = \sum_i \left| U_{\alpha,i} U^*_{\beta,i} \right|^2 + 2\,\mathrm{Re}\left(\sum_{i>j} U_{\alpha,i} U^*_{\beta,i} U^*_{\alpha,j} U_{\beta,j} e^{-i\frac{\Delta m^2_{i,j}}{2E}L} \right) \tag{1.11}$$

with the mass squared difference $\Delta m^2_{i,j} = m^2_j - m^2_i$. Hence, experiments observing neutrino oscillation can only measure the mass squared differences of the mass states and the mixing angles, not the absolute mass.

Simplification with two flavors

A simplified version of neutrino oscillation can be found by considering only the two flavor scenario. The mixing of two flavors and their eigenstates can be described as:

$$\begin{pmatrix} \nu_\alpha \\ \nu_\beta \end{pmatrix} = \begin{pmatrix} \cos\theta & \sin\theta \\ -\sin\theta & \cos\theta \end{pmatrix} \begin{pmatrix} \nu_1 \\ \nu_2 \end{pmatrix} \tag{1.12}$$

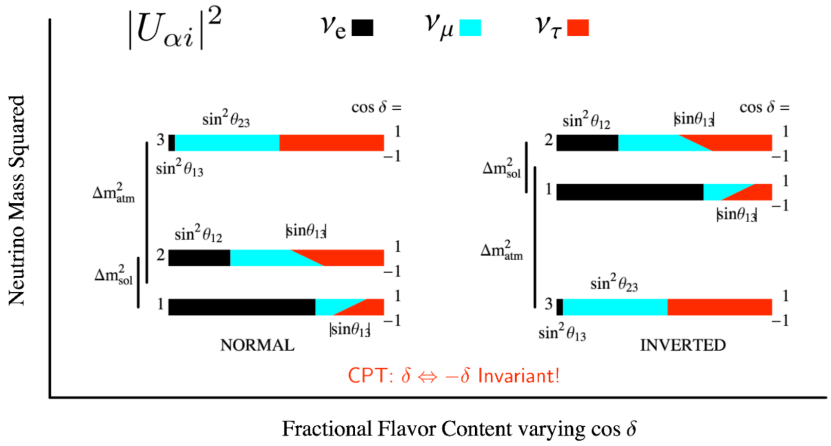

Figure 1.4.: *Visualization of the flavor fraction of the three neutrino mass eigenstates and the cosine of δ - the CP violating phase. Figure taken from [Par08].*

and consequently the transition or oscillation probability simplifies to:

$$P\left(\nu_\alpha \rightarrow \nu_\beta\right) = \sin^2\left(2\theta\right) \sin^2\left(\frac{\Delta m^2 L}{4E}\right). \tag{1.13}$$

Since neutrino oscillations occur, the mixing angle and the mass difference must not vanish. The transition probability depends on the distance to the source of the neutrino:

$$\frac{L}{E} \geq \frac{4}{\Delta m^2} \tag{1.14}$$

A visualization of the transition probability is shown in figure 1.3.

MSW effect

So far, only neutrino oscillations in vacuum are considered. Depending on the position of the Sun, neutrinos have to pass the Sun first and then the Earth in order to investigate the solar neutrino flux. Electron-neutrinos travelling through matter may forward-scatter via charged current interactions. This is called the Mikheyev-Smirnov-Wolfenstein (MSW) effect [MS87] [Wol78]. Since this interaction is not possible for muon- or tauon-neutrinos, the MSW effect modifies the oscillation probability and therefore has to be considered in oscillation experiments.

Measurements

In total there are six free parameters, which can be measured from oscillation experiments. There are three mixing angles θ_{12}, θ_{23}, θ_{13}, the squared mass differences Δm^2_{21}, Δm^2_{32} and the CP violating phase. The various experiments need to be tuned/initially built to measure the respective neutrino oscillation parameters. The current measurement results are listed in table 1.1.

Measurements of the mixing angle θ_{12} and the mass difference Δm^2_{21} are usually performed with solar neutrinos and these parameters are also often referred to as solar parameters as they can be measured by solar neutrino oscillations. However, these parameters can also measured by long baseline reactor-neutrinos.

The parameters θ_{23} and Δm^2_{32} are called atmospheric parameters as these can be determined by atmospheric neutrinos. These are produced by cosmic ray interacting with the atmosphere

parameter	value
$\sin^2\theta_{12}$	$0.307^{+0.013}_{-0.012}$
Δm^2_{21}	$(7.53 \pm 0.18) \cdot 10^{-5}\,\mathrm{eV}^2$
$\sin^2\theta_{23}$	$0.421^{+0.033}_{-0.025}$
Δm^2_{32}	$(2.51 \pm 0.05) \cdot 10^{-3}\,\mathrm{eV}^2$; $(-2.56 \pm 0.04) \cdot 10^{-3}\,\mathrm{eV}^2$
$\sin^2\theta_{13}$	$(2.12 \pm 0.08) \cdot 10^{-2}$
δ	0 to 2π

Table 1.1.: *The current measurements of the six neutrino oscillation parameters. If two numbers are stated, the first one refers to normal mass ordering and the second to inverse mass ordering. A visualization of the mass ordering is shown in figure 1.4. Data taken from [Tan+18].*

of the Earth which creates pions and kaons. The charged pions usually decay into (anti-) muons and (anti-) muon-neutrinos. The (anti-) muons decay further to (anti-) electron-neutrinos and (anti-) muon-neutrinos. The ratio of $\nu_\mu : \nu_e$ is about 2:1. Observing the various baselines of up- and down-going neutrinos of the muon-neutrino flux, can be interpreted as a disappearance of $\nu_\mu \to \nu_\tau$, the parameters can be derived, because no excess of ν_e is observed. This method works for a detector that can identify the flavor and reconstruct the direction. Measurements are also done at accelerators creating a muon neutrino beam and measuring the ν_μ disappearance.

Measurements of the mixing angle θ_{13} has been proven rather difficult because it is the smallest angle in PMNS. It can be measured by long baseline experiments looking for the ν_e appearance channel. This method undergoes several ambiguities: the CP violating phase, the mass ordering/unknown sign of Δm^2_{32} and also matter effects in the Earth. Latest reactor experiments use the $\overline{\nu}_e$ flux to look for the disappearance of $\overline{\nu}_e$ to assess θ_{13}.

Although the squared mass differences can be assessed with neutrino oscillation experiments, their ordering is still unknown. There are three possible mass hierarchies:

1. **Normal** mass ordering: $m_1 < m_2 \ll m_3$ where $\Delta m^2_{32} > 0$
2. **Inverted** mass ordering: $m_3 < m_1 \ll m_2$ where $\Delta m^2_{32} < 0$
3. **Quasi-degenerate** mass ordering: $m_1 \approx m_2 \approx m_3$

A visualization of the first two orderings, which are preferred due to the mass splittings and limits on the absolute neutrino mass, is given in figure 1.4. Measurements of the absolute neutrino mass are explained in the next section.

1.4. Neutrino mass

As stated in section 1.2 concerning the Standard Model, neutrinos were previously assumed to be massless. However, neutrino oscillation requires at least two neutrino mass eigenstates to have mass. There are different mechanisms to extend the Standard Model in order for the neutrino to have mass. One of the simplest models is to add a right-handed neutrino to the model, which would allow mass creation through the Higgs-mechanism [Jun15]. The interested reader can find detailed information on the different mass creation mechanisms in [Bil10].

This section gives an overview of neutrino mass measurements and focuses on measurements of the neutrino mass with a cosmological approach, neutrino-less double beta decay, and utilizing single beta decay, for example in the KATRIN experiment.

1.4.1. Cosmology

The Λ-CDM model, also called the Standard Model of cosmology, describes the evolution of the universe from a hot Big Bang to the cold universe we live in today. It is dominated by cold dark-matter (CDM) and dark energy (Λ). The model of the Big Bang predicts a background of photons still existent today which is measured to be $T_\gamma = (2.7255 \pm 0.0006)\,\mathrm{K}$ [Tan+18]. Besides that, the model predicts a flux of neutrinos of [KZ97]:

$$N_\nu = \frac{3}{11} N_\gamma \tag{1.15}$$

with a temperature of the cosmic neutrino background of:

$$T_\nu = \left(\frac{4}{11}\right)^{1/3} T_\gamma. \tag{1.16}$$

Utilizing the temperature given above and a density of CMB photons of $N_\gamma = (410 \pm 3)\,\mathrm{cm}^{-3}$ [Tan+18] leads to $N_\nu = 112\,\mathrm{cm}^{-3}$ for each flavor at a temperature of $T_\nu = 1.95\,\mathrm{K}$. Nevertheless, due to the small interaction probability of such low energetic neutrinos, the cosmic neutrino background has not been measured so far. The neutrino is the second most abundant particle in the universe after the photon and could be a hot dark matter candidate.

The Planck experiment observes the cosmic microwave background anisotropy of the universe with high precision. By fitting the Λ-CDM model to the data and including external data from various experiments, a summed neutrino mass can be derived [Agh+18]:

$$\sum m_\nu < 0.12\,\mathrm{eV} \qquad (95\,\%\ \mathrm{C.L.}) \tag{1.17}$$

This result is highly model-dependent.

1.4.2. Neutrino-less double beta decay

This section gives a brief summary of neutrino less double beta decay. It is based on reference [Rod11] where the interested reader can find additional information.

The ordinary double beta decay ($2\nu\beta\beta$) is a transition of a nucleus into another nucleus with an increase on the proton number by two, the emission of two electrons and electron anti-neutrinos.

$${}^{A}_{Z}X \rightarrow {}^{A}_{Z+2}Y + 2e^- + 2\overline{\nu}_e \tag{1.18}$$

The half-life of this process is in the order of 10^{19} to 10^{21} years and the process is allowed in the Standard Model in the cases in which single beta decay is energetically forbidden. The nucleus, compared to its mother nucleus with an increased atomic number by one, needs to have a smaller binding energy to prevent single beta decay. The nucleus with an increased atomic number by two needs to have a larger binding energy. Some nuclei, which can be used for double beta decay experiments, are for instance ^{48}Ca, ^{76}Ge, and ^{136}Ge. In this process the spectrum of the two emitted electrons is continuous as the anti-neutrinos also carry away part of the decay energy.

Neutrino-less double beta decay works analogously to the normal beta decay. The initial nucleus transitions into a nucleus with an atomic number increased by two and two electrons.

$${}^{A}_{Z}X \rightarrow {}^{A}_{Z+2}Y + 2e^- \tag{1.19}$$

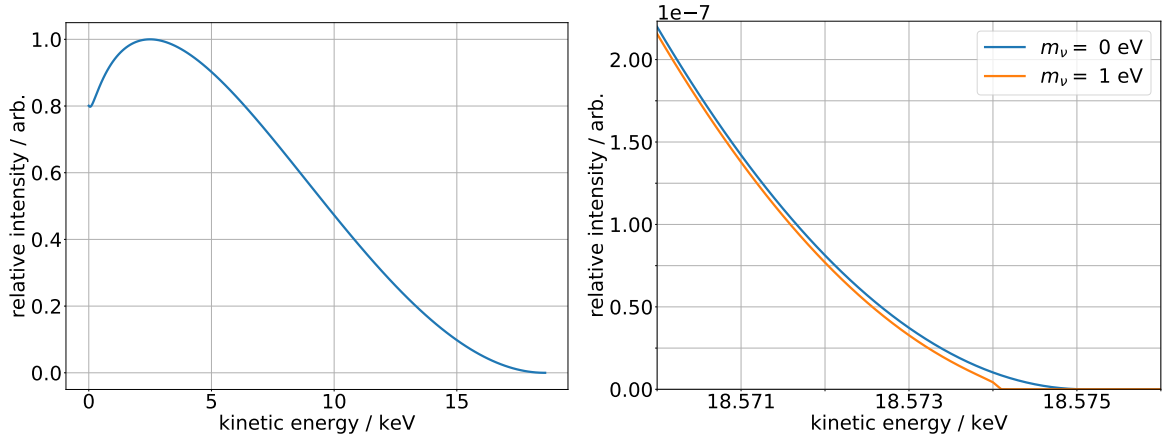

(a) Full spectrum. **(b)** Zoom on endpoint.

Figure 1.5.: *In the left figure (a) the full tritium spectrum with an endpoint of 18.575 keV and zero neutrino mass is visualized. In the right figure (b) the same spectrum close to the endpoint and an additional spectrum with a neutrino mass of 1 eV is visualized.*

However the lepton number conservation is violated as it is increased by two by creating no electron anti-neutrinos. This process can occur if a Majorana neutrino is exchanged at the vertex, i.e. the neutrino is its own anti-particle and the helicity flips. In this decay chain, the electrons carry away all the decay energy Q and instead of a continuous spectrum, a sharp line should be detectable.

So far no neutrino-less double beta decay has been observed. However, limits on the neutrino mass can be set utilizing the half-life of neutrino-less double beta decay [Ago+16]:

$$\left(T^{0\nu}_{1/2}\right)^{-1} = G^{0\nu}(Q_{\beta\beta}, Z) \left|M^{0\nu}\right|^2 \langle m_{\mathrm{ee}}\rangle^2 \tag{1.20}$$

with the phase-space $G^{0\nu}(Q_{\beta\beta}, Z)$, atomic number Z, and $M^{0\nu}$ the nuclear matrix element. The effective Majorana mass $\langle m_{ee}\rangle$ is given as:

$$\langle m_{\mathrm{ee}}\rangle = \left|\sum_{i=1}^{3} U^2_{\mathrm{ei}} m_i\right| . \tag{1.21}$$

Currently, Gerda [Ago+18] and KamLAND-Zen [Gan+16] set the best limits on the effective Majorana mass with (90 % C.L.):

$$\begin{aligned} 120\,\mathrm{meV} < \langle m_{\mathrm{ee}}\rangle < 260\,\mathrm{meV} \qquad & (\mathrm{Gerda}) \\ 61\,\mathrm{meV} < \langle m_{\mathrm{ee}}\rangle < 165\,\mathrm{meV} \qquad & (\mathrm{KamLAND-Zen}) \end{aligned}$$

1.4.3. Single beta decay

Single beta decay is based on Fermi's theory stated in section 1.1. It is a three-body decay with a mother nucleus decaying into the daughter nucleus under emission of an electron/positron and anti-neutrino/neutrino. The electron spectrum for tritium beta decay, following Fermi's golden

rule, is given as [KAT05]:

$$\frac{dN}{dE} = C \cdot F(Z,E)p(E+m_e)(E_0-E)\sqrt{(E_0-E)^2-m_\nu^2}\cdot\Theta(E_0-E-m_\nu) \tag{1.22}$$

where E is the kinetic energy, m_e the mass and p the momentum of the electron. The endpoint energy E_0 refers to the endpoint energy with a zero neutrino mass. The term $F(Z,E)$ denotes the Fermi function which takes the Coulomb interaction into account and is independent of the neutrino mass. Additionally, the term C is also independent of the neutrino mass (an explanation and derivation of the specific formula for tritium can be found in [Dre+13b] and [OW08]), it is given as :

$$C = \frac{G_F^2}{2\pi^3}\cos^2\theta_C\,|M|^2 \tag{1.23}$$

with G_F as the Fermi constant, θ_C the Cabbibo angle and the nuclear matrix element M. The Heaviside function Θ ensures energy conservation. A visualization of the tritium beta spectrum with an endpoint energy of 18.575 keV is given in figure 1.5. On the left side the entire spectrum with a zero neutrino mass is visualized. On the right side, the spectrum is zoomed to the endpoint, with a comparison of the zero neutrino mass spectrum and the spectrum with 1 eV neutrino mass. From a fit of the endpoint and amplitude, the neutrino mass can be derived. In the experiment one additional fit parameter has to be taken into account which is the background. In tritium beta decay experiments only the endpoint region is investigated because the distortion of the spectrum is statistically the most significant in that region.

The ansatz of single beta decay is referred to as model independent as the kinematics of beta decay are well known and the absolute mass is independent of the neutrino being a Dirac or Majorana particle. Given the KATRIN experiment energy resolution, the mass splittings are too small to be observed, and the neutrino mass squared as the incoherent sum of the mass eigenstates is measured:

$$m_{\nu_e}^2 = \sum_i |U_\mathrm{ei}|^2\, m_i^2 \tag{1.24}$$

weighted by the PMNS matrix elements. The KATRIN experiment utilizes the single beta decay to derive the absolute neutrino mass or to set a new limit of $m_\nu = 0.2\,\mathrm{eV}$ (90 % C.L.). Predecessor experiments in Mainz [Kra+05] and Troitsk [Ase+11] set the current best limits on the neutrino mass with (95 % C.L) from direct detection:

$$m_\nu \leq 2.3\,\mathrm{eV} \qquad \text{(Mainz)} \tag{1.25}$$

$$m_\nu \leq 2.2\,\mathrm{eV} \qquad \text{(Troitsk)}. \tag{1.26}$$

In order to improve the sensitivity to a neutrino mass lower by a factor of ten, a one-hundred times larger amount of detected events is required for KATRIN compared to its predecessors.

CHAPTER 2
THE KATRIN EXPERIMENT

Predecessor experiments to KATRIN in Mainz and Troitsk have set an upper limit of the neutrino mass in the order of 2 eV [Kra+05; Ase+11]. The goal of the KArlsruhe TRItium Neutrino (KATRIN) experiment is to enhance the sensitivity to the neutrino mass by one order of magnitude down to 0.2 eV [KAT05] with a 90 % confidence level or with the discovery potential to a neutrino mass of approximately 0.35 eV [KAT05]. In order to achieve that, the statistics of data taking needs to be increased by a factor of 100 while keeping the systematic uncertainties of the experiment at a low level.

The experiment is based in Karlsruhe at the former "Forschungszentrum", today called the "Karlsruhe Institute of Technology" (KIT). The location in Karlsruhe has many advantages. It is close to Mainz where one of the predecessor experiments was located and a lot of expertise in such kind of experiments exists. Additionally, the Tritium Laboratory Karlsruhe (TLK) is part of KIT and is capable of handling the amount of tritium required to achieve the sensitivity goal of KATRIN in a short measurement time (5 yr).

This chapter gives an introduction to the essential hardware components and the physics of the KATRIN experiment. An overview over the approximately 70 m long beam-line is given in figure 2.1. The interested reader can find more information about the single components given in the references of each section and generally in the references [KAT05; Dre+13a] and [Are+18].

2.1. Measurement principle

As stated in the previous chapter, single beta decay experiments focus on the shape of the beta spectrum close to the endpoint as the impact of a non-vanishing neutrino mass is statistically most significant in that region. However, on the downside, detecting beta electrons in the endpoint region is the least likely as electrons need to carry almost all of the decay energy. The probability to detect and electron close to the endpoint is on the order of $\approx 10^{-13}$ for a single tritium atom and therefore a Source with a strong luminosity is essential. Additionally, the acceptance or detection probability of the experiment should be large and ideally all isotropically emitted electrons should be detected. A large acceptance of beta electrons is achieved if a Magnetic-Adiabatic-Collimation with an Electrostatic filter (MAC-E) is utilized.

In order to measure the neutrino mass, beta spectroscopy is performed. The basic principle

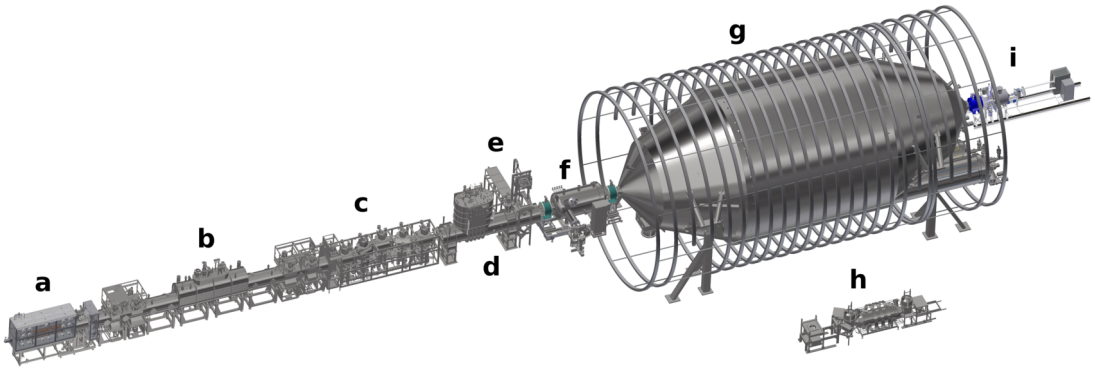

Figure 2.1.: *Visualization of the KATRIN beam-line and its main components. The components: the Rear-Section (RS) (a), the Windowless Gaseous Tritium Source (WGTS) (b), the Differential Pumping Section (DPS) (c), the Cryogenic Pumping Section (CPS) (d) with the attached Forward Beam Monitor (FBM) (e), followed by the two spectrometers (f) and (g) indicating the Pre- and Main-Spectrometer (PS/MS). Attached to the MS is the Focal Plane Detector (FPD). The former Mainz setup is now utilized as the Monitor-Spectrometer, (MoS) (h).*

is as follows (refer to figure 2.1): electrons emitted by the beta decay of tritium in the WGTS are magnetically guided through the Source and Transport-Section (TS). The TS consists of two main components, namely the DPS and CPS. As the WGTS is not blocking tritium from leaving the Source, the tritium is also moving towards the main detector and could therefore decay anywhere in the experiment, even in the spectrometers. This is prevented in the TS as the tritium is pumped from the system. Afterwards, electrons are spectroscopically analyzed by the MAC-E (PS and MS) filter and only electrons that overcome an electrostatic barrier are finally detected at the Focal Plane Detector (FPD). The MAC-E filter defines the energy resolution of the experiment and the FPD counts the emitted betas close to the endpoint of tritium. Therefore, by shifting the electrostatic barrier, the KATRIN experiment measures the integrated beta spectrum close to the tritium endpoint. The MAC-E filter principle is explained in the next section.

2.2. MAC-E filter

The KATRIN experiment consists of three MAC-E filters in total. One is the Pre-Spectrometer (PS) and removes beta electrons with an energy lower than 18.3 keV to reduce background in the Main-Spectrometer (MS). The MS serves as the essential component for beta spectroscopy with high precision. An electrostatic barrier is shifted in the MS to scan through the beta spectrum. Additionally, the third MAC-E filter is utilized in the Monitor-Spectrometer (MoS). The MoS was situated in Mainz and was used to measure the neutrino mass limit set by the Mainz group. The MoS is used in KATRIN to monitor the stability of the electrostatic barrier in the MS. The MAC-E filter principle started its development in the 1970s and was refined over the years ([HH76; BPT80; KR83]) before finally being used in the experiments that set the current upper limit on the neutrino mass in Troitsk [LS85] and Mainz [Pic+92].

A visualization of the MAC-E filter principle is given in figure 2.2. In this figure, the electrons enter the spectrometer from the left, originating from the Source. The electrons follow their respective magnetic field lines if they are guided adiabatically. That means, electrons enter-

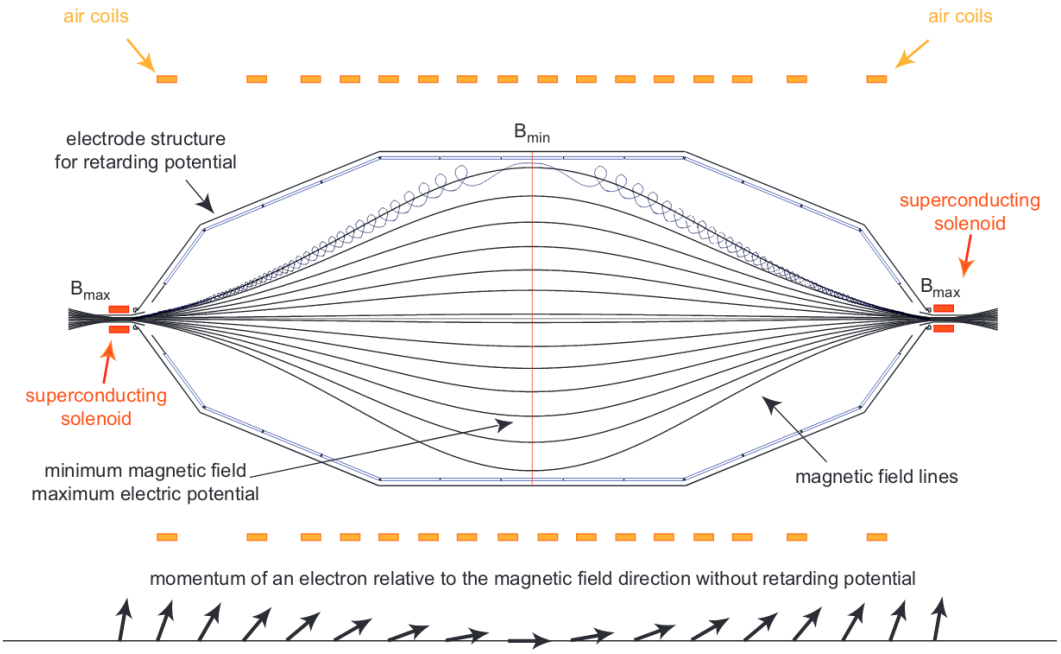

Figure 2.2.: *Visualization of the MAC-E filter principle. Electrons follow their respective magnetic field line on a cyclotron orbit. The transverse momentum component decreases while the longitudinal component increases accordingly. In the analyzing plane, the maximum electric field is applied where almost all momentum of the electron is transferred to the longitudinal component. Figure taken from [Hug08].*

ing from the left undergo a large magnetic field B_S[1], which drops along the travel of the electron to the analyzing plane where the magnetic field is at its minimum. The maximum magnetic field in nominal KATRIN settings is 6 T and the minimum field is 3 G ($3 \cdot 10^{-4}$ T). The MAC-E filter principle only works if the gradient of the magnetic field is small for one cyclotron motion of the electron. The magnetic moment of the electron is constant:

$$\mu = \frac{E_\perp}{B} = \text{const.} \tag{2.1}$$

and therefore the electron travels adiabatically. While the electron travels towards the analyzing plane, the transverse momentum component decreases and the longitudinal component increases. In the analyzing plane, the electron has transferred almost all of its momentum into its longitudinal component of the momentum and at this stage the maximum electrostatic potential is applied to perform filtering. Electrons overcoming the electrostatic barrier travel towards the detector as visualized on the right side of the figure, the others are reflected in front of the maximum magnetic field B_{max} and travel back towards the Source. For a symmetric setting of the magnetic field, i.e. $B_S = B_{\text{max}}$ all electrons that overcome the electrostatic barrier are guided towards the detector. If $B_{\text{max}} > B_S$ still some of those electrons can be reflected by the so-called magnetic mirroring effect:

$$\sin\theta_{\text{max}} = \sqrt{\frac{B_S}{B_{\text{max}}}} \tag{2.2}$$

[1] It is called B_{max} in the figure. The magnetic field strength is not necessarily equal for both super-conducting magnets as stated in the figure, therefore the magnet at the entrance is called B_S in this section and B_{max} at the detector side.

for θ being the polar or also called pitch angle of the electron. This effect increases the transverse momentum of the electron for an increasing magnetic field until it flips in longitudinal direction and returns towards its origin. For KATRIN the so-called acceptance angle is $\theta_{\max} = 50.77°$, which is calculated by comparing the magnetic field in the Source of KATRIN and the maximum magnetic field along the beam-line. In other words, out of the polar angle range in forward direction, 0° to 90°, for electrons in the Source about 1/3 can be detected. Electrons with larger polar angle are excluded from data taking because they have a larger systematic uncertainty and lose more energy due to synchrotron radiation while also having a larger scattering probability.

As stated before, not all of the transverse component of the momentum can be transferred to the longitudinal component, this induces some uncertainty on the resolution of the energy of the electron. This effect defines the energy resolution of the MAC-E filter. In case of KATRIN and the MS it is:

$$\Delta E = \frac{B_{\min}}{B_{\max}} \cdot E_0 = 0.93\,\mathrm{eV} \tag{2.3}$$

for nominal KATRIN settings, i.e. $B_{\max} = 6\,\mathrm{T}$ and $B_{\min} = 3.6\,\mathrm{T}$, and an electron energy of $E_0 = 18.6\,\mathrm{keV}$. The energy resolution also defines the sharpness of the transmission function of the spectrometer, which is given by:

$$T(E, qU) = \begin{cases} 0 & E - qU < 0 \\ \frac{1-\sqrt{1-\frac{E-qU}{E}\cdot\frac{B_{\mathrm{s}}}{B_{\min}}}}{1-\sqrt{1-\frac{\Delta E}{E}\cdot\frac{B_{\mathrm{s}}}{B_{\min}}}} & 0 \leq E - qU \leq \Delta E \\ 1 & E - qU > \Delta E \end{cases} \tag{2.4}$$

with the energy E of the electron, q the charge of the electron and U the retarding potential.

2.3. Main components

Detailed information on all the components can be found in the design report of KATRIN [KAT05]. This section focuses on components of KATRIN which are essential for this thesis.

The goal of this work at hand aims to simulate the electron flux and also the beta spectrum measured with the Forward Beam Monitor. The FBM is located in the Transport-Section, right before the energy filtering components (the spectrometers), and utilizes *p-i-n*-diodes to measure the electron flux from the Source and to monitor its stability. All components required for a good understanding of the different chapters of this thesis and the simulation of the FBM detector signal are introduced in this section.

2.3.1. WGTS

The main body of the Windowless Gaseous Tritium Source (WGTS) consists of a cylindrical tube of 10 m length with radius of 90 mm. Tritium is injected in the center through 250 capillaries, each with 2 mm diameter. The tritium moves by diffusion towards the pumping ports, where it gets pumped out by 12 turbomolecular pumps. This is extended by the pumping sections: the Differential Pumping Section stage 1 which increases the length of the WGTS to 16 m with a total gas flow reduction factor of about 10^2 [Höt12]. The pumped-out gas is collected and re-injected. This concept is advantageous as no windows are blocking the electrons from leaving the Source. A window would induce uncertainties on the electron energy due to their energy loss by penetrating the window.

Since the tritium moves by diffusion a larger density at the point of injection is expected compared to that at the pumping ports. This has to be taken into account as electrons have a

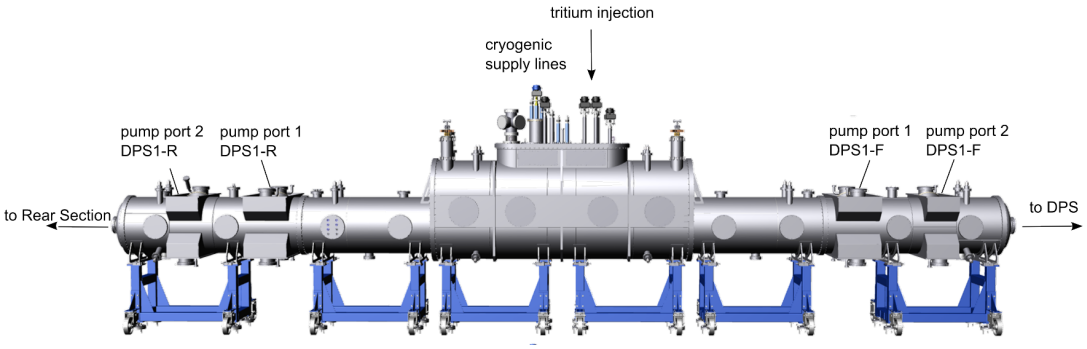

Figure 2.3.: *Visualization of the Source of the KATRIN experiment. The tritium is injected in the center of the Source and moves by diffusion to the DPS, connected to the right side, and to the RS on the left. Figure taken from [Kuc16].*

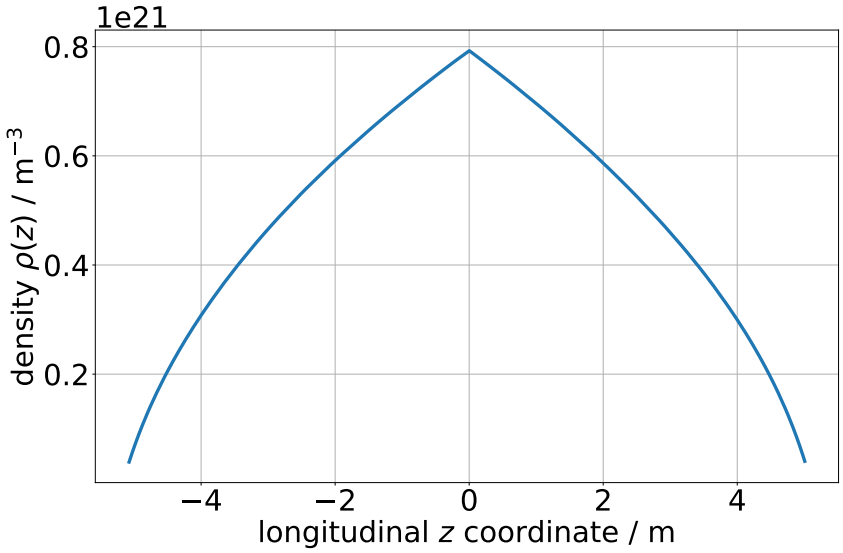

Figure 2.4.: *Example of the tritium density distribution along the z-axis.*

larger probability to stem from tritium close to the injection point compared to the pumping ports. Therefore, the probability of electrons from the center to interact with the gas inside of the Source is larger as they have to travel a further distance to reach the exit of the Source. An example density distribution is given in figure 2.4.

It is essential to have a stable column density ρd, which is defined as tritium molecule density integrated along the longitudinal axis z. For KATRIN the nominal value is $5 \cdot 10^{21}\,\mathrm{m}^{-2}$ and it must not fluctuate by more than a factor of $2 \cdot 10^{-3}$ [KAT05].

The total luminosity $L_{\mathrm{tot.}}$ of the Source can be calculated utilizing the half-life of tritium which is $(4500 \pm 8)\,\mathrm{d}$ [LP00], and the tritium purity ϵ_{T}, which is 95 % in the nominal KATRIN configuration, as follows:

$$L_{tot.} = \epsilon_{\mathrm{T}} \cdot 2\rho d \cdot \lambda_{\mathrm{tritium}} \cdot A_{\mathrm{eff}} = \epsilon_T \cdot 2\rho d \cdot \frac{\ln(2)}{T_{1/2}(\mathrm{tritium})} \cdot A_{\mathrm{eff}} = 1.1 \cdot 10^{11}\,\mathrm{s}^{-1} \tag{2.5}$$

with the effective area A_{eff}. The factor of 2 arises because the column density refers to the amount of particles (molecules) in the Source and the tritium molecule consists of two tritium atoms. The emitted electrons are guided by their respective magnetic field lines towards the exit of the Source into the Differential Pumping Section (DPS) or Rear-Section (RS).

Even though the column density might be stable on the required level, it is essential to monitor the tritium purity. This is done using a LAser RAman measurement system (LARA) [Sch+11]. As the FBM is supposed to measure the Source stability both input parameters are directly proportional to the measured rate and are therefore essential to understand the measured rate and spectrum.

2.3.2. Transport- and Rear-Section

The guided electrons enter either the Rear-Section in rear direction of the experiment or the Transport-Section in forward direction. The Transport-Section consists of the DPS and CPS, both are required to reduce the tritium flux in the experiment while the electrons are magnetically guided through these sections. In the Rear-Section, the electrons are guided until they hit the Rear-Wall, the rear-end of the experiment for beta electrons. Both sections play a crucial role in the analysis/interpretation of FBM measurements and are introduced in this section.

2.3.2.1. Rear-Section

The interested reader can find detailed information about the Rear-Section in [Bab14]. If not stated differently, this section is based on that reference.

In figure 2.5 the Rear-Section components are visualized. Its main components are the RS electron-gun, the Rear-Section magnet (RSCM) and the Rear-Wall. Electrons leaving the Source towards the Rear-Section impinge on the Rear-Wall. This offers an ideal possibility to install a detector system to monitor the Source activity. It is realized with a beta-induced X-ray spectroscopy detector (BIXS) detecting bremsstrahlung and X-rays. The detector is situated close to the gold plated Rear-Wall (which has a large atomic number Z). Additionally, the Rear-Wall can be used to set the plasma potential in the Source and can be irradiated with UV light to produce low-energy electrons to neutralize positive ions in the Source. This method was also used for first light measurement of the experiment as the electrons were guided through the entire KATRIN setup [Hac17].

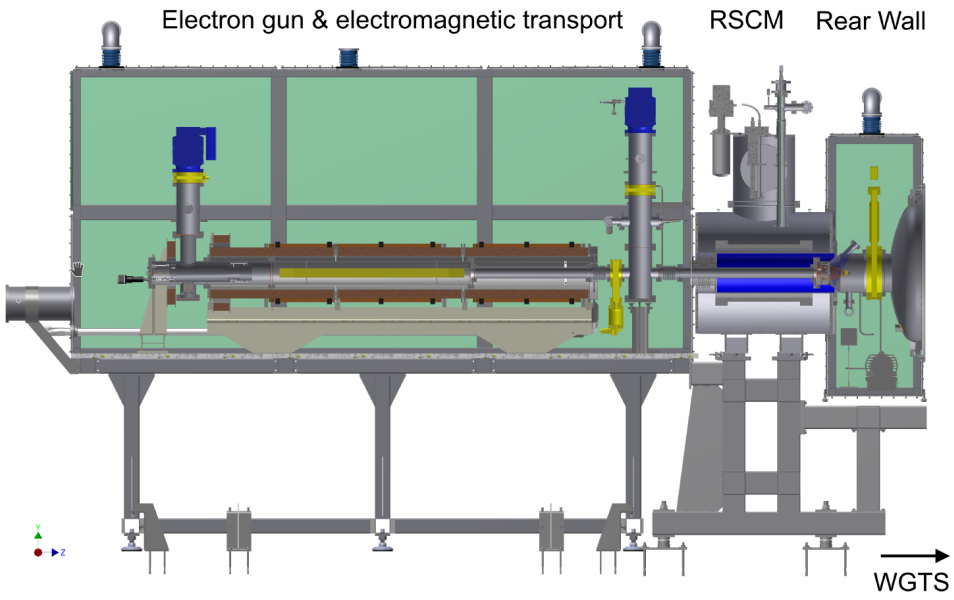

Figure 2.5.: *CAD drawing of KATRIN's Rear-Section. To the right side, the WGTS is connected. Figure taken from [Bab14].*

The Rear-Wall is supposed to terminate the electron and ion flux from the Source, however electrons may scatter off the Rear-Wall and travel again through the Source into the Transport-Section. Although, this process is unlikely to occur for electrons close to the tritium endpoint - which are of of interest for neutrino mass fitting - they cannot be neglected for the simulation of the FBM rate and spectrum.

If this thesis refers to the Rear-Section it usually also includes the rear part of the Source called Differential Pumping Section 1 Rear, which is visualized in figure 2.3 on the left side. This is done in order to differentiate between the tritium beta decay section and the electron transporting sections of the experiment. A visualization of the magnetic field in the Rear-Section and the components is shown in appendix A.II. This work focuses on data measured during the First Tritium measurement phase. During that phase the Rear-Section magnet was not turned on and the valve V0 was closed and therefore defined the rear-end of KATRIN, it is right in front of the Rear-Wall as shown in appendix A.III. Hence, electrons scatter of the valve instead of the Rear-Wall and the low magnetic field due to the turned off magnet decreases the probability of electrons re-entering the Source.

2.3.2.2. Transport section

The Transport-Section consists of the Differential Pumping Section (DPS) (also referred to as Differential Pumping Section 2 Forward), the Cryogenic Pumping Section (CPS), and as defined in this thesis at hand, the forward component of the Source called Differential Pumping Section 1 Forward (refer to figure 2.3). The purpose of the Transport-Section is to reduce the tritium and ion flux in the system since neither one of these must enter the spectrometers. Otherwise it would increase the background rate of the experiment and therefore decrease the sensitivity of KATRIN on the neutrino mass. In order to achieve that, the flux of tritium at the entry of the spectrometers has to be reduced by 14 orders of magnitude in the Transport-Section [Dre+13a]. A detailed overview of the components is given in [Hac17].

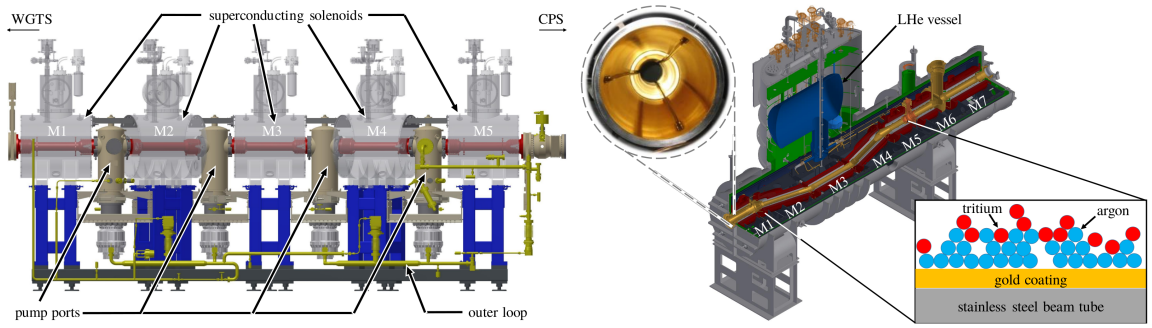

(a) Differential Pumping Section. **(b)** Cryogenic Pumping Section.

Figure 2.6.: *(a) Visualization of the beam-tube and magnets of the DPS. (b) Visualization of the CPS and its gold coated inner surface. Figures taken from [Hac17].*

The DPS consists of four turbomolecular pumps in order to remove the tritium. Additionally, five magnets provide the magnetic field to guide electrons adiabatically through a chicane. The neutral tritium gas does not follow the magnetic field lines and therefore the chicane serves as a barrier for the neutral gas as no direct path is available towards the spectrometers. The DPS is visualized in figure 2.6 (a) from the side view. The CPS has a similar chicane as the DPS visualized in figure 2.6 (b).

The beam-tube elements of the CPS (2 to 3) are cooled down to 3 K and a thin layer of argon frost is prepared on the gold coated surface to cryosorb the tritium [Hac17]. The CPS also has a chicane in order to achieve the desired tritium flux reduction of $> 3 \cdot 10^7$ [Dre+13a]. In pump port 2, located between beam-tube M6 and M7, of the CPS. The Condensed Krypton Source (CKrS) can be inserted into the upper part of the port. The FBM is inserted in the horizontal direction at the same pump port. The FBM and the Condensed Krypton Source cannot be inserted at the same time into the CPS.

As stated before, ions must not enter the spectrometers as they induce background. They follow the magnetic field lines and cannot be pumped out. Therefore, ring electrodes are installed in the Transport-Section. These remove the ions by $\vec{E} \times \vec{B}$ drift as they hit the surface of the Transport-Section where they are neutralized.

Throughout the Transport-Section the magnetic field strength varies. This defines if electrons can reach the FBM, as well as the pitch angle of electrons at the FBM which influences the reflection probability off the FBM detector. Therefore, it is essential for this work to investigate the radial dependent magnetic field strengths as well as the field strength at the location of the FBM. Additionally, the Transport-Section defines the mapping of the FBM detector location to the Source.

2.3.3. Focal Plane Detector

The FBM is able to scan the electron flux (refer to next section) and therefore needs to be moved to different positions throughout the flux tube. Thus, at the same time the FBM blocks electrons from reaching the FPD, which is the final component of the KATRIN experiment to measure beta electrons, and a shadow of the FBM can be seen on the FPD. This can be used during commissioning and calibration to estimate the relative position of the two detectors.

The pixel-wise structure creates a shadow like structure on the FPD detector if components

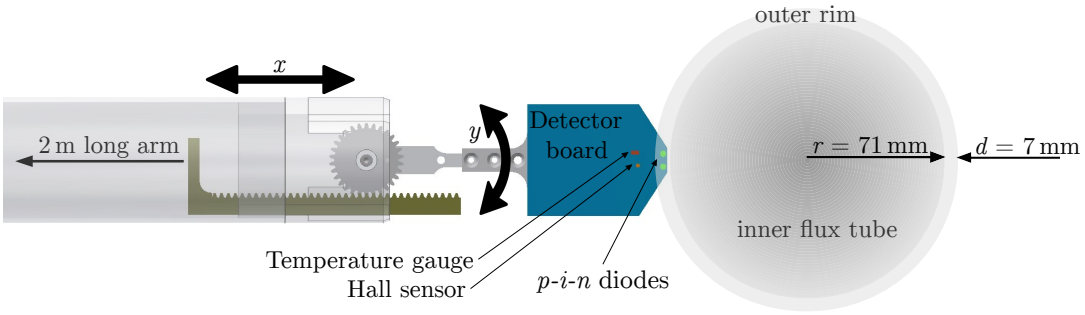

Figure 2.7.: *Visualization of the Forward Beam Monitor front end located in the outer rim of the magnetic flux tube. Figure adapted from [Are+18].*

are blocking the electron flux from the Source. The FPD consists of 148 silicon *p-i-n*-diode pixel, each with a size of 44 mm^2. The total diameter of the FPD is 90 mm [Ams+15]. The FPD is attached to the end of the Main-Spectrometer, therefore electrons that are able to pass the electrostatic filter are guided to the FPD where they have to be counted. Hence, the FPD needs a high detection efficiency. The measured detection efficiency is in the order of 95 % [Ams+15].

2.3.4. Forward Beam Monitor

The task of the Forward Beam Monitor (FBM) is to verify the Source stability in order to perform neutrino mass analysis with the FPD with high sensitivity. Therefore, it needs to achieve 1 ‰ precision in approximately 1 min measurement time. To achieve this statistical precision, 10^6 events have to be detected. During nominal KATRIN operation approximately 10^6 electrons per second and square millimeter are expected at the location of the FBM (compare section 5.3.2 and 7.1). Therefore, theoretically, one second integration time is sufficient to achieve the precision with a 1 mm^2 detector.

Since it is of interest to also measure deeper into the tritium beta spectrum to observe Source effects, *p-i-n*-diodes were chosen with an energy resolution of about 2.5 keV FWHM. The data acquisition can handle an electron rate of approximately 10^4 to 10^5 events per second without being dominated by pile-up events. Pile-up occurs if two, or more, electrons hit the detector at the same time, that is within the integration time of the detector for one event. Those electrons are counted as a higher energetic event. Therefore, in nominal KATRIN configuration, smaller *p-i-n*-diodes need to be used with an effective size of about 0.1 mm^2. During First Tritium, the tritium purity was 0.5 % and therefore larger diodes with an effective size of approximately 1.1 mm^2 were used.

The FBM is equipped with two *p-i-n*-diodes, which are supposed to be situated in the outer-rim. This area is in between the 229 T cm^2 and 191 T cm^2 magnetic flux at nominal KATRIN settings with 100 % magnetic field setup. The latter one maps the Source onto the FPD and must not be covered by the FBM. The magnetic flux Φ is defined as:

$$\Phi = \int BdA = \text{const.} \tag{2.6}$$

where B denotes the magnetic field and A the area. The flux, mapping the Source to the FPD with 191 T cm^2, covers almost all of the Source, except for the mentioned outer-rim of ≈ 4 mm, which translates to 7 mm at the location of the FBM as visualized in figure 2.7. Nevertheless, during the past measurement phases it appears that the outer-rim is smaller than expected,

probably due to collisions of the flux in the Transport-Section with the beam-tube wall. Therefore, the existence of the rim needs to be verified with electron gun measurements to find the optimal position of the FBM.

A detailed description of the FBM hardware can be found in [Ell19]. The hardware consists of a 2 m long vacuum manipulator that allows the FBM to move to the inside of the CPS. It is able to scan the entire flux by moving in horizontal x and vertical y directions. The movement along the horizontal axis is done utilizing the mentioned vacuum manipulator. The vertical movement is in fact a rotary movement indicated by the FBM front-end (compare figure 2.7). A rod connected to the rear-end of the FBM can perform longitudinal movement which is translated - by a toothed bar and wheel - into a rotary movement. Therefore, the horizontal x position is also changed by the rotary movement which has to be taken into account. The relative positioning of the overall system is better than 0.1 mm.

The FBM detector board is made of kapton and equipped with two p-i-n-diodes at the tip of the board, a temperature sensor, and a Hall-sensor. The Hall-sensor enables continuous monitoring of the magnetic field on the one hand, but it also allows relative positioning of the FBM to the magnetic field and the verification of the predicted magnetic field by simulations. The entire board is covered by stainless steel in order to prevent electrons hitting the electronic components of the board. Only two holes are drilled into it to allow electrons to reach the p-i-n-diodes.

For this thesis, the horizontal movement capability of the FBM is essential in order to calculate the radially expected electron rate at the FBM location as it allows scanning through the electron flux. The magnetic field changes radially, which directly impacts to the count rate.

CHAPTER 3
CONCEPT OF THE RESPONSE MATRIX

In order to simulate the FBM detector signal, all components in which electrons from the initial tritium beta decay, have to be simulated. For example the Source, the Transport-Sections, as well as the diodes have to be simulated. A full Monte-Carlo simulation requires non-feasible calculation time on available CPU (Central Processing Unit) clusters and would have to be performed for all signal related parameters and their respective uncertainties. Just for the simulation of the Source at one parameter setting, the calculation time is in the order of 20 CPU years. Therefore, to simulate the FBM detector signal, all components are simulated separately (Source, Transport-Section, diodes, etc.). To combine the influence of the various components in KATRIN onto the detector response signal, the *response matrix* method is used, which parameterizes these influences. A comparable approach is utilized to look for sterile neutrinos with the KATRIN experiment [SL18a]. The response matrix ansatz for the FBM is explained in this chapter.

3.1. One dimensional

The basic concept of the response matrix ansatz is to bin all parameters (e.g. energy and polar angle of the particle) in order to simulate the expected detector signal, and therefore to perform a simulation of all components individually. A simple example to understand the concept of a matrix representation is a mono-energetic Source (e.g. electron-gun) emitting electrons into a gas (e.g. tritium) with a certain gas density. The electrons will undergo scattering and the initial mono-energetic particle spectrum smears out.

Therefore, we have a transformation of the initial binned energy spectrum $\vec{E}$:

$$\tilde{\vec{E}} = \sum_{i=1}^{n} E_i \cdot \vec{R}_i \tag{3.1}$$

where each energy bin E_i is transformed by its own response-vector $\vec{R}_i$. The response-vector $\tilde{\vec{E}}$ has the same dimension n as the energy spectrum $\vec{E}$. Therefore, the total response for all bins in $\vec{E}$ requires a number of $n \times n$ response indices.

For simulating the response-vector for the initial bin E_i, the energy within the boundaries of the bin is assumed to be distributed uniformly to get a good representation of the bin. The resulting spectrum $\tilde{\vec{E}}$ has to be investigated after the scattering process. The higher the initial number of electrons in bin E_i is, the more statistically reliable the calculated response-vector.

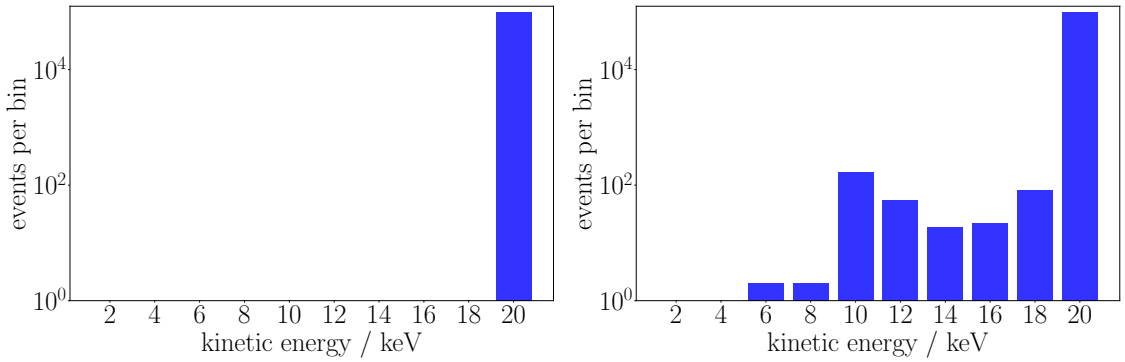

(a) Initial energy distribution $\vec{E}$.

(b) Final energy distribution $\tilde{\vec{E}}$.

Figure 3.1.: *Simulation of an electron-gun emitting electrons with a fixed kinetic energy of 20 keV, starting at the rear-end of the KATRIN Source, with a polar angle of 0° to the magnetic field. While travelling through the Source, the electrons have a certain probability to scatter off the tritium gas molecules inside the Source and thereby the energy spectrum transforms from the energy spectrum $\vec{E}$ shown in (a) to the energy spectrum $\tilde{\vec{E}}$ shown in (b).*

An example is given in figure 3.1. Each entry in the response-vector $\vec{R}_i$ can be calculated as:

$$\vec{R}_i = \sum_{j=1}^{n} \frac{\tilde{E}_j}{E_i} \cdot \vec{e}_j \tag{3.2}$$

where $\vec{e}_j$ denotes the unit vector which is 1 at index j and 0 for all other indices. This equation only holds for $E_i \neq 0$. Although the FBM is only capable of recording energy histograms with its data acquisition, it is essential to know all properties of the particle and experimental setup as they influence the energy distribution. Of particular importance are the kinetic energy, the polar angle of the particle and properties of the experimental setup. For example, radial or azimuthal inhomogeneities of the magnetic field influence the measured detector signal by changing the particle properties. To account for all these parameters of the particles an extension of the response-vector to a response matrix (energy and polar angle) is necessary. The response matrix transforms into multi-dimensional arrays to include more parameters (energy, polar angle, radius/azimuth). In the next section the two dimensional matrix case, extended by the polar angle of the particle, is explained.

3.2. Two dimensional

The basic case of a one-dimensional energy distribution is extended by the polar angle distribution of the particle. The polar angle distribution needs to be known in order to simulate the diode response for the particle. To retrieve the response matrix, the initial distribution matrix **A**, which includes the initial polar angle and energy distribution of the particle, needs to be considered:

$$\mathbf{A} = (a_{ij}) = \begin{array}{c} \\ \boldsymbol{E_1} \\ \boldsymbol{E_2} \\ \vdots \\ \boldsymbol{E_m} \end{array} \begin{array}{c} \begin{array}{cccc} \boldsymbol{\theta_1} & \boldsymbol{\theta_2} & \boldsymbol{\dots} & \boldsymbol{\theta_n} \end{array} \\ \begin{pmatrix} a_{11} & a_{12} & \dots & a_{1n} \\ a_{21} & a_{22} & \dots & a_{2n} \\ \vdots & \vdots & \ddots & \vdots \\ a_{m1} & a_{m2} & \dots & a_{mn} \end{pmatrix} \end{array} \tag{3.3}$$

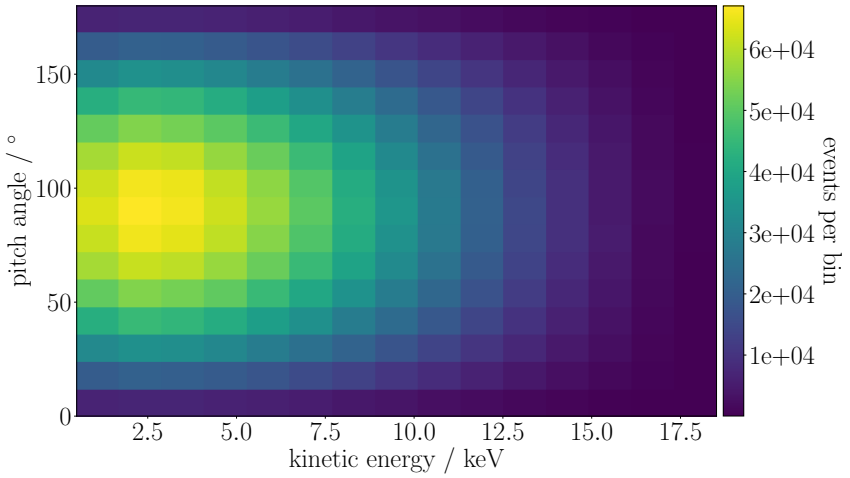

Figure 3.2.: *An initial distribution of the particle energy 500 eV to 18 600 eV and polar angle of 0° to 180° visualized as a two-dimensional histogram with 15 bins per axis. The energy distribution follows the β decay theory for tritium [KAT05] while the polar angle follows the cosine distribution. This example consists of 50 million particles in total.*

Here a_{ij} indicates the amount of entries or the weight for each bin (E_i, θ_j). An example of such a matrix representation is illustrated in figure 3.2 in the form of a histogram.

Performing a Monte-Carlo simulation with a large amount of events $> 10^6$ in the Source of KATRIN of a single scalar, e.g. bin a_{mn}, with a particle energy close to the tritium endpoint and a polar angle of e.g. 90°, with a large transverse momentum, has a high probability of scattering and will therefore distribute events over all energy and polar angle bins in the resulting matrix $\tilde{\mathbf{A}}$.

$$\tilde{\mathbf{A}} = (\tilde{a}_{ij}) = \begin{array}{c} \\ \boldsymbol{E_1} \\ \boldsymbol{E_2} \\ \vdots \\ \boldsymbol{E_m} \end{array} \begin{array}{c} \begin{array}{cccc} \boldsymbol{\theta_1} & \boldsymbol{\theta_2} & \boldsymbol{\dots} & \boldsymbol{\theta_n} \end{array} \\ \begin{pmatrix} \tilde{a}_{11} & \tilde{a}_{12} & \dots & \tilde{a}_{1n} \\ \tilde{a}_{21} & \tilde{a}_{22} & \dots & \tilde{a}_{2n} \\ \vdots & \vdots & \ddots & \vdots \\ \tilde{a}_{m1} & \tilde{a}_{m2} & \dots & \tilde{a}_{mn} \end{pmatrix} \end{array} \tag{3.4}$$

The response matrix $\mathbf{R}$ for single bin a_{mn} can be calculated similarly to equation 3.2:

$$\mathbf{R} = \frac{\tilde{\mathbf{A}}}{a_{mn}} \tag{3.5}$$

Thus, a single bin is represented by a two-dimensional response matrix and the entire initial distribution matrix requires a four-dimensional response to calculate the resulting two-dimensional distribution matrix as follows:

$$\tilde{\mathbf{A}} = (\tilde{a}_{kl}) = \left(\sum_{i,j} a_{ij} \cdot r_{ijkl} \right) \tag{3.6}$$

This work uses the term response matrix and response synonymously, meaning the four-dimensional array r_{ijkl} is referred to as the response matrix.

In the Transport-Section of the KATRIN experiment, i.e. between Source and Rear-Wall as well as Source to FBM detector, higher dimensions of the response matrix are required. The

particles undergo various magnetic field strengths and therefore have different reflection probabilities depending on their radial or azimuthal position. For the other components of KATRIN, the two-dimensional case for single bins is sufficient. Considering the Transport-Section only the radial dependence is investigated while the experiment is assumed to be symmetric in azimuth.

3.3. Uncertainty Estimation

Using the method of the response matrix induces an uncertainty, which is given by the bin width. In order to calculate the response of the experiment in one bin, a uniform energy distribution in this bin has to be assumed, but the actual distribution is not uniform. In other words, the smaller the bin-width, the smaller the induced error by this method, but the more computationally expensive it becomes. An upper bound can be estimated by looking at the bin with the largest gradient between the bin edges and performing the response matrix method in that bin multiple times with increasingly smaller binning in the energy distribution of the initial bin.

Additional uncertainties arise from uncertainties in the scattering cross-sections on tritium in the Source or from the energy-loss-functions. These should ideally be propagated in the simulation by performing the experiment and therefore the response matrix calculations multiple times while varying the settings (e.g. cross-section) within their uncertainties. This approach is not feasible with the response matrix approach as it is computationally too expensive. A conservative approach is to vary the corresponding setting with the uncertainty of 1σ and to propagate it further. Afterwards, the mean of the energy and angular distribution is compared. This method is used to estimate the uncertainties of the simulation.

CHAPTER 4
TRACKING OF PARTICLES IN THE SOURCE

To study the response of the entire KATRIN experiment and specifically the FBM, different simulation frameworks for the different components of KATRIN need to be used. The standard simulation tool for KATRIN is its own simulation framework called Kassiopeia [Fur+17]. It is used to perform particle tracking in complex electromagnetic environments. For this thesis, Kassiopeia is mainly used to study the Rear-Section and the Transport-Section of the experiment. It is also able to perform Monte-Carlo simulations of electrons interacting with tritium molecules in the Source of the KATRIN experiment. However, tracking of particles with Kassiopeia can only be performed on CPUs (Central Processing Unit), which is comparably slow (see section 4.4).

The calculation of response matrices of the Source from Monte-Carlo simulations is an essential part of this thesis. Therefore, a fine energy binning and a large number of events is required. Hence, the simulation code of Kassiopeia was rewritten and optimized to run on GPUs (Graphics Processing Unit).

This chapter focuses on the implementation of physical processes into the technical construct of Monte-Carlo simulations running on GPUs. Firstly, the physical conditions in the Source are explained in section 4.1, followed by a simple Source model to motivate the utilization of GPUs in section 4.2. The workflow of the simulation is described in section 4.3. Afterwards, the GPU Monte-Carlo simulation speed results are compared with the standard KATRIN simulation framework in section 4.4.

The full Source simulation model on GPUs, which could also be used for a comparison of existing analytical models and for neutrino mass analyses, can be simplified even further for the FBM. This leads to a significant speed-up, which is explained in section 4.5. Finally, the physical results of the frameworks are compared and checked whether they provide identical simulation results in section 4.6.

4.1. Source simulation

Electrons, originating from tritium beta decay in the Source, are distributed according to the gas density profile. An example is visualized in figure 2.4. The electrons are emitted isotropically from the tritium molecule and have an energy distribution according to Fermi's theory of tritium beta decay (compare equation 1.22). The emitted electrons are guided by a magnetic field

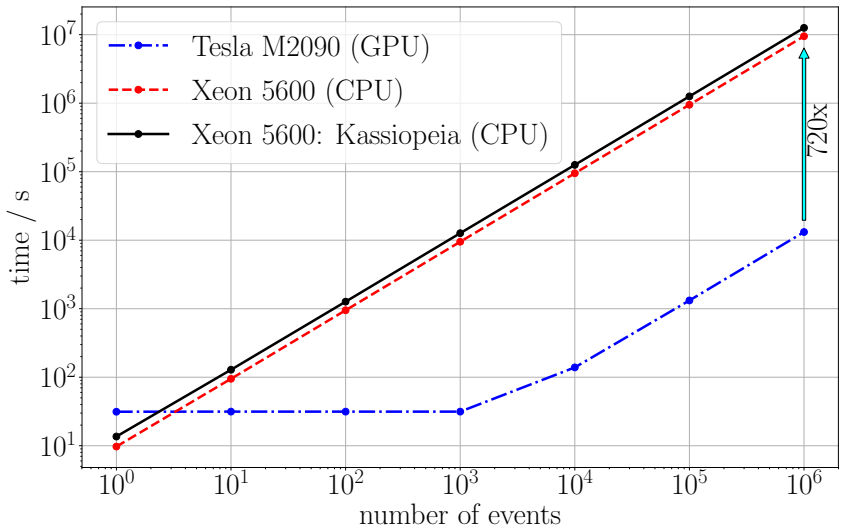

Figure 4.1.: *The performance of particle tracking on a single CPU versus a single GPU. On the x-axis the number of simulated electrons is shown while on the y-axis the required tracking time for this number of events is visualized.*

longitudinally towards the two exits at the front and rear-side of the Source. Thereby, they have a certain probability to interact with the gas molecules in the Source, which can change the polar angle and kinetic energy of the electron. To fit the neutrino mass in KATRIN, the shape of the tritium beta electron spectrum close to the tritium endpoint has to be well understood. Therefore, dedicated analytical models are used in the KATRIN experiment for the endpoint region [Kle+18].

In contrast to the main detector, the Focal Plane Detector (FPD), the FBM is capable of measuring deep into the beta electron spectrum (towards lower electron energies) and therefore it is important to understand the spectrum far from the tritium beta endpoint. Additionally, a future upgrade of KATRIN will search for sterile neutrinos, which increases the need to understand and describe the complete spectrum.

For this thesis, the Monte-Carlo approach for determination of the response matrix in the Source is used. In order to track electrons in parallel, the computational power of GPUs is utilized. The technical challenges are presented in the following sections.

4.2. Source simulation on GPU

The paths of electrons, which follow their magnetic field line through the KATRIN Source, are independent and do not interfere with each other. On a standard CPU based approach the particles are therefore tracked one after another. GPUs offer the flexibility of tracking independent particles in parallel on thousands of cores on a single (GPU-) device. This approach is called General-Purpose GPU (GPGPU) computing.

For scientific purposes special GPUs with a high performance on 64-bit calculations were developed. One example is the NVIDIA Tesla series (reference [NVI19]) which is used for this work.

Simplified first model

To test the usage of GPUs to track particles in magnetic fields a simple model of the Source is used. A tube of 10 m length is generated which is about the length of the KATRIN Source. It is oriented coaxial to the applied magnetic field of 3.6 T in z-direction. All particles have identical starting properties with a polar angle of 45° and a kinetic energy of 18.6 keV. The electrons are generated at the rear-side exit surface of the tube at $z = 0\,\mathrm{m}$ and terminated at the front-side surface at $z = 10\,\mathrm{m}$. To track the electrons, the Lorentz-equation:

$$\frac{d\vec{p}}{dt} = q\left(\vec{E} + \frac{\vec{p}\times\vec{B}}{\gamma m}\right) \tag{4.1}$$

is solved numerically using the Runge-Kutta-8 integrator [Ver78]. The required simulation time per number of events is visualized in figure 4.1.

In order to find programming errors and have a comparison of execution time on CPU and GPU, the code development started off as standard C++ CPU code and was translated to GPU Cuda code afterwards. For this reason, two CPU references are given in figure 4.1. One for the developed CPU code for this thesis and the other one for the Kassiopeia simulation. The speed improvement compared to the Kassiopeia framework is negligible with approximately 30 %. This is mainly caused by simplifications in the calculation of the electron path, because the particle does not interact and therefore its properties (e.g. Lorentz factor) do not need to be recalculated at each step of the electron on its path through the Source.

As expected on the CPU based code, the required calculation time is directly proportional to the number of simulated events. The GPU behaves differently as a plateau like structure develops for a small amount of events on the order of 1000 and below. The GPU code tracks electrons in parallel and can handle 2048 electrons at once. Hence, 2048 particles are always tracked at the same time on a single GPU. For more than 2048 events, the required simulation time behaves linearly to the multiple of 2048 particles.

On one hand, the speed result presented in figure 4.1 hints towards a speed improvement of factor 720 that can be achieved using GPUs. On the other hand, the simulation configuration is highly-optimized for GPUs.

In other words, only a small amount of data is transferred from host (CPU) do device (GPU) and all electrons have identical starting conditions, which is a perfect configuration for simulations on GPUs.

One goal of this thesis is to enhance the required simulation time of Kassiopeia Monte-Carlo simulations of the Source on a single CPU by - at least - a factor of 100 for the same simulation on a single GPU. This is required to calculate the response of the source for electrons with a kinetic energy far away from the tritium endpoint and appears to be achievable considering the speed improvement in the simplified model.

4.3. Simulation workflow

An overview of the GPU based simulation workflow is given in figure 4.2. The blue boxes represent steps performed on a single CPU while in red the simulation steps performed on the GPU are visualized. Although it may seem that most of the simulation workload is handled by the

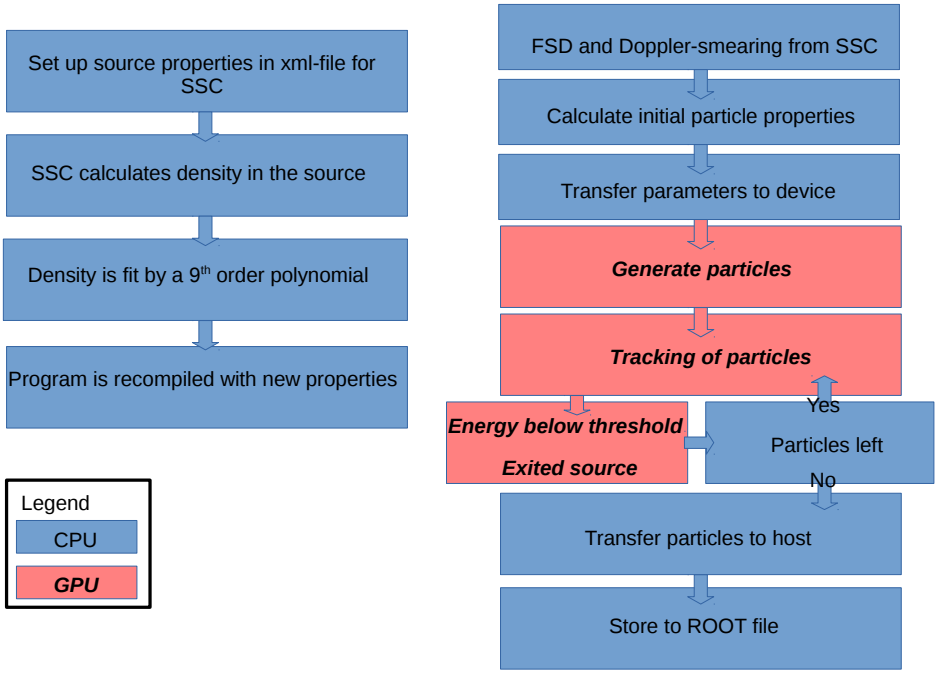

Figure 4.2.: *Schematic of the simulation workflow describing the different steps performed on CPUs (host) and GPUs (device) for the simulation.*

CPU, the computationally expensive calculations are performed on the GPU device. Additionally, some parts of the code are kept on the host to utilize existing interfaces, e.g. to the Source density calculation framework.

In order to use different configurations of the Source, i.e. Source temperatures and column densities that change the density profile in the Source, an interface to SSC (Source and Spectrum Calculation) [Höt12; Kuc+18a] is established. It is able calculate the density profile for different Source configurations. The profile is provided by SSC as an array of gas densities in the Source and is fit with a ninth order polynomial for a normalized root-mean-square-deviation of approximately 10^{-5}. The fit is performed to avoid lookup tables on the GPU. The fit result is taken as input for the simulation.

The generation of particle properties is also done on the CPU. This includes the position of the electron within the Source, the direction according to an isotropic distribution, and the initial kinetic energy. All these steps could also be performed on the GPU in parallel, but in order to perform FSD (Final State Distribution) and Doppler broadening calculations an interconnection to the CPU based SSC is required. These effects are crucial close to the tritium electron endpoint energy in order to determine the neutrino mass.

The amount of electrons generated at once is determined by the storage space on the GPU. All properties need to be transferred onto the device and each particle is created by its own particle class. Thereby, 10^7 particles require $\approx 3.6\,\mathrm{GB}$ of memory on the device. This memory space is occupied by the initial particles generated on the host and additional space is allocated for secondary electrons. The secondaries are generated due to the ionization of the gas molecules by (primary) electron interactions. The limited amount of space on the device for secondaries enforces an energy threshold of $\approx 500\,\mathrm{eV}$. Below this threshold, more secondary electrons are generated than memory space is available on the device for 10^7 particles. This energy threshold

in the simulation is sufficient as the energy threshold of the Forward Beam Monitor detector is approximately 5 keV.

Tracking of particles

After the properties of the electrons are transferred onto the device and the generation of the initial electrons on the device succeeded, the electrons are tracked adiabatically according to their initial position and momentum. Thus, their radius $\vec{r}_c$ and momentum $\vec{p}$ can be calculated according to the following equations [Gro15]:

$$\frac{d\vec{r}_c}{dt} = \frac{p_\parallel}{m\gamma} \cdot \frac{\vec{B}_c}{B_c} \tag{4.2}$$

$$\frac{dp_\parallel}{dt} = -\frac{p_\perp^2}{2\gamma m B_c} \left(\vec{\nabla} B_c + q\vec{E}_c\right) \cdot \frac{\vec{B}_c}{B_c} \tag{4.3}$$

$$\frac{dp_\perp}{dt} = \frac{p_\perp p_\parallel}{2\gamma m B_c} \vec{\nabla} B_c \cdot \frac{\vec{B}_c}{B_c} \tag{4.4}$$

This tracking method splits the momentum into its longitudinal and transversal component and propagates them independently. It allows larger step sizes than the exact integration of the Lorentz-equation presented in section 4.2, especially with a longitudinally constant magnetic field as utilized in this GPU based simulation, which is a good approximation of the field in the Source of KATRIN. Additionally, synchrotron losses are included into the simulation, which adds an additional term to the transverse momentum [Fur15]:

$$\frac{dp_\perp}{dt} = -\frac{\mu_0}{6\pi c} \frac{q^4}{m^3} \vec{B}_c^2 p_\perp \gamma \tag{4.5}$$

The particles are tracked until they reach the rear- or front-exit of the 10 m long Source, which is equivalent to the bottom or top surface of the tube in the simplified model. If they fall below the energy threshold by interactions with the gas molecules the tracking is also stopped. If a particle is terminated by one of these two conditions, the device automatically continues with the next primary particle. It depends on the hardware of the device how many particles can be tracked in parallel and the code has to adapted for the different GPU hardware models.

A few percent of particles have a track length of hundreds of meters in the 10 m long Source, because they have a large transversal momentum compared to its longitudinal component or undergo many interactions with the gas in the Source and scatter back and forth. To be more time efficient with particles that are stored in the Source for a long time, a maximum number of steps is set, which a particle can undergo, see figure 4.3. The cut is set to 85 000 steps, which covers $\approx 91\,\%$ of particles that left the Source or fell below the energy threshold before they reach the maximum number of steps. These particles, terminated by the maximum number of steps, are not lost in the particle simulation. After all initial primary particles were tracked, the remaining particles, which are not terminated by the energy threshold or by leaving the Source, are re-injected into the simulation procedure with their properties at their termination. Among those re-injected particles are also secondary electrons from ionization of the gas in the Source. With this method the full capacity of the GPU is utilized. After the tracking of all remaining particles is finished, all particles are transferred back to the host and stored into ROOT trees [BR97] (compare figure 4.2). Within these trees, only the initial and final track information of the particle is stored, but no information about the step level or interactions on the step level.

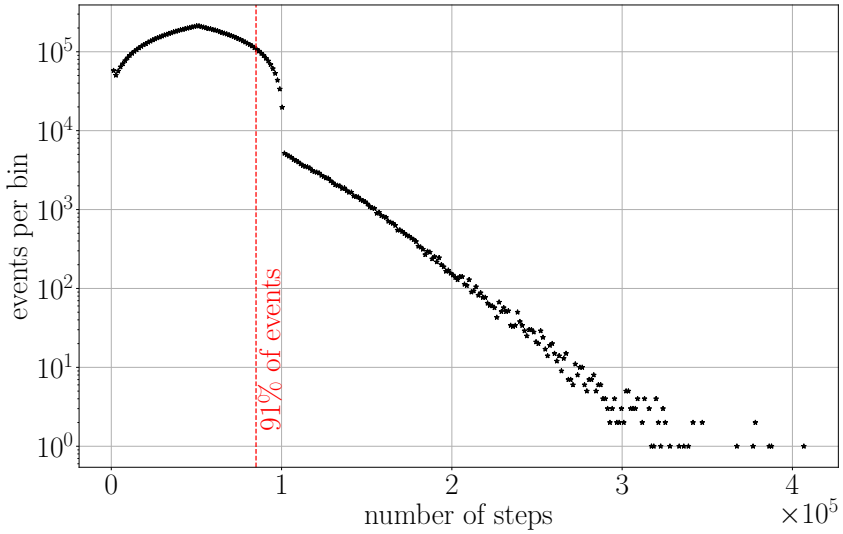

Figure 4.3.: *Simulation result of the tracking of 10^7 electrons through the Source. On the x-axis the number of steps for particles to fall below the energy threshold of 500 eV and hence being terminated or before leaving the Source is shown. On the y-axis the number of particles per x-bin is given. The red dashed line indicates the cut at 85 000 steps.*

Particle interactions

While particles travel through the Source, which has an average density of approximately $5 \cdot 10^{20}$ molecules per cubic meter in the nominal configuration, their probability of interacting with the gas depends on the individual cross-sections of the different interaction processes. These are adapted from the implementation in Kassiopeia and the cross-sections are visualized in figure 4.4. A more detailed discussion about the implementation into Kassiopeia can be found in the references [Hei15] and [Wan13]. In order to avoid overhead on the GPU, interactions below 500 eV electron energy are not considered, although these are implemented into the Kassiopeia interaction model. As the energy threshold of the FBM detector is in the range of a few keV (usually 4 keV to 5 keV), these are not crucial for the simulation of the detector signal.

However, the cross-section is one of the biggest uncertainties in the simulation and has to be extrapolated from above 1 keV to the endpoint as no data is available (compare figure 4.4). Close to the endpoint of tritium at 18.6 keV, the measured total cross-section is $(3.40 \pm 0.07) \cdot 10^{-18}\,\mathrm{cm}^2$ [Ase+00] and the extrapolated value in Kassiopeia is $3.62 \cdot 10^{-18}\,\mathrm{cm}^2$ differ by approximately 6 %. Another model integrated into Kassiopeia for simulating the endpoint uses a fixed cross-section. The cross-section can be set individually by the user. The GPU code uses the extrapolated Kassiopeia cross-section model to have an energy range from 500 eV to 18 600 eV. The energy loss calculation is also identical to the implementation in Kassiopeia. A discussion can be found in [Ase+00].

4.4. Speed results

The achieved speed improvement of a Monte-Carlo Source simulation on a GPU versus a CPU on a similar code basis and an additional comparison to Kassiopeia is shown in figure 4.5. With highly optimized code for the purpose of tracking electrons through the the Source of KATRIN, the produced CPU code outperforms Kassiopeia by a factor of three. This is mainly due to optimizations applied because of the neglected electric field and magnetic field gradients. The

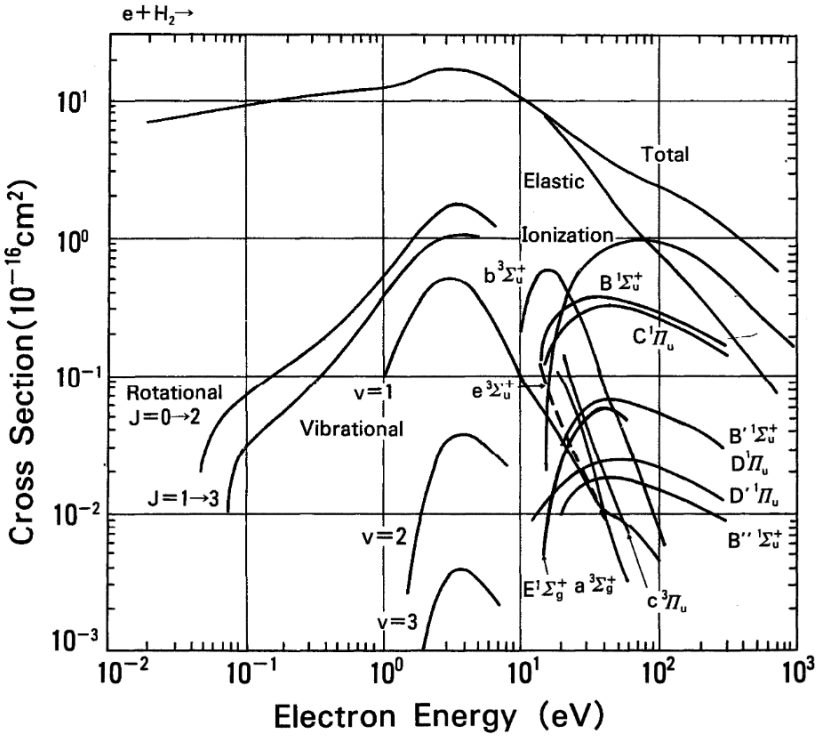

Figure 4.4.: *Cross-sections for electrons on hydrogen molecules. In Kassiopeia, the cross-sections were extrapolated to fit higher energy regimes. Figure taken from [Taw+90].*

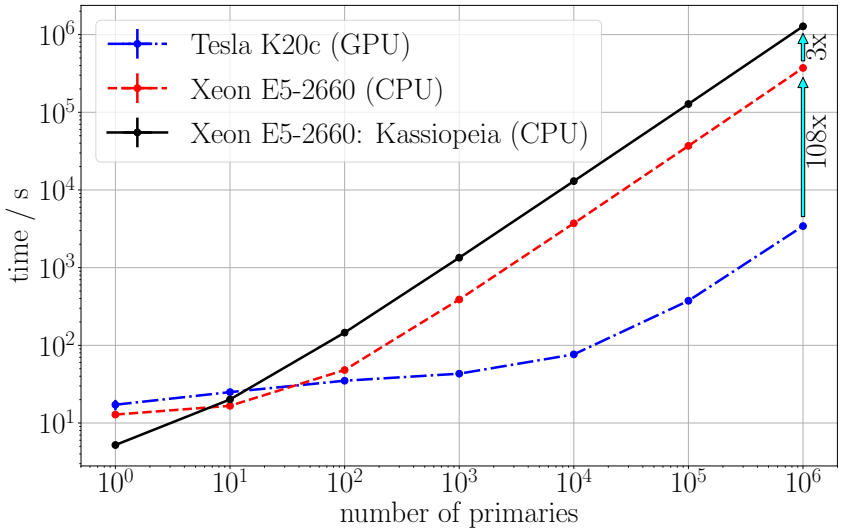

Figure 4.5.: *The required calculation time (y-axis) for the simulated the number of primary events (x-axis). The simulation includes secondary particles.*

equivalent GPU code is 108 times faster than the optimized CPU code. That means, for the complete simulation of the response matrices, five Tesla K20c GPUs are used. Hence, this represents an equivalent of 540 Xeon E5-2660 CPU cores.

Comparing figure 4.1 and 4.5, the latter does not show the characteristic plateau in the required simulation time for a small number of primary particles on the GPU as can be seen in figure 4.1. In the final simulation code, only the created particles are tracked and the GPU is not filled to its maximum capacity if the number of electrons is lower. The required time depends on the initial properties of the electron.

4.5. Simplifications for Response Matrix

To simulate $312 \cdot 36$ response matrices with $5 \cdot 10^6$ events per bin as used in this thesis, the GPU code did undergo further simplifications. Assuming a constant magnetic field and a symmetric density distribution in the Source, the density can also be assumed to be constant in the Source [SL18b]. The electrons are generated laterally uniform in the Source. In the normal (not simplified) model, the probability of interactions of the particle with the gas is calculated at each step. In contrast, utilizing a constant density in the Source, the point of the next interaction can be calculated. The step sizes are defined by the time of the next interaction of the particle. The equations can be found in the reference [Fur+17]. Additionally, FSD and Doppler broadening are removed as they have no effect on the uniform energy distribution within each bin of the response matrix. Synchrotron radiation has a non-detectable effect for the FBM and is also not considered in the Source simulation, but an upper estimate is given in section 5.1.2. With all these simplifications applied, the complete simulation of the response matrices takes about 10 days on five Tesla K20c cards.

For this number of events, the full particle information cannot be stored as this method requires too much storage space. Therefore, the response matrices for each bin are directly calculated in the simulation code and stored.

4.6. Comparison of simulation results

In order to verify the simulation code on GPUs, a virtual electron-gun is placed at the rear-side of the Source. It emits 10^7 electrons with an initial energy of 18.6 keV, which are uniformly distributed in $\cos(\theta)$ with θ ranging from 0° to 45° in forward direction. The magnetic field is set to 70 % (2.52 T) of the nominal field as stated in the KATRIN design report[1].

The electrons leaving the front-exit of the Source are used for the analysis shown in figure 4.6. Their final kinetic energy is subtracted from their initial kinetic energy resulting in the energy loss of the particle. The equivalent method is used for the angular change of the particle. A model with a variable step size and a constant density as well as the model with the fixed step size and real density distribution including synchrotron radiation are compared against the Kassiopeia model. Both models agree well with the Kassiopeia reference. Hence, for this work, the variable step size with a fixed density can be utilized.

[1] This configuration was used during First Tritium campaign.

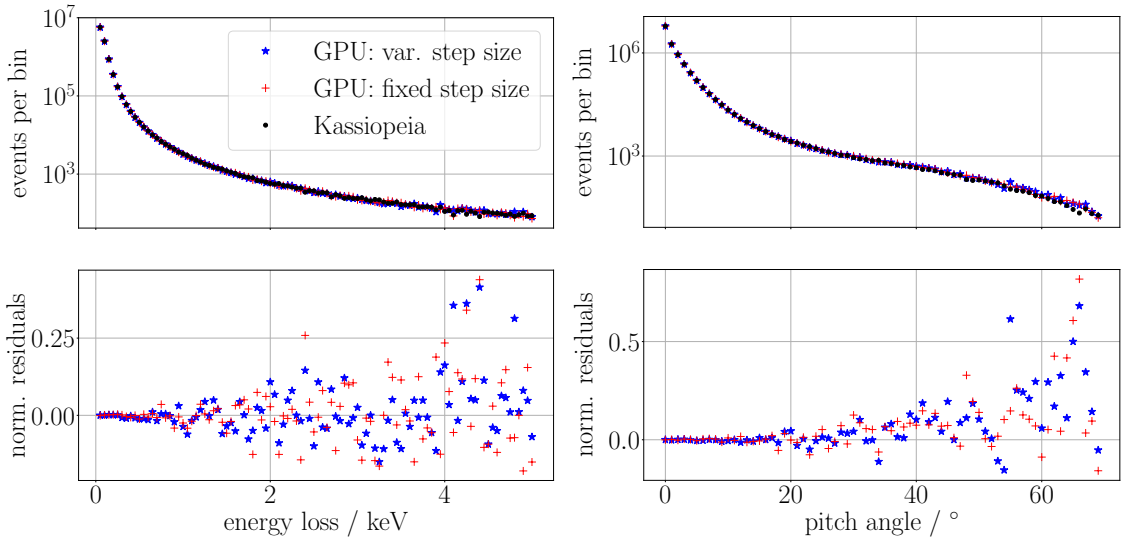

(a) Energy loss. **(b)** Angular change.

Figure 4.6.: *The energy loss (a) and angular change (b) of electrons is shown with an initial kinetic energy of 18.6 keV travelling through the Source at a magnetic field of 2.52 T. In the figures at the top the energy loss and changes of the pitch angle using three different MC (Monte-Carlo) generators are shown. Kassiopeia represents the standard KATRIN simulation framework. The fixed step size refers to section 4.2 while the variable step size includes all model simplifications described in the same section. In the bottom figures, the residuals normalized to the Kassiopeia simulation are shown.*

CHAPTER 5
TOWARDS THE SIMULATION OF THE FBM RESPONSE

As stated in the previous chapter, Kassiopeia is used for tracking particles through the components of the KATRIN experiment. Kassiopeia is part of the KASPER (KATRIN analysis and simulation package) framework. The geometry of the KATRIN experiment and the magnet configuration are implemented in this framework.

Other than that, for the complete simulation of the KATRIN experiment, the reflection of electrons on the Rear-Wall needs to be simulated. For this purpose, the GEANT4 (GEometry ANd Tracking) toolkit is used [Ago+03]. It can simulate different kinds of particles and their interactions passing through matter. This is discussed in section 5.2.

The GEANT4 toolkit is also used to simulate the influence of the cover on the detector board in section 5.4. The cover protects the electronics on the FBM detector board.

The response of the FBM *p*-*i*-*n*-diodes is simulated utilizing the KESS (KATRIN Electron Scattering in Silicon code) framework [Ren11]. It is used to simulate dead-layer thicknesses and the deposited energy of each electron in the sensitive volume. In contrast to GEANT4, it is optimized for low energetic electrons in silicon. The simulation of the diode response can be found in section 5.5.

In this chapter all the challenges of the simulation of individual KATRIN components and the simulation results leading to the respective response matrices are presented. The combination of these matrices and the final response is shown in chapter 6.

5.1. Source Response Matrix

Calculation of a single response matrix for the Source section is not sufficient. The Source response is split into six different responses by the design of the Source, depending on the positions of the particles and their directions.

Two of them emanate directly from tritium decay itself. Tritium is injected in the central part of the Source and it travels by diffusion towards the rear- and front-side of the Source. Electrons, emanating from tritium beta decay, are guided by a magnetic field and can leave the Source at the front- and at the rear-end. The exit probabilities for electrons being distributed in different angle and energy bins are represented by two distinct response matrices.

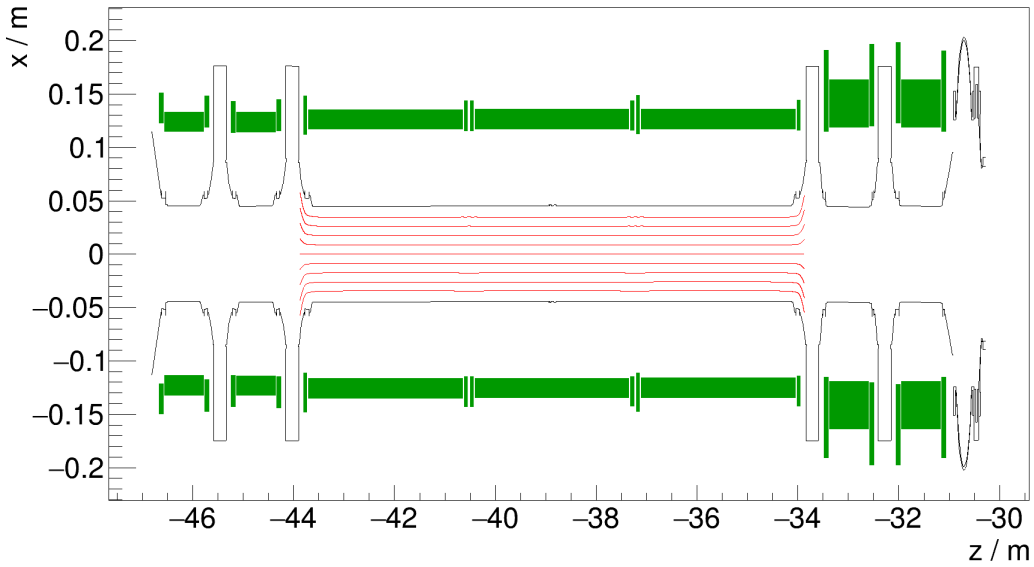

Figure 5.1.: *Schematic of a cut through the xz plane of the WGTS. The green blocks indicate the super-conducting magnets while the beam tube walls are colored in black. The red colored lines show the magnetic field lines within the Source. They stop before they enter the differential pumping sections. The simulation of the Source response matrices is performed in the volume shown by the magnetic field lines.*

Additionally, electrons that leave the Source towards the Transport- or Rear-Section are partially reflected back into the Source. Therefore two additional response matrices describe electrons, entering the Source on one side, and leaving the Source at the opposite side, or the side of their initial entrance. As reflected electrons enter the Source either from the rear-side or front-side this adds up to four additional response matrices in total.

Utilizing the simplifications described in section 4.2, the Source is assumed to be symmetrical, i.e. only three response matrices are required. For example, electrons, from beta decay, leaving the Source at the front side have the identical response matrix to electrons leaving on the rear-side. Thereby, only the angular distribution is shifted by 180° (or flipped) while the energy distribution remains unchanged. Hence, for electrons from tritium beta decay leaving the Windowless Gaseous Tritium Source only one response matrix simulation is sufficient. Electrons, reflected in the Rear-Section or Transport-Section can be described by the same set of response matrices, only flipped on the polar angle axis, for transmission and reflection. The setup of the Source and their magnetic field lines can be seen in figure 5.1.

5.1.1. Results from beta decay

To model the response of the Source for tritium beta decay, the energy spectrum is split into 50 eV bins ranging from 3000 eV to 18 600 eV and the polar angle is split into 5° bins, ranging from 0° to 180° making a total of 11 232 matrix indices. However, each matrix index needs to be represented by an individual response matrix with the same amount of indices of 11 232.

These matrices are simulated using a uniform electron distribution in energy and in $\cos(\theta)$ within a single bin. That means, they can be applied to different shapes of the initial tritium electron spectrum and the goodness of the representation is the better, for smaller bin widths. The initial beta electron distribution is simulated assuming a tritium endpoint energy of 18 575 eV and a neutrino mass of 0 eV. The angular distribution is created by a random number generator,

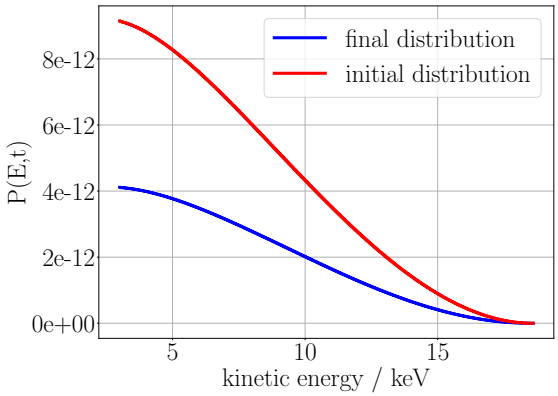

(a) Energy distribution.

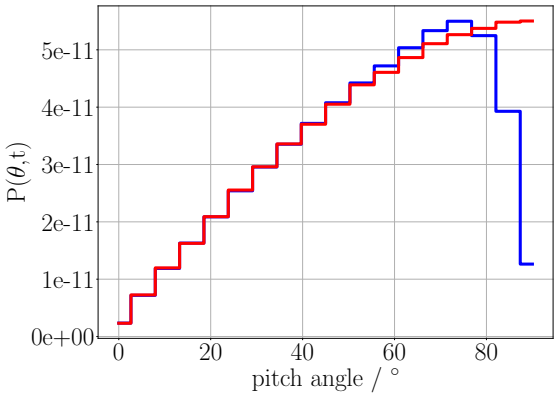

(b) Angular distribution.

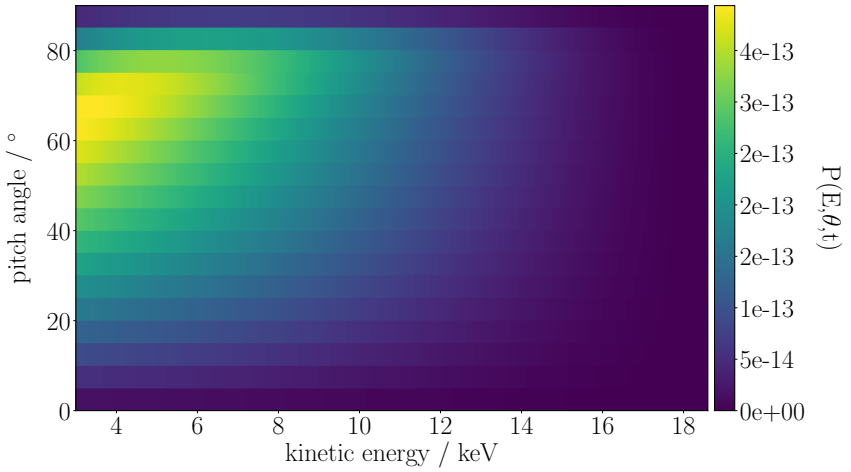

(c) Combined distribution.

Figure 5.2.: *The energy distribution (a) and angular distribution (b). The initial distribution is shown in red and the distribution at the front-exit of the WGTS in blue. The y-axis denotes the probability of a single tritium atom to decay into the corresponding bin per second and travel towards the Source exit. The distribution in figure (c) is the combination of the final distribution from figures (a) and (b).*

which is uniform in $\cos(\theta)$. The magnetic field in the Source is set to $\vec{B}^{\mathsf{T}} = (0, 0, -2.52\,\mathrm{T})$.

An example distribution of electrons at the front-exit of the Source is shown in figure 5.2. In figure (a) the initial energy distribution integrated over all spherical directions is shown. Approximately 45.9 % of particles reach the front-exit of the Source, shown as the final distribution. As the Source is assumed to be symmetrical, the same number of electrons reach the rear-exit of the Source. The missing particles (8.2 %), not leaving the Source, have a kinetic energy below the energy threshold of 3 keV due to interactions with the gas molecules and are not tracked to the Source exit in the simulation.

In figure (b) an overview of the polar angle distribution at the time of the tritium decay and after leaving the front-exit of the Source is given. The cut for the plot is set to 90°, because electrons leaving the Source in forward direction have - by definition - a polar angle of $\theta \leq 90°$. Nevertheless, electrons with a larger initial polar angle can leave the Source in forward direction through interactions with the tritium molecules which change their polar angle. Electrons with

a large pitch angles have the tendency to scatter to lower angles so they are able to leave the Source. The figure is not symmetric for electrons leaving the Source at the opposite side. The spectrum is flipped along the polar angle axis for a range of 90° to 180°

In figure (c) the combination of the final distributions shown in (a) and (b), which represents the probability $P(E, \theta, t)$ for a single tritium atom to emit an electron that falls into the 50 eV energy and 5° polar angle bin per second and to reach the front-exit of the Source.

5.1.2. Uncertainty estimation

The accuracy of the response estimation is influenced by several factors. Some are induced by the method itself, i.e. by binning the simulation results, others are systematic uncertainties. Examples are the density or the tritium cross-section for electrons. In this section an overview of the propagated uncertainties is given that represent the uncertainties of the simulation results in the Source.

- **Binning:** The response matrices are calculated using a uniform electron energy distribution inside 50 eV energy bins. Binning is only an approximation of the real shape in that energy range and the smaller the bin width - the smaller is the induced error by this method. An estimation can be derived by looking at the largest gradient of a real tritium beta decay spectrum and comparing it to a uniform distribution. For a tritium endpoint energy of 18 575 eV and a zero neutrino mass, the largest gradient is in between the bin edges of 8850 eV to 8900 eV with a slope of 8 ‰. Both distributions are simulated in this energy range with 10^8 events and a uniform distribution in $\cos(\theta)$ between 45° to 50°. The weighted mean of the two energy distributions are compared at the front-exit of the Source. The energy threshold for electrons is set to 3 keV.

  The mean energy for the beta decay spectrum in this bin is $E_\beta = 8778.93$ eV and $E_{\text{uni}} = 8778.96$ eV with a difference of 0.03 eV ($3 \cdot 10^{-4}$ %). This effect is negligible compared to the energy resolution and uncertainty of the FBM detector (section 5.5).

  The distribution for pitch angle bins follow the same isotropic distribution as without binning. Hence, no error is induced by binning the polar angle of the electrons in the Source initially.

- **Cross-section and density:** One of the largest uncertainties in the Source is the cross-section of electron scattering off tritium. It is assumed to be 6 % at the tritium endpoint as shown in the particle interactions discussion in section 4.2. Other than that, one of the KATRIN requirements is a stable Source column density on the per mille level [KAT05]. The probability $P(t)$ of a particle interaction with a gas molecules in the simulation per time t is calculated by [Fur+17]:

$$P(t) = 1 - \exp\left(\frac{t \cdot v}{\lambda}\right) \tag{5.1}$$

  with the mean free path $\lambda = (n \cdot \sigma)^{-1}$, n being the target number density and σ the summed cross-section of all interactions of the target and v the velocity of the particle. From this equation one can read that relative uncertainties of the density and cross-section have an identical effect on the interaction probability. Therefore, both effects are combined to a total (conservative) 7 % relative uncertainty. This also includes fluctuations of the magnetic field as they can be represented as fluctuations of the column density which are on the per mille level ([KAT05]) as well. The uncertainty estimation is performed using 10^7 particles with identical starting conditions. They are distributed uniformly in the

Source with an isotropic momentum direction vector, or uniformly in $\cos(\theta)$. The kinetic energy of the electron is set to the lowest energy bin between 3000 eV to 3050 eV, because at these energies the electron has the largest interaction probability. After the particles propagate to the Source exit, the weighted mean of the energy spectrum at the front-exit of the Source is compared against the same spectrum at nominal Source conditions. Since the initial electron energy is close to the nominal energy threshold in the simulation (of 3 keV), the threshold is set to 500 eV in this uncertainty estimation. The results are as follows:

$$\begin{aligned} E &= 2574.30\,\text{eV} \qquad \text{for } \lambda^{-1} = 1.00 \cdot \lambda^{-1}_{\text{nominal}} \\ E &= 2590.80\,\text{eV} \qquad \text{for } \lambda^{-1} = 0.93 \cdot \lambda^{-1}_{\text{nominal}} \\ E &= 2559.41\,\text{eV} \qquad \text{for } \lambda^{-1} = 1.07 \cdot \lambda^{-1}_{\text{nominal}} \end{aligned}$$

As expected for larger densities/cross-sections, the probability of interactions with the gas molecules increases and therefore the mean energy is lowered by approximately 14.89 eV. This is a 6 ‰ effect. This also accounts for lowering the interaction probability by a larger mean energy of approximately 16.50 eV which is also a 6 ‰ effect.

The amount of interactions with the gas molecules also influences the final pitch angle distribution. The weighted mean of the final pitch angle is about $(50.3 \pm 0.3)°$ (6 ‰) in both directions and, as expected from figure 5.2, the more particle interactions, the more likely there is a smaller mean pitch angle at the exit of the Source.

Besides the influence on the polar angle and energy distribution, different densities/cross-sections also influence the probability of electrons being able to leave the Source. The difference for 7 % shifts induces a change of the probability and therefore the rate by 1.5 %. For an increasing density or cross-section, the probability decreases and increases for a smaller density or cross-section. This does not account for additional electrons emanated at a higher tritium density.

- **Cyclotron radiation:** To simplify the event-by-event simulation, the cyclotron radiation is removed from the simulation. An upper limit can be calculated by using equation 4.5. In the non-relativistic case (the Lorentz factor is about $\gamma = 1.04$ for a kinetic energy of 18 575 eV) and by replacing the transversal momentum by the energy $E_\perp$ results in:

$$\frac{\Delta E_\perp}{\Delta t} = -\frac{\mu_0}{3\pi c}\frac{e^4}{m_e^3}\vec{B}^2 \cdot E_\perp \approx -0.4 \cdot \vec{B}^2 \cdot E_\perp. \tag{5.2}$$

The minus sign denotes that the energy is radiated away from the particle. Assuming a magnetic field of $B_z = 2.52$ T and a pitch angle of 90° at the endpoint energy of 18 575 eV, results in an energy loss of 457 meV for particles that spent 10 µs in the Source. Thereby, 10 µs is a conservative estimate for particles with kinetic energies larger than 3 keV.

5.1.3. Particles entering sideways

Electrons, that are magnetically reflected in the Transport-Section or backscattered from the Rear-Wall are entering the Source sideways (front-/rear-side). As the Source is assumed to be symmetric, the response of electrons entering from the front- or rear-side is identical, but flipped on the polar angle axis. Hence, only response matrices for electrons entering from one side, in this case the rear-side, are calculated. The electrons will be transmitted to the front or back-reflected to the rear-side of the Source. The results for three of the 312 energy bins is shown in figure 5.3. In figure (a), the summed transmission probability over the initial pitch angle is

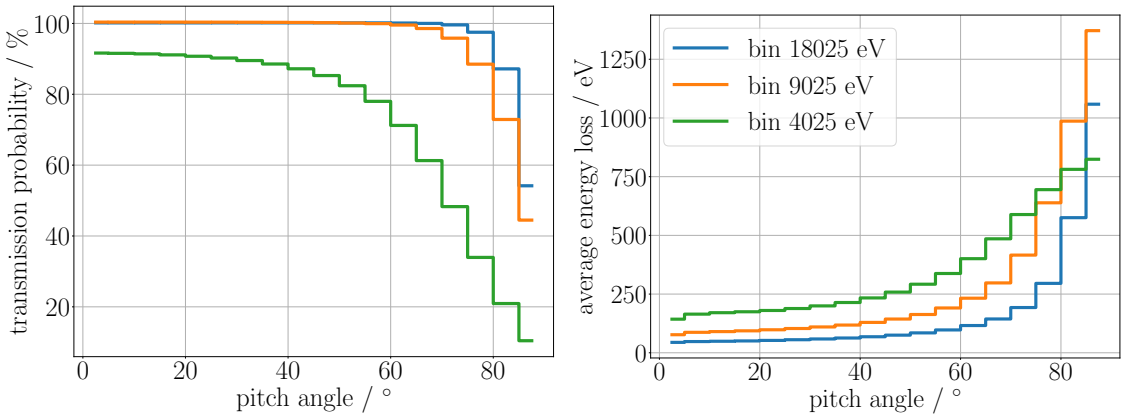

(a) Transmission probability.

(b) Average energy loss.

Figure 5.3.: *The transmission probability (a) and average energy loss (b) of electrons entering the Source from the rear-side and traveling to the front-side in their respective energy bin over all pitch angles 0° to 90°. The transmission probability is given as the summed probability over all energy bins 3 keV to 18.6 keV at the front-exit of the Source.*

shown. The x-axis is split into 18 polar angle bins with a 5° bin width. For an initial energy of 18 000 eV to 18 050 eV, i.e. bin 18 025 eV, the transmission probability is close to 100 % up to a pitch angle of 70°. The transmission probability is defined as the summed probability over all energy bins from 3000 eV to 18 600 eV at the front-side.

At larger pitch angles, above 70°, the transmission probability drops. The utilized energy bin at 18 025 eV has a surplus of 15 keV to the energy threshold and most electrons above 70° are reflected and leave the Source at the rear-side, but are not stopped in the Source.

Electrons, in the energy bin of 9025 eV, have a larger interaction probability than electrons in bin 18 025 eV as the cross-section for interaction in the Source increases. Therefore, less particles are transmitted to the front-side and more are reflected to the rear-side compared to the higher energy bin.

In contrast, the bin representing an electron energy of 4025 eV is close to the threshold of 3000 eV at which the particle is terminated. Additionally, the cross-section is compared to that of electrons in bin 9025 eV. Therefore, at low pitch angles, the transmission probability is only $\approx 90\,\%$ and drops down to $\approx 10\,\%$ for pitch angles at 85° to 90°. The total reflection probability is largest for bin 9025 eV with a 3000 eV energy threshold compared to bin 4025 eV and 18 025 eV.

In figure 5.3 (b), the averaged lost energy for transmitted electrons over their respective initial pitch angles is shown. This is calculated by weighting the center of each energy bin with its individual response and calculating the mean which gives the average energy of electrons leaving the Source in front-direction. The average energy is subtracted from the initial energy, which results in the energy loss at different pitch angles.

As expected, the average energy loss increases for larger pitch angles. It is the largest for electrons in the energy bin 4025 eV. In comparison to the higher energy bins, the energy loss flattens out towards larger pitch angles of $> 70°$, because electrons at these angles are likely to fall below the energy threshold of 3000 eV and therefore are terminated in the Source. Other than that, the average energy loss for electrons in the energy bin 9025 eV is larger than for electrons in bin 18 025 eV as the interaction probability is larger.

5.2. Rear-Section

The Rear-Section of the KATRIN experiment guides electrons from the Source to the Rear-Wall. These electrons leave the Source at the rear-end with a pitch angle of 90° to 180°. In this section, the effect of magnetic field guidance and the scattering off of the Rear-Wall onto the electrons is presented.

The two effects are expressed as response matrices for the scattering at the Rear-Wall process and as an analytical transmission function for the magnetic field guidance in the Rear-Section. Electrons, guided by magnetic field lines, undergo changes of their pitch angle depending on the magnetic field they experience. This angular change is described by the following equation [KAT05]:

$$\frac{\sin\theta_1}{\sin\theta_2} = \sqrt{\frac{B_1}{B_2}}. \tag{5.3}$$

The maximum magnetic field the electrons experience during their travel defines the acceptance angle θ_{accept}. If the magnetic field increases, the pitch angle of the electron increases as well. As soon as the pitch angle reaches 90°, the electron is reflected backwards. For this scenario equation 5.3 can be expressed as:

$$\theta_{\text{accept}} = \arcsin\sqrt{\frac{B_{\text{S}}}{B_{\text{max}}}} \tag{5.4}$$

with an initial magnetic field of B_{S} that allows the electrons to pass the maximum magnetic field B_{max}. The angle θ_{accept} is defined as the acceptance angle in the starting magnetic field B_{S} and is equivalent to 90° at B_{max}.

This section is split into two parts. In one part the influence of the Rear-Section and wall in nominal KATRIN configuration is discussed. The second part discusses the settings during the First Tritium campaign as the Rear-Section magnet was off and the valve V0 was closed.

For simulating the magnetic field lines and synchrotron radiation losses the Kassiopeia framework is used. The scattering simulations are performed with the GEANT4[1] toolkit.

To avoid confusion in the upcoming sections, all angles are always referring to the z-axis. That means electrons travelling towards the rear side of KATRIN have pitch angles in the range of 180° to 90° and 0° to 90° when travelling towards the front side. This scheme is also applied to the inclination and acceptance angles of the electrons. The inclination angle is defined as the angle of the magnetic field line to the z-axis while entering the Rear-Wall or valve V0.

5.2.1. Nominal KATRIN operation

In nominal KATRIN operation, electrons leaving the Source in rear-direction, are guided to the gold-plated Rear-Wall [Sch16] through the Rear-Section. A visualization of this component and the magnetic field lines is given in figure A.II.

An overview of the properties of the Rear-Section magnetic field is given in table 5.1. In this table, the radial dependency for electrons passing this section is given. Their initial magnetic field and maximum magnetic field are radially independent which leads to an acceptance angle of 92.53°. It is independent of the radius r_{S} and is equivalent to almost full transmission.

The final magnetic field B_{final} at the Rear-Wall is almost identical at all given radii, which results in a pitch angle for electrons of $\approx 128°$ at each radial position. This is the maximum pitch

[1] Release 10.04 including patch 02.

$\mathbf{r_S}$ / mm	$\mathbf{B_S}$ / T	$\mathbf{B_{max}}$ / T	$\boldsymbol{\theta}_{\mathbf{accept}}$ / °	$\mathbf{B_{final}}$ / T	$\boldsymbol{\theta}_{\mathbf{pitch}}$ / °	$\boldsymbol{\theta}_{\mathbf{inc}}$ / °
0	2.522	2.527	92.527	1.588	127.562	179.905
5	2.522	2.527	92.527	1.587	127.569	178.667
10	2.522	2.527	92.527	1.586	127.601	177.357
15	2.522	2.527	92.527	1.584	127.646	176.038
20	2.522	2.527	92.527	1.581	127.729	174.708
25	2.522	2.527	92.527	1.577	127.820	173.366
30	2.522	2.527	92.527	1.571	127.945	172.005
35	2.522	2.527	92.527	1.565	128.081	170.623
40	2.522	2.527	92.527	1.558	128.255	169.215
45	2.522	2.527	92.528	1.550	128.449	167.778

Table 5.1.: *Overview of the properties of the Rear-Section in nominal KATRIN configuration at 70 % magnetic field. The radius r_S indicates the radial starting position of the electron in the center of the Source. The initial magnetic field strength in the Source is given by B_S, and the maximum field strength B_{max}, which the electron experiences during its travel towards the Rear-Wall. The acceptance angle $\theta'_{\mathrm{accept}}$ can be calculated from equation 5.4. Since only electrons traveling to the Rear-Wall are considered, the reduced acceptance angle is given. That means, in KATRIN coordinates, the polar angle to the z-axis is given by $\theta_{\mathrm{accept}} = 180° - \theta'_{\mathrm{accept}}$. The angular distribution ranges from 180° to θ_{accept}. To estimate the scattering probabilities on the Rear-Wall, the inclination angle to the normal of the Rear-Wall plane needs to be known. The maximum angle due to the field change can be derived from B_{final} and is given by the reduced θ_{pitch}. Additionally, the magnetic field lines are not always perpendicular to the Rear-Wall plane. This is expressed by θ_{inc}. An angle of 180° is anti-parallel to the normal. A complete list of properties can be found in the appendix A.I.*

bin edge Source	180°	175°	170°	165°	160°	155°	150°	145°	140°	
bin edge Rear-Wall	180°	176°	172°	168°	164°	160°	157°	153°	149°	
bin edge Source	135°	130°	125°	120°	115°	110°	105°	100°	95°	90°
bin edge Rear-Wall	146°	143°	140°	137°	134°	132°	130°	129°	128°	-

Table 5.2.: *Representation of the bin polar angle edges at the position of the Rear-Wall. The angles are always rounded to integer values and the magnetic field in the Source is assumed to be 2.52 T and at the Rear-Wall 1.58 T. The bin edges are radially dependent as the magnetic field strength varies at the Rear-Wall.*

angle electrons can reach at the Rear-Wall. It is limited by the acceptance angle and magnetic field at the Rear-Wall. The angle for each polar angle bin is calculated using equation 5.3.

The inclination angle, which is defined as the polar angle between the z-axis and the incoming magnetic field line, varies from 168° to 180°. This means an inclination angle of 180° is perpendicular to the Rear-Wall plane or anti-parallel to its normal. Hence, the transmission of electrons, leaving the Source in rear direction, can be described in a radially independent way, but the inclination angle on the Rear-Wall and therefore the scattering probability differs at each radius. The complete list of Rear-Section properties can be found in table A.I in the appendix.

The polar angle in the Source section is distributed within 18 bins with 5° bin width each. The bin edges are also changing while undergoing different magnetic field strengths. An overview of the final distribution is given in table 5.2. From this table one can read that the polar angle distribution is compressed due to the low magnetic field at the Rear-Wall compared to the Source. In addition to the magnetic field change, the inclination angle of the magnetic field line onto the rear- wall plane also changes. The actual incoming angle onto the Rear-Wall is given by a uniform distribution in between $\theta_{\text{inc}} \pm \theta_{\text{bin}}$, with θ_{bin} describing the bin edges at the Rear-Wall shifted by 180°. That means the bin edge 176° is translated to a variation of the incoming angle of $\theta_{\text{inc}} \pm 4°$. Having two bin edges, always the maximum variation is considered. This is a simple model of the real angular distribution.

Both, the bin edge and the inclination angle are radially dependent. The 90° bin edge in the Source is not transmitted to the Rear-Wall, because of the larger acceptance angle of 92.527°. Therefore, only a fraction ($\approx 50\,\%$) of electrons in that polar angle bin are transmitted.

Electrons, reaching the Rear-Wall, are either transmitted or reflected. The reflection can be modelled by a response matrix which is explained in section 5.2.1.2. The reflected particles can travel through the Rear-Section into the Source again. The initial magnetic field of $\approx 1.58\,\text{T}$ and the maximum magnetic field of 2.527 T result in an acceptance angle for electrons to go back towards the Source of 52.25°. Electrons, with a smaller pitch angle, will be transmitted back to the Source while the remaining are magnetically reflected and hit the Rear-Wall again.

5.2.1.1. Uncertainty estimation during the transport

During their travel from the Source exit towards the Rear-Wall, or valve V0 respectively, electrons lose energy due to synchrotron radiation. The amount of radiated energy depends on the pitch angle, kinetic energy and magnetic field. One example is given in figure 5.4. The energy loss is simulated at all radii r_{S}, stated in table 5.1, and the radius having the largest amount of radiated energy is chosen as a conservative estimate for synchrotron losses of all electrons in the Rear-Section. The simulation provides the expected behavior, the smaller the transverse component of the momentum - the smaller the radiated energy.

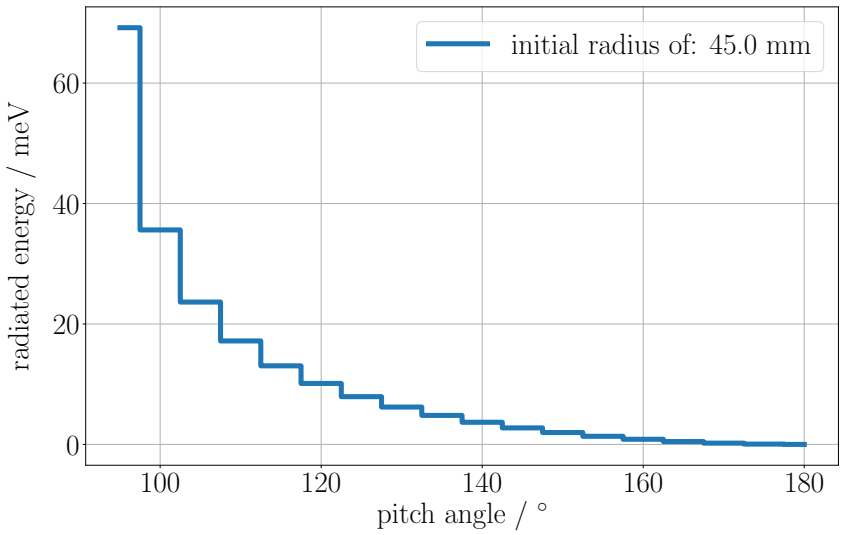

Figure 5.4.: *The synchrotron energy losses of electrons leaving the Source in backward direction until they reach the Rear-Wall at an initial radius inside the Source of 45 mm. The electrons have an initial energy of 18 575 eV.*

In order to simulate the synchrotron radiation for the properties, given in table 5.1, the electrons are created in the center of the Source and tracked towards the Rear-Wall. The energy, these particles lose during their travel inside of the Source, is added afterwards again to calculate the energy losses in the Rear-Section. This induces a small uncertainty as the particle does not have its initial energy while leaving the Source. This effect is less than a per mille on the energy and therefore not considered. This approach is used to simulate the radiation losses at the correct radial position according to table 5.1.

The electron can also interact with residual gas inside of the Rear-Section and thereby lose energy, change the pitch angle, or get stuck in varying magnetic fields. This is not considered in the uncertainty estimation. Additionally, super-conducting magnets might change their expected position slightly during cooling. These uncertainties in their absolute positioning are not considered. The effects are presumed to be negligible, but should be investigated in more detail in future.

5.2.1.2. Rear-Wall Response Matrix

To simulate the response matrices for the gold-plated Rear-Wall, the GEANT4 toolkit is used. The energy and polar angle binning for the Rear-Section response matrices calculation is kept identical to that of the Source section, although, table 5.2 suggests to go to a finer binning of the polar angle in the order of 1°. This would infer five times more bins, which also requires at least five times the amount of initial events for the same precision per bin. This is computationally too expensive considering the gain achieved in simulating the FBM response.

A simplification to previous simulations is the smaller polar angle range from 180° to 90°. For the simulation process, a cuboid shaped volume out of gold is used and 10^6 electrons are shot onto it at each angle and energy bin. The scattering probability thereby depends strongly on the incoming angle as well as the energy. The simulation result is shown in figure 5.5. It shows that electrons with increasing kinetic energies are more likely to scatter. The larger the polar angle is, the smaller the probability of electrons to scatter off the Rear-Wall. This is because

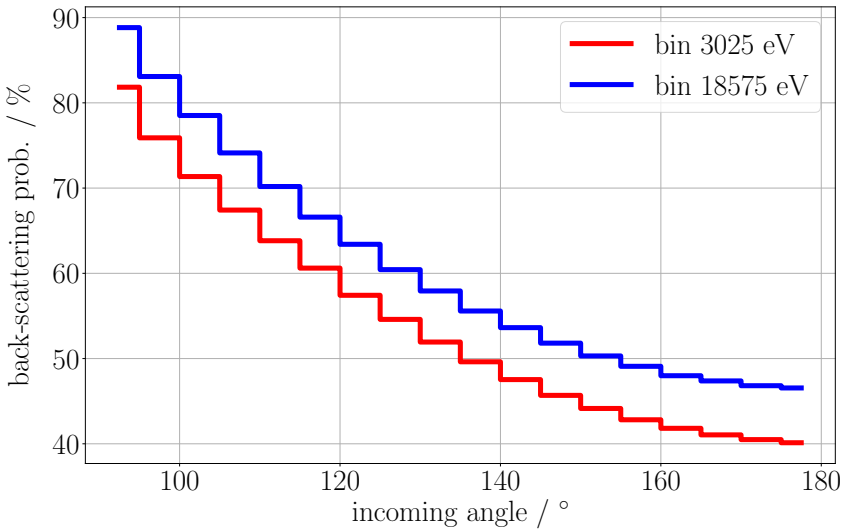

Figure 5.5.: *The probability of an electron to backscatter from the gold-plated Rear-Wall at different inclination angles. The angle of 180° is perpendicular to the plate while 90° is parallel. The data in this figure is simulated using an isotropic distribution within an angular bin and a uniform distribution within an energy bin.*

the larger the angle - the smaller the parallel component of the momentum towards the gold plate.

In order to simulate the response matrices for the Rear-Wall, the Penelope physics package is used [SFS06]. It is embedded in GEANT4 specifically for low-energetic electrons and positrons [All+16]. The error is assumed to be 10 % on the cross-section [PAC15]. In GEANT4 the interaction probability $P(l)$ is calculated in a similar way compared to the Source interaction probabilities [Ago+03]:

$$P(l) = \exp\left(-n_\lambda\right) = \exp\left(-\int_0^l dl/\lambda(l)\right). \tag{5.5}$$

Therefore, instead of varying the cross-section, the density of the target material is varied by 10 %. The variation is also done for the backscattering simulation shown in figure 5.5. It affects the backscattering probability by less than 0.5 % and is therefore not considered. Besides the backscattering probability, it also affects the mean energy of the backscattered electrons:

$$\begin{aligned} E &= 17\,580\,\text{eV} \qquad \text{for } \lambda^{-1} = 1.0 \cdot \lambda^{-1}_{\text{nominal}} \\ E &= 17\,597\,\text{eV} \qquad \text{for } \lambda^{-1} = 0.9 \cdot \lambda^{-1}_{\text{nominal}} \\ E &= 17\,567\,\text{eV} \qquad \text{for } \lambda^{-1} = 1.1 \cdot \lambda^{-1}_{\text{nominal}} \end{aligned}$$

The initial electron energy ranges from 18 550 eV to 18 600 eV. For higher densities, the interaction probability is larger and therefore the electron loses more energy on average and vice versa for lower densities. The relative difference is therefore below 0.2 % in energy, and 0.6 % for the mean reflected angle.

To evaluate the error made by the rather large binning of 5° for the response matrix calculations, the bin of 125° to 130° is compared to a 1° degree binning from 128° to 129° according to table 5.2. This bin is chosen, because the probability of scattering is the largest while the bin width is the smallest. The electron energy ranges from 18 550 eV to 18 600 eV, because the probability of scattering increases with larger electron energies (compare figure 5.5). While the

r_S / mm	B_S / T	B_{max} / T	θ_{accept} / °	B_{final} / T	θ_{pitch} / °	θ_{inc} / °
0	2.522	2.526	92.487	0.246	161.807	179.617
5	2.522	2.526	92.487	0.245	161.840	176.308
10	2.522	2.526	92.487	0.243	161.938	172.543
15	2.522	2.526	92.487	0.238	162.105	168.713
20	2.522	2.526	92.488	0.233	162.342	164.790
25	2.522	2.526	92.488	0.224	162.660	160.740
30	2.522	2.526	92.488	0.214	163.065	156.530
35	2.522	2.526	92.488	0.202	163.565	152.119
40	2.522	2.526	92.488	0.188	164.175	147.467
45	2.522	2.526	92.488	0.171	164.913	142.523

Table 5.3.: *Overview of the individual properties in the Rear-Section during First Tritium. A detailed explanation is given in table 5.1. In this configuration the Rear-Section magnet is off and valve V0 is closed. Therefore, the magnetic field strength at V0 is small compared to nominal KATRIN operation, which leads to a large pitch angle, but a small inclination angle towards the z-axis.*

effect is less than half a percent on the mean reflected polar angle and energy bin, it still shifts the mean reflected energy by one bin. For the normal binning the mean reflected energy is 15 345 eV and for the smaller binning 15 294 eV.

5.2.2. First Tritium operation

During First Tritium operation valve V0 in the Source was closed and the Rear-Section magnet was turned off. An overview of the setup is given in the appendix A.III. Therefore, the properties of the transmission in the Rear-Section change compared to nominal KATRIN operation. Additionally, the backscattering probability at valve V0, which is made of stainless steel, is different to the Rear-Wall and the scattering response matrices need to be simulated.

An overview of the transmission properties is given in table 5.3. The values are comparable to table 5.1. The maximum magnetic field is slightly lower by 1 mT compared to the nominal configuration, therefore the acceptance angle decreases slightly while the amount of transmitted electrons is increased. The magnetic field at V0 is only at ≈ 200 mT, hence the pitch angle θ_{pitch} is larger with more than 160° at all radii compared to the nominal configuration.

As the Rear-Section magnet is switched-off, the magnetic field at V0 diverges. While the inclination angle θ_{inc} is almost 180° and can be considered anti-parallel to the V0-plane normal in the center, it changes to 143° at the maximum radius r_S. As explained in the previous section, the actual polar angle of the incoming electron onto valve V0 is simulated by a uniform distribution in $\theta_{\text{inc}} \pm \theta_{\text{bin}}$ with θ_{bin} being the bin edges represented by the magnetic field at valve V0, and shifted by 180°. Due to the low magnetic field at V0, the pitch angles are large ($> 160°$) and the bin edges originating from the Source are compacted into a polar angle range of 180° to 160° as given in table 5.4. Therefore, all electrons, originating from the Source, are compressed within four polar angle bins for simulating the valve V0 response matrices. This low magnetic field at V0 also causes back-reflected electrons from valve V0, which have a polar angle larger than 16.76°, to be magnetically reflected back to V0 and not to be transmitted to the Source.

On their travel towards valve V0, electrons also radiate synchrotron radiation. As the magnetic field is slightly lower than in nominal KATRIN operation (compare section 5.2.1.2) and

bin edge Source	180°	175°	170°	165°	160°	155°	150°	145°	140°
bin edge V0	180°	178.5°	177.1°	175.7°	174.3°	173.0°	171.7°	170.5°	169.3°
bin edge Source	135°	130°	125°	120°	115°	110°	105°	100°	95°
bin edge V0	168.2°	167.2°	166.3°	165.5°	164.8°	164.3°	163.8°	163.5°	163.3°

Table 5.4.: *Representation of the bin edges at the position of V0 of the Source bin edges. The angles are always rounded to the first decimal place and the magnetic field in the Source is assumed to be 2.52 T and 0.21 T at V0. The bin edges are radially dependent as the magnetic field strength varies at V0. The bin edge of 90° in the Source is not considered as it is below the acceptance angle.*

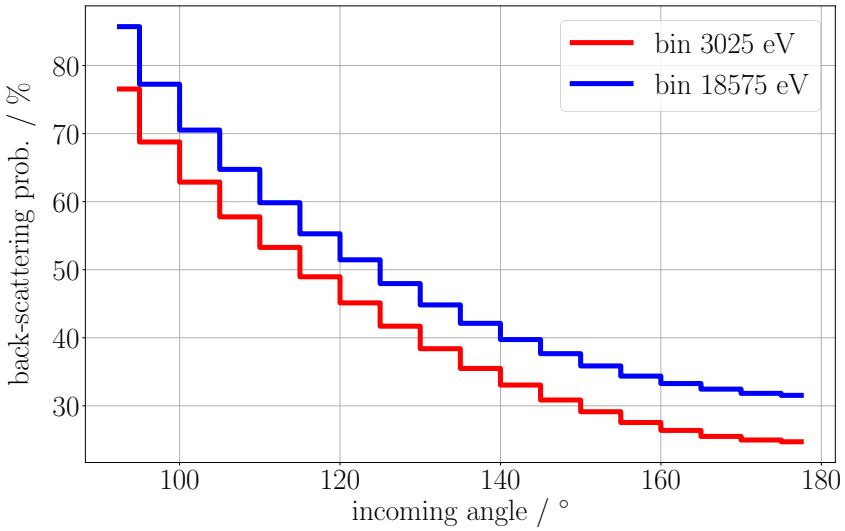

Figure 5.6.: *The probability of an electron to backscatter from valve V0 at different inclination angles. The angle of 180° is perpendicular to the valve while 90° is parallel. The figure is simulated using a uniform distribution in* $\cos(\theta)$ *within an angular bin and a uniform distribution within an energy bin.*

the travel distance of the electron is smaller, the estimate given in figure 5.4 also holds for the First Tritium measurement phase.

5.2.2.1. Valve V0 Response Matrix

In contrast to the Rear-Wall, valve V0 (VAT-valve 10848-CE24 [Stu18]) is made out of the stainless steel alloy AISI 316L [VAT18]. This alloy is implemented into GEANT4 for this work using the material list from reference [Mat18].

In order to simulate the response matrices, the energy and polar angle binning is kept identical to the binning used in the Source. To resolve the different scattering behaviors for all bin edge representations, given in table 5.4, the polar angle bin width needs to be 0.1°. This is computationally too expensive to simulate. Therefore, keeping identical polar angle binning, all interactions are represented by four angular bins, but the simulation needs to be performed from 90° to 180° as reflected electrons (with a polar angle range of 0° to 90°) may have large polar angles up to 90°. These are magnetically reflected and hit valve V0 again.

To simulate the interaction of electrons with the valve, the Penelope physics package is used. The probability of scattering at different incoming polar angles of the lowest, as well as the highest energy bin is shown in figure 5.6. The trend of the figure is comparable to that of

r_S / mm	B_S / T	B_{max} / T	θ_{accept} / °	B_{final} / T	θ_{pitch} / °	θ_{inc} / °
0	2.522	3.976	52.781	0.879	28.053	0.071
5	2.522	3.976	52.781	0.878	28.031	0.075
10	2.522	3.976	52.781	0.875	27.974	0.079
15	2.522	3.977	52.781	0.870	27.882	0.082
20	2.522	3.977	52.780	0.862	27.755	0.087
25	2.522	3.977	52.780	0.853	27.592	0.089
30	2.522	3.979	52.759	0.842	27.385	0.091
35	2.522	3.982	52.725	0.829	27.136	0.094
40	2.522	3.987	52.685	0.813	26.848	0.094
45	2.522	3.991	52.641	0.796	26.518	0.090

Table 5.5.: *Overview of the properties of the setup for electrons traveling from the Source to the FBM. A detailed description of the properties is given in table 5.1. The difference is that electrons travel along the z-direction upstream towards the FBM which leads into polar angles smaller than 90°. They experience a larger maximum magnetic field and therefore more electrons get reflected back to the Source as compared to the Rear-Section. Additionally, the magnetic field lines are almost parallel to the FBM plane normal and therefore the inclination angle is negligible compared to the pitch angle. The complete table can be found in the appendix A.III.*

figure 5.5, the higher the incident kinetic energy - the larger is the scattering probability. With decreasing polar angle, the probability of scattering increases to more than 80 %. However, the general probability of reflection is smaller than for the Rear-Wall.

For a radius of $r_S = 0$ mm and an inclination angle of almost 180°, the incoming polar angle is between 163° to 180° and therefore the reflection probability is low with less than 30 % for all energy bins. The reflection probability increases with larger radii due to the decreasing inclination angle of the magnetic field line.

To estimate the error, the density of the stainless steel target is shifted by 10 % according to equation 5.5. The effect on the backscattering probability is less than 0.5 %. The mean reflected energy is:

$$\begin{aligned} E &= 17\,514\,\text{eV} \qquad \text{for } \lambda^{-1} = 1.0 \cdot \lambda^{-1}_{\text{nominal}} \\ E &= 17\,530\,\text{eV} \qquad \text{for } \lambda^{-1} = 0.9 \cdot \lambda^{-1}_{\text{nominal}} \\ E &= 17\,498\,\text{eV} \qquad \text{for } \lambda^{-1} = 1.1 \cdot \lambda^{-1}_{\text{nominal}} \end{aligned}$$

considering the bin with the largest scattering probability - which is the largest energy bin of 18 575 eV and the smallest polar angle bin of 92.5°. It is shifted on the per mille level. The same holds for the mean reflected polar angle. To investigate the effect of angular bin widths, the bin with a polar angle of 165° to 160° is compared to the bin with an angle of 163.3° to 163.5° at the highest electron energy of 18 575 eV, which has the largest probability of backscattering. The mean energy of backscattered electrons with the nominal binning is 13 210 eV and 13 192 eV for the small binning. The mean reflected angle differs on the per mille level.

5.3. Transport-Section

Electrons leaving the Source in forward direction of the experiment, i.e. along the z-axis with a polar angle of $\leq 90°$, travel through the Transport-Section, namely through the DPS and CPS,

bin edge Source	0°	5°	10°	15°	20°	
bin edge FBM	0°	3°	6°	9°	11°	
bin edge Source	25°	30°	35°	40°	45°	50°
bin edge FBM	14°	17°	19°	22°	24°	26°

Table 5.6.: *Representation of the polar angle bin edges at the position of FBM of the initial Source bin edges. The angles are always rounded to integer values and the magnetic field in the Source is assumed to be 2.52 T while at the FBM 0.84 T. The bin edges are radially dependent as the magnetic field strength varies at the position of the FBM. The bin edges of above 50° in the Source are not considered as these are larger than the acceptance angle.*

until they arrive at the position of the FBM in pump-port 2 of the CPS at $z \approx -18.3\,\mathrm{m}$.

An overview of the Transport-Section is given in the appendix A.IV. Some electrons, travelling through the Transport-Section, will hit the FBM detector while others travel along towards the spectrometer side and leave the Transport-Section.

The properties of the Transport-Section for electrons can be seen in table 5.5. Electrons, originating from different radii in the center of the Source are stated with their initial magnetic field B_S which is identical for all radii in the referenced table. On their travel through the Transport-Section they experience different maximum magnetic fields B_{max}. The maximum difference of the field is 0.5 %. According to equation 5.4, the acceptance angle θ_{accept} can be calculated.

In contrast to the previous section, the electrons travel in forward-direction, which means that all electrons leaving the Source with a polar angle of approximately 0° to 52.7° are transmitted through the Transport-Section and can reach the FBM or the spectrometers.

Since pump-port 2 is not surrounded by a super-conducting magnet at the FBM location, the magnetic field drops, and due to the conservation of the magnetic flux (compare equation 5.6), the effective magnetic flux area expands. Hence, the radial offset of the incoming magnetic field line guiding the electrons also expands. The drop in magnetic field at the position of the FBM compared to field in the Source results in a small pitch angle θ_{pitch}. Electrons arriving from the Source are distributed in a small angular window of approximately 0° to 28°. The distribution for each bin edge can be seen in table 5.6.

As the FBM detector board is centered in pump-port 2, the magnetic field lines are aligned almost perfectly anti-parallel to the FBM plane with an inclination angle of the magnetic field line of $< 0.1°$ (compare table 5.5), because it is in between two coaxially aligned magnets. Therefore the inclination angle can be neglected for further simulations and electrons are only distributed in their angular bin according to table 5.6.

Due to the small acceptance angle of $\approx 52.7°$ many electrons leaving the Source in the forward direction are magnetically reflected back to the Source. That means 61 % of electrons are reflected before they reach the FBM considering an isotropic distribution of electrons between 0° to 90° in the Source.

Nevertheless, these electrons travelling through the Source with an initial pitch angle above the acceptance angle, might scatter at the gas molecules and leave the Source in forward direction, but with a smaller pitch angle and still reach the FBM detector.

Electrons, backscattering from the FBM diodes, have pitch angles in the range of 180° to 90° while the magnetic field at the FBM is comparably small with 0.8 T. Hence, many of those

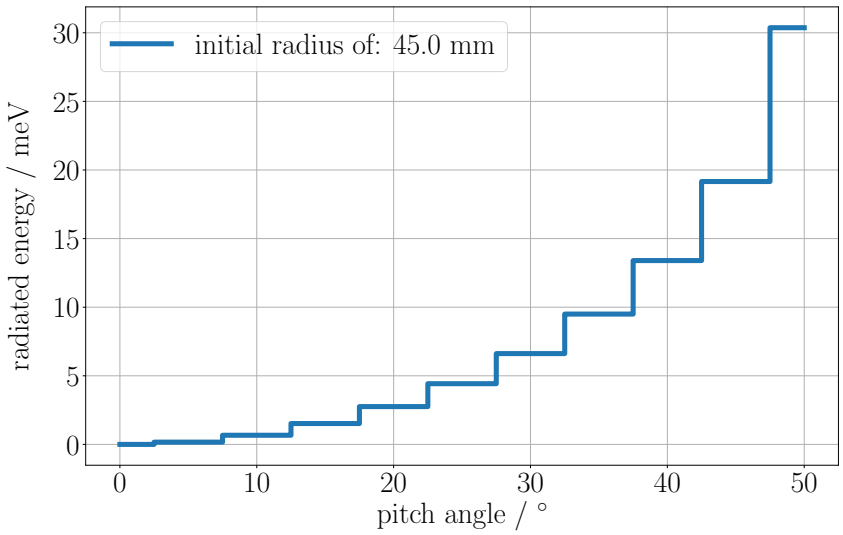

Figure 5.7.: *The synchrotron radiation of electrons leaving the Source in the forward direction until they reach the FBM detector at an initial radius of 45 mm inside of the Source. The electrons have an initial energy of 18 575 eV.*

electrons are magnetically reflected in the Transport-Section again and return to the FBM. The acceptance angle for this case is 153.36°. Therefore, electrons backscattered from the FBM with an angle of 180° to 153.36° are transmitted to the Source (11 %), while 89 % of the remaining particles hit the FBM again for an assumed isotropic pitch angle distribution in 90° to 180° for the backscattered electrons from the diode in this calculation.

5.3.1. Uncertainty estimation

During their travel from the Source to the FBM, the electrons emit synchrotron radiation. The amount of radiated energy depends on the pitch angle of the electron, its kinetic energy and the magnetic field it experiences. An example is shown in figure 5.7. It shows the amount of radiated energy from particles leaving the Source at different pitch angles. This simulation is done for all initial radii in the Source and as an upper estimate the track with largest emitted radiation is chosen. It has a starting radius r_S in the Source of 45 mm.

In order to simulate the emitted radiation, electrons are started in the center of the Source at an energy of 18 575 eV and tracked along their respective magnetic field lines to the FBM. As discussed in section 5.1.2, the radiation the particle lost during its travel to the exit of the Source is added again. This means that the initial kinetic energy at the exit is slightly lower than 18 575 eV. However, this effect is negligible. The electrons are generated in the center of the Source and not at the exit because the magnetic field lines are diverging at the Source exit as a pump-port is attached and therefore no guiding super-conducting magnet.

Looking at the absolute scale of radiated energy in figure 5.7 one expects it to be larger than for the Rear-Section given in figure 5.4, because the track length is longer and the electron undergoes larger magnetic fields. However, the acceptance angle is much smaller in the Transport-Section which leads to smaller pitch angles at which electrons can arrive at the FBM. A pitch angle in the Transport-Section of 50° is equivalent to a pitch angle of 130° in the Rear-Section and the radiated energy is about three times larger in the Transport-Section than in the Rear-Section.

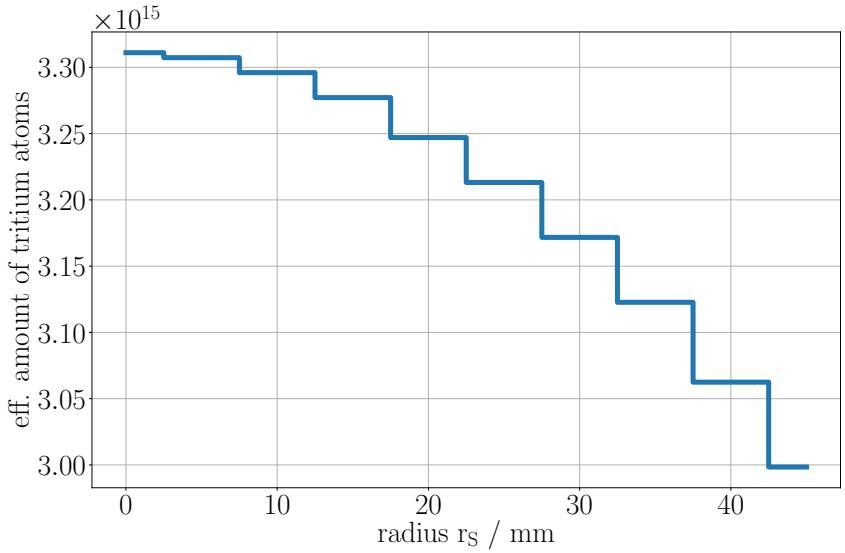

Figure 5.8.: *The number of tritium atoms the FBM observes per 1 mm² at various radii. The gradient is proportional to the magnetic field drop at the position of the FBM.*

5.3.2. Effective amount of tritium atoms

In order to calculate the electron rate at the FBM at different positions, the number of tritium atoms in their corresponding Source volume needs to be known. The Source has a column density of $5 \cdot 10^{21}\,\mathrm{m}^{-2}$ [KAT05]. This is equivalent to $9.5 \cdot 10^{15}$ tritium atoms in the Source per $1\,\mathrm{mm}^2$ at a tritium purity of $\epsilon_\mathrm{T} = 0.95$. The effective amount of tritium atoms the FBM detector observes depends on the magnetic field at the FBM position due to the conservation of magnetic flux:

$$\Phi = \int B dA \tag{5.6}$$

Therefore, the effective area A_S the FBM detector observes in the Source can be calculated as:

$$A_\mathrm{S} = \frac{B_\mathrm{final}}{B_\mathrm{S}} \cdot A_\mathrm{diode} \tag{5.7}$$

according to table 5.5. For an effective diode size of $1\,\mathrm{mm}^2$ this results in the radial dependency of the amount of tritium atoms given in figure 5.8. Therefore, the rate drops with increasing radii during tritium measurements. The error on the rate in this calculation is, according to equation 5.7, proportional to the variation of the magnetic field at the FBM position and anti-proportional to the variation of the magnetic field in the Source.

During First Tritium measurements the tritium purity was $\epsilon_\mathrm{T} \approx 0.005 = 0.5\,\%$. Therefore the effective amount of tritium atoms needs to be corrected for that value.

5.4. Forward Beam Monitor cover

To protect the FBM detector board from the electron beam, the electronics are enclosed by a stainless steel cover. It is made from AISI 316LN and fully covers the front and the sides of the detector board. Five holes are drilled into the front, two of them for fixing the board with screws, one for a LED located on the board and two for the *p-i-n*-diodes. For this section, only the two holes utilized by the diodes are of interest and their impact onto the measured detector

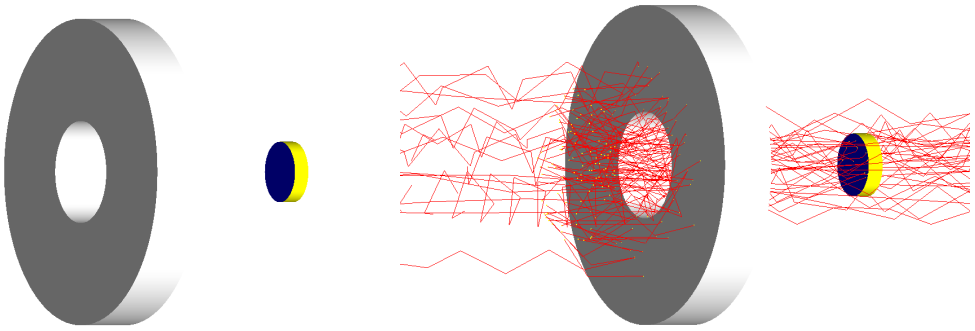

(a) Cover (left) and diode (right). **(b)** Simulation of 100 electrons.

Figure 5.9.: *GEANT4 setup.*

signal. All information, given in this section about the geometrical setup of the cover and the material is derived from its corresponding CAD drawings [Ell18].

Electrons, reaching the FBM, experience a magnetic field of approximately 0.8 T in the First Tritium configuration. They follow their magnetic field lines and therefore perform cyclotron motion. Hence, they can interact with the stainless steel cover, lose energy, produce secondaries, or change the momentum direction of the electron. To investigate this effect, the GEANT4 toolkit is used and the setup is modelled in that toolkit. The holes in the FBM cover, for the diodes, have a diameter of 2 mm and the thickness of the cover is 1 mm. The distance of the diode to the cover is set to 6 mm.

5.4.1. Simulation model

A simple model is created with the GEANT4 toolkit and the experimental configuration is visualized in figure 5.9. The cover is simplified and replaced by a tube with a total diameter of 6 mm and a hole of 2 mm in diameter. The dimensions are appropriate for the size of the diodes and expected Larmor radius. It has a thickness of 1 mm.

The detector is colored in yellow and blue in figure 5.9, with blue denoting the dead-layer and yellow the sensitive volume of the diode. For simplicity in this simulation, the full detector response is not simulated, but only the transmission through the hole as well as the energy and coordinates at transmission point of the particle. This is done to investigate the effect of the cover rather than that of the detector response.

The FBM detector board can be equipped with differently sized diodes. During First Tritium measurements in KATRIN the largest diode Hamamatsu S5971 was used. The largest diode can also be used as a conservative ansatz to estimate the effect of scattered electrons, or of secondaries hitting the detector. This diode has an effective size, according to Hamamatsu of 1.1 mm^2 [Ham11], but the measured visible detector size is $(1.35 \pm 0.05)\,\mathrm{mm}^2$. The latter is utilized in the simulation. Measurements with an electron-gun in the KATRIN setup also indicate a larger effective diode size (compare to figure 5.12).

Besides investigating the perfectly aligned diode to the hole (i.e. perfectly centered), it might happen that during the assembly of the board, the diode has an offset in position. To compensate for that, the diode is moved off-center to different position in the simulation. In order to not redo the simulation at each position of the diode, the diode is extruded so that all electrons passing the hole of the cover are stored into ROOT trees. The detector dimensions are applied afterwards in the analysis of the simulation. This also allows the simulation to be performed

with a larger number of initial electrons.

The initial electrons are generated in different energy bins, i.e. 18 575 eV, 9025 eV, and 3025 eV and are uniformly distributed in their 50 eV bin as described in the previous sections. The pitch angle is distributed isotropically from 0° to 30° and the electrons follow the 0.8 T strong magnetic field as shown in figure 5.9 (b).

To investigate effects of the interaction with the cover, the origin of electrons is uniformly generated in a circular plane with a radius of 2 mm, which is a factor of two larger than the actual hole. To generate a sufficient number of events, $5 \cdot 10^7$ electrons are generated in this plane. For the interaction model the Penelope physics package is used.

5.4.2. Simulation results

The results of the simulation are shown in figure 5.10. At first, the virtual diode is perfectly centered to the hole in the cover, which is denoted with an offset of 0 mm in all sub-figures. It is shifted along the x-axis in 0.1 mm steps to place the diode at different offsets.

In figure 5.10 (a) the fractions of primary particles that are lost by not perfectly aligning the diode to the cover are shown. The number of particles that reach the perfectly centered detector are set as the normalization factor to calculate the fraction of particles that reach the detector at different detector positions. This simulation is done for various energy bins as the Larmor radius depends on the transverse component of the momentum and the interactions with the stainless steel cover differ at different kinetic energies.

In figure 5.10 (a), all energy bins show a similar behavior and an offset of up to 0.5 mm still allows more than 80 % of primaries to reach the detector. The Larmor radius for electrons with 18.6 keV in a magnetic field of 0.8 T and with a polar angle of 30° is approximately 0.3 mm. Therefore, the loss of primaries is caused by electrons hitting the cover due to their cyclotron motion. As expected, the fraction of primaries drops down to 0 % after the diode is fully covered with an offset larger than 1.5 mm.

In figure 5.10 (b) the fractions of the primary electrons, that reach the detector shown in figure (a), but scattered at the cover are shown. The lowest energy bin of 3025 eV is not shown in figure (b) to (d), because the threshold for this simulation is set to 3000 eV and electrons that scatter off the cover, or produce secondaries, are likely to fall below the given threshold.

Furthermore, the fraction of scattered primaries is 1 % for the 18 575 eV bin and 0 % for the 9025 eV bin up to 0.4 mm. At 1 mm offset the fraction is in the order of 4 %.

In figure 5.10 (c) the fraction of secondaries normalized to the number of primaries in the respective offset bin is given. Secondaries can originate from e.g. ionization of the atoms in the cover or Bremsstrahlung. The total fraction of secondaries is negligible for the overall detector response as the fraction is below 0.3 % at all offsets. The drop in fraction at 1.8 mm offset is caused by a low number of events reaching the detector. In this particular bin, only one secondary is detected. This is reasonable as only photons are able to reach the position of the diode at such a large offset in position.

In figure 5.10 (d) the relative number of photons to the total number of secondaries reaching the detector is given. Therefore, at small offsets, the fraction of photons is rather large with up to 33 %. Secondary electrons follow their respective magnetic field line while photons are able to hit a centered diode. At an offset from 0.5 mm to 1.3 mm the secondaries are dominated by electrons. At larger offsets the board is covered and electrons are not able to reach the detector, therefore these are dominated by photons. The two largest offset bins contain only one event.

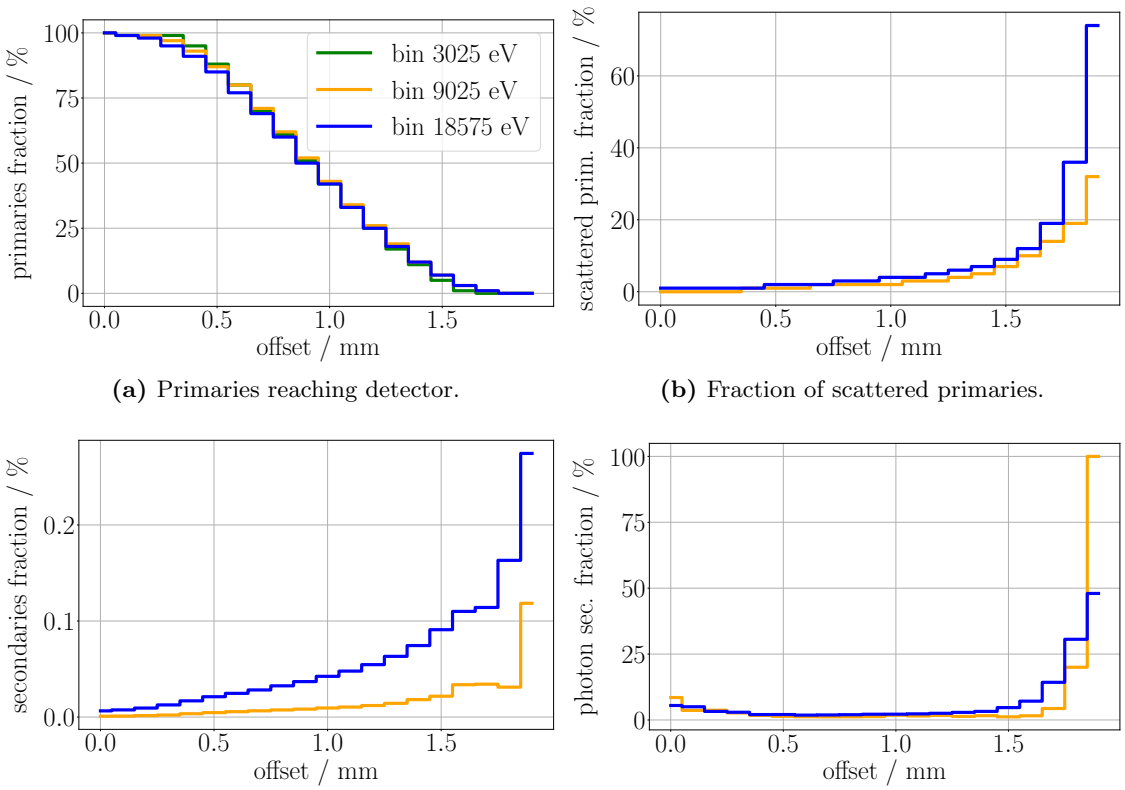

(a) Primaries reaching detector.

(b) Fraction of scattered primaries.

(c) Secondaries reaching detector.

(d) Fraction of photons in secondaries.

Figure 5.10.: *The probability for electrons to reach the FBM detector through the cover at different positions (offsets). Figure (a) shows the fraction of initial primary particles reaching the detector, where the fraction is normalized to the number of particles reaching the detector when it is perfectly centered at an offset of 0 mm. While figure (a) shows the integrated sum of primaries, figure (b) gives the number of primaries that reach the detector, but do interact with the cover and thereby lose energy. These are normalized to their corresponding offset bin in figure (a). Electrons interacting with the cover might produce secondaries. Their fraction, normalized to the number of primaries, with the same offset is given in figure (c). Not only electrons are produced as secondaries, but photons as well. Their fraction, normalized to the total number of secondaries, is given in figure (d).*

Backscattered electrons

As will be discussed in the next section 5.5, electrons may scatter off the diode and the polar angle of the reflected electron is therefore in the range of 90° to 180°. According to reference [Ren11], the mean reflected polar angle for an incident polar angle of 30° is 135°. This is equivalent to a Larmor radius of about 0.4 mm and therefore only one tenth of a millimeter larger than for incoming electrons.

Electrons might be reflected at almost 90°. This is equivalent to a Larmor radius of approximately 0.6 mm. These electrons are likely to scatter at the cover, if their origin is close at the rim of the diode. They might return to the diode with an altered kinetic energy and polar angle or leave the enclosed FBM board. As the probability of backscattering for electrons is on the order of 20 % and large transverse momenta of the reflected electrons are suppressed (compare [Ren11]), a few percent of the reflected electrons have a larger transverse momentum than the incoming electrons. Additionally, the origin of electrons needs to be in the outer rim of the diode, therefore all reflected electrons are assumed to be transmitted through the hole in the cover.

5.4.3. Conclusion

In this section the necessity to center the diodes as well as possible was shown. A maximum offset of 0.5 mm is the precision that should be achieved with the largest diodes of 1.35 mm^2 effective size. For future tritium measurement campaigns smaller diodes will be used as the electron rate will be higher. The required precision of centering the diode will therefore be smaller. This GEANT4 simulation can be seen as an upper estimate of the effects caused by the cover, the pitch angle in the simulation is 2° larger than in the actual setup, and for future measurements smaller diodes are used.

In this work, the diodes are assumed to be centered with a precision better than 0.5 mm and response matrices are not utilized for the cover. But this section shows that for Hamamatsu S5971 diodes it is reasonable to increase the diameter of the cover hole. Otherwise, the influence on the rate and energy resolution is not negligible if the diode is not perfectly centered.

5.5. p-i-n-diode response

Electrons, that pass the cover and hit the diode in its sensitive area, have to surpass the deadlayer to get into the sensitive volume in order to be detected. While travelling through the deadlayer they lose energy depending on their initial energy and inclination angle. The KATRIN collaboration developed the KATRIN Electron Scattering in Silicon code (KESS) framework to simulate the response of diodes. For this purpose the GEANT4 toolkit can also be used, but it did not achieve the required precision in the past [Ren11]. Further improvements in the low energy regime (keV range) were implemented into GEANT4. Comparisons between GEANT4 and KESS were done in the course of this work and the results using the Livermore or Penelope package were comparable to KESS.

Nevertheless, at electron energies below 5 keV, the probability of electron reflection in the silicon differs between both of them. Additionally, the KESS code performance exceeds GEANT4 for the same number of events which cannot be underestimated in order to simulate the response matrices.

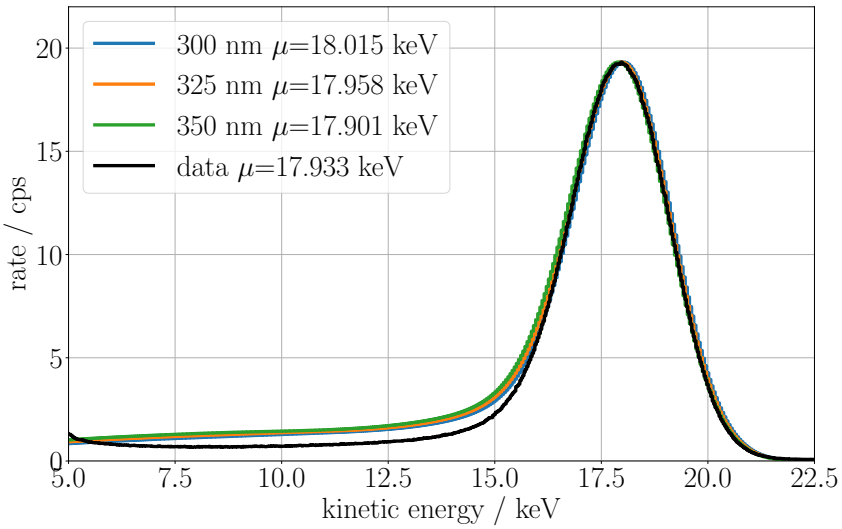

Figure 5.11.: *An electron-gun measurement during the STSIIIa phase of KATRIN. Additionally, the expected detector response with an energy resolution of 2.5 keV at different dead-layer depths is shown and the fitted peak position is shown additionally in the legend.*

5.5.1. Simulation model

Measurements with an electron-gun have shown that the utilized Hamamatsu diodes have a dead-layer on the order of 330 nm [Ell19]. However, these values vary for each diode. In order to make up for that fluctuation, the diode response is simulated with a dead-layer of 300 nm, 325 nm, and 350 nm.

As discussed in previous sections, the energy is varied in 50 eV steps from 3 keV to 18.6 keV. To fit the requirements of the FBM detector in pump-port 2 of the CPS, the KESS code was edited in the course of this thesis. Electrons, reflected off the detector with a pitch angle larger than the acceptance angle, for transmission to the Source, are magnetically reflected back onto the detector. As simulations have shown, the reflection occurs in less than 1 µs and therefore the electron is accounted as being within the same event as the initial energy deposition of the same primary electron. Hence, the deposited energy of the reflected electron counts as the same event in the detector. This changes the shape of the detected signal and also the detection efficiency. Electrons with smaller pitch angles than the acceptance angle are transmitted to the Source.

In the simulation the pitch angle of the incoming electron is varied from 0° to 30° in 5° steps. Electrons that scatter off the diode with a pitch angle larger than the acceptance angle are accounted for in the KESS simulation already and therefore no response matrices have to be calculated above a polar angle of 30°.

During the STSIIIa measurement phase of KATRIN in September 2018, electrons were emitted from an electron-gun with an initial energy of 18.6 keV onto the FBM. The data and different dead-layer simulations are shown in figure 5.11. The mean of the peak with $\mu_{\text{measured}} = 17.933\,\text{keV}$ is best represented by a dead-layer of 325 nm with $\mu_{\text{simulated}} = 17.958\,\text{keV}$ which is set as the nominal value. Utilizing a dead-layer of either 300 nm, or 350 nm respectively leads to a shift in the mean energy of approximately one bin at 18.6 keV at a bin width of 50 eV.

KESS itself stores data in ROOT trees so that each event can be accessed. This is not useful for simulating response matrices for each bin. The code had to be changed in order to create response matrices. Electrons, which are reflected are stored in a two dimensional histogram (re-

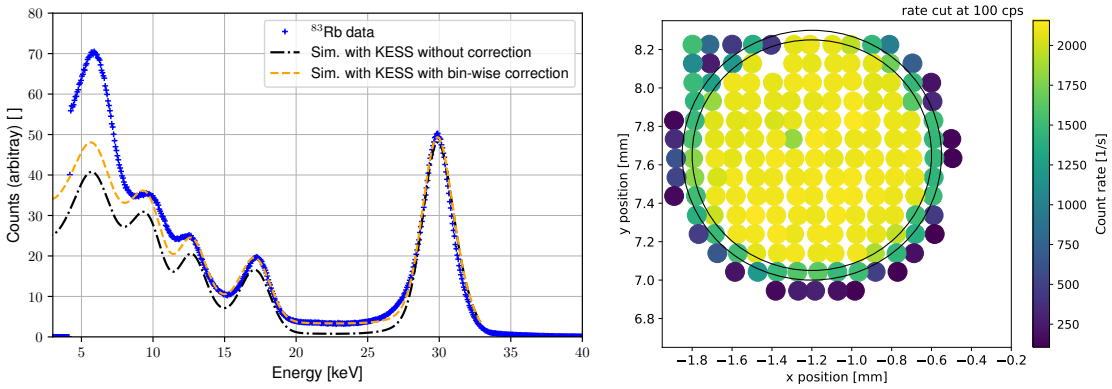

(a) Rb spectrum with correction.

(b) Rate distribution along the *p-i-n*-diode.

Figure 5.12.: *The numerical model used in this thesis to describe the response of the diodes is shown. In figure (a) the applied correction to describe the measured rubidium spectrum with the p-i-n-diode S5971 is shown. This is motivated by figure (b) in which a scan of the diode in 0.1 mm steps is visualized. The most-inner ring visualizes the expected size of 1.1 mm^2 and the outer ring the actual ring size where electrons are detected. The outer part of the detector leads to an increased plateau-like structure. Figures taken and more information about the model to be found in reference [Ell19].*

flected energy and polar angle bin) as already used in previous sections. The second histogram, representing the deposited energy is one dimensional, because information about the polar angle is lost in the diode. The polar angle is still represented by differently deposited energies of the electron. The histogram represents the fraction of electrons depositing their energy in the sensitive volume per energy bin.

The BetheFano interaction model, implemented in KESS, is used in the simulation and electrons are tracked until they reach a minimum energy of 110 eV before they deposit their remaining energy locally. Each energy and polar angle bin is simulated with 10^6 initial electrons.

There are different methods to model the dead-layer. In this work, electrons depositing energy in the dead-layer have no effect on the detected signal. Hence, there is a hard cut between the dead-layer and sensitive volume. For the FPD (Focal Plane Detector) wafer, a different ansatz was used. The dead-layer is assumed larger than measurements indicate for a hard cut between dead-layer and sensitive volume. In this method 46 % of the energy deposited in the dead-layer actually contributes to the detected signal [Wal+14].

This ansatz for the FBM has proven to underestimate plateaus of rubidium spectra taken with the FBM detector and to overestimate the plateau of the electron-gun peak. However, a numerical model was developed in [Ell19] to perform a correction of the underestimation that is also apparent in the hard cut model. This is discussed in the following section.

5.5.2. Modelling of the rim

This section is based on the work presented in [Ell19]. The Rubidium spectra measured with the Hamamastu S5971 diode could not be simulated in KESS to get the correct response. This can be seen in figure 5.12 (a). The simulation, normalized to the 30 keV peak, underestimates the plateaus each peak creates. The idea of the model is that peaks at lower energies are placed on top of the plateau and are therefore lifted. These plateaus are created by higher energy electrons. A numerical model is introduced based on 5.12 (b), which is a scan of the diode with

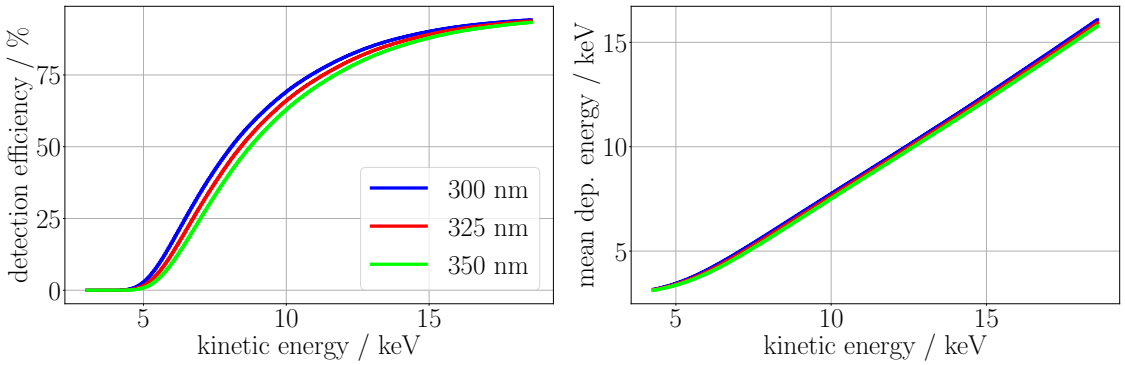

(a) Detection probability. **(b)** Mean deposited energy.

Figure 5.13.: *Overview of the detection probability of electrons in a certain energy bin (a), and the mean deposited energy for each bin (b) at different dead-layer thicknesses.*

an electron-gun spot in 0.1 mm steps. Each dot represents the count rate at that position. The inner ring thereby represents the diameter of the sensitive area stated by Hamamatsu [Ham11], but electron counts are still detected beyond the sensitive area. In that rim, the electrons are only partially collected which creates a plateau like structure emphasizing the numerical model.

The idea of the model is that each bin contributes with a certain fraction to the plateau like structure. The factor for KESS simulations is $1.19 \cdot 10^{-3}$ [Ell19] added to the energy distribution created by KESS of each energy bin. In other words, each bin adds a plateau of its amount of entries times the factor at each energy bin which is lower than the current energy bin. The model gives a good representation of the data down to approximately 8 keV.

This model is a representation for the entire diode. Comparing it to figure 5.11, the plateau is over-estimated for the electron-gun spot, which is centered on the diode, without rim effects.

5.5.3. Simulation results

The expected diode efficiency to detect electrons at different energy bins and the corresponding mean deposited energy is shown in figure 5.13. These figures are based on the response matrices of pitch angles up to 30°. The total energy response of the highest energy bin is shown in figure 5.14. The detection efficiency drops for larger pitch angles as the virtual dead-layer depth, the electron has to overcome, increases while also the probability of backscattering increases. A detailed discussion can be found in reference [Ren11].

In this simulation the detection limit in the simulation is set to an energy threshold of 3 keV. Therefore, the detection efficiency starts to increase at an initial electron energy of 5 keV shown in figure (a) and rises to more than 80 % at the highest energy bin. The remaining electrons are backscattered, lose all of their energy in the dead-layer, or deposit less than 3 keV in the sensitive volume. In both sub-figures the simulation for the different dead-layer thicknesses of (300 nm, 325 nm and 350 nm) is shown.

As a 325 nm dead-layer thickness is set as the nominal value, the others can be interpreted as the error band. The maximum difference is 4.7 % in the detection efficiency, which leads to a rate uncertainty of the same factor. Figure 5.13 (b) shows the mean deposited energy over its initial energy for the different dead-layer thicknesses. It can be seen that even the highest energy electrons lose 2.5 keV on average in the dead-layer. The uncertainty is determined

by the various dead-layers and the maximum difference in the average deposited energy is 153 eV.

From these simulation results one can see that the largest uncertainties in this entire chapter originate from the uncertainties of the diode dead-layer thickness. These can cause uncertainties up to 4.7 % in the detection efficiency for single bins and an energy shift of more than 3 bins with a bin width of 50 eV. In the error estimation of the combined response the uncertainty for each bin is treated separately. A more detailed discussion about the diodes used in the FBM can be found in [Ell19].

5.6. Simulation of the data acquisition system

After electrons deposit their energy in the sensitive volume of the diode, the measured charge has to be read-out. This is done by Amptek DP5/PX5 devices. The signal undergoes pulse shaping and the resolution depends on various factors as, for instance, shaping time, noise, pile-up, and the DC offset. Optimized settings are used for each diode and use case.

The signal, especially for high rates, detected by the data acquisition can be simulated with a Monte-Carlo ansatz. The simulation code is available in the KASPER framework. Another tool is discussed in [Bab10].

All these tools depend on the expected count rate. During First Tritium measurements, the amount of tritium atoms was low (approximately 0.5 % tritium purity) and pile-up effects were negligible. Hence, in this work, a simple ansatz of a convolution with a Gaussian distribution of 2.5 keV FWHM is sufficient. This value is derived from the the electron-gun data during STSIIIa measurements of the 18.6 keV peak, see figure 5.11. The result of a convolution with the response at the largest energy bin is given in figure 5.14. In order to perform the full convolution, the energy range of the simulation is extended to 22.5 keV leading to a total number of 390 bins as the convolution also shifts events to higher energy bins.

Since the detection probability below 5 keV is low (compare figure 5.13) no extension towards lower energies is required. Therefore, the response matrices for the energy deposition and the simulation of the data acquisition is combined into one set of response matrices. Nevertheless, for future measurements, the simulation has to be performed with the expected rate and data acquisition settings to understand the measured signal.

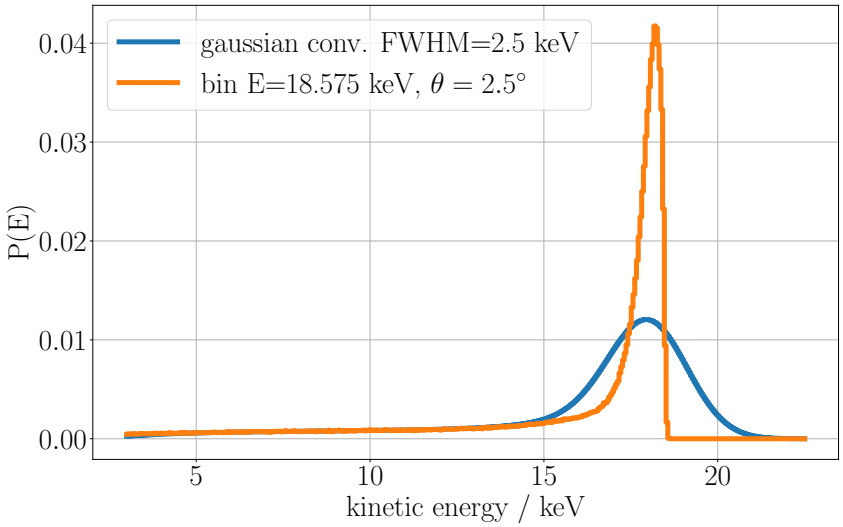

Figure 5.14.: *The combined detector response. In orange, the effect of the dead-layer on the initial energy bin with E=18 575 eV at a polar angle of θ=2.5° is shown and the probability of depositing energy in each of the 50 eV bins. The blue curve shows the convolution of the dead-layer effects in orange with a normalized Gaussian distribution of FWHM=2.5 keV (its area is normalized to one).*

CHAPTER 6
COMBINATION OF RESPONSE-MATRICES

To simulate the tritium signal, which is expected to be measured by the FBM detector during the First Tritium and nominal KATRIN operation, all required components of the KATRIN experiment are investigated in the previous chapter 5. The response matrices of the individual components need to be combined. Each component comes with a response matrix for each entry of the initial distribution matrix. This leads to a four dimensional array, which is radially dependent for some of the components in the experiment. This chapter explains how the different components are combined and the influence on the expected signal of each component is given.

To calculate the FBM response, the experiment is split into four separate stages. An overview is given in section 6.1 while detailed investigations are given in sections 6.2 to 6.4. This is followed by the uncertainty estimation of the simulation model in section 6.5. An outlook on the influence on the neutrino mass fit, also deep into the tritium spectrum, is given in section 6.6.

6.1. The four stages of the simulation

The final simulation model used for this thesis consists of four stages, set up in a modular way, and each component in the KATRIN experiment contributes to its specific stage. These are:

1. **Initial stage:** The initial stage simulates the laterally distributed tritium gas, the beta decay and the scattering process. As an input it requires the initial electron energy and angular distribution. Therefore, the tritium endpoint energy as well as the neutrino mass can easily be exchanged in the model. The initial stage only needs to be applied once. The output of this stage is the electron probability distribution at the rear- and front-end of the Source. An example output distribution can be found in the previous section, in figure 5.2.

2. **Rear-Section stage:** The input of the Rear-Section is the rear-end output of the initial stage and this stage outputs the magnetically reflected electrons as well as electrons that are backscattered from the Rear-Wall or valve V0. This stage comprises the electron transport to the rear-end from the Source, the reflection off the rear-end of KATRIN and the transport back to the Source. In order to combine the different responses to one stage, four particle distributions are required. One is the initial input distribution, the second distribution is required in front of the Rear-Wall/V0, which consists of particles about to hit the rear-end. The third consists of the particles reflected off of the rear-end and the fourth consists of electrons transported back to the entrance of the Source.

This is necessary because electrons that are reflected off, for example the Rear-Wall, have pitch angles larger than the acceptance angle and are therefore magnetically reflected during their travel back to the Source and hit the Rear-Wall again. The scattering process continues until a fixed fraction of particle probabilities are left in the distributions of reflected electrons and those about to hit the rear-end again. Usually, the fraction is fixed to 1 ‰ of the summed input distribution.

3. **Transport through Source stage:** This stage consists of three distributions, the first is the input distribution, in other words electrons that return from the Rear-Section to the Source, or electrons that return from the Transport-Section to the Source. The second and third are the back-reflected distribution in the Source and the output distribution opposite side of the Source for transmitted electrons. The Source in the model is assumed to be symmetric and therefore the same model is applied for electrons entering the Source from both sides.

4. **Transport-Section and *p-i-n*-diode stage:** This stage is comparable to the Rear-Section stage. It comprises of the input distribution, which consists of electrons leaving the Source in forward direction, a second distribution of electrons about to hit the diode, the third distribution consists of electrons reflected off of the diode and the fourth of electrons re-entering the Source. The reflection and handling of the distributions work exactly as for the Rear-Section and the same fraction of 1 ‰ is utilized for the distributions. The additional, fifth, distribution is one-dimensional and represents the simulated electron probability spectrum. This is the final spectrum that needs to be weighted by the tritium purity in the Source, measured by the LARA experiment [Sch+11], and the column density at the local magnetic field in order to calculate the rate for each energy bin.

These stages are combined into one response using the same method described for the Rear-Section and Transport-Section stage. The calculation of the final FBM detector signal runs until all output distributions of the different stages (except the signal) only consist of 1 ‰ of the summed initial distribution. The fraction can easily be varied. Additionally, the radial dependency is implemented to all the stages, i.e. different acceptance angles and inclination angles on, for example the Rear-Wall. This leads to a complete, modular model.

6.2. Rear-Section stage

In nominal KATRIN operation, for electrons well below the energy of the tritium beta decay endpoint, the scattering of electrons off the Rear-Wall plays an important role in describing the tritium electron spectrum measured by the FBM and for keV-sterile neutrino searches. The probability of electrons to scatter off the gold plated Rear-Wall is not negligible during KATRIN operation. The influence of the rear-end of the experiment is described for nominal KATRIN configuration, as well as for First Tritium configuration in this section.

6.2.1. Zero radial offset

The probability distributions of electrons, according to their kinetic energy and polar angle, is shown in figure 6.1 for a starting radial position of $r_S = 0\,\text{mm}$ at the rear-exit of the Source. As the Source is assumed to be symmetric, figure (a) is identical to the probability distribution shown in figure 5.2 (c), but flipped along its y-axis (pitch angle axis). A pitch angle of 180° is anti-parallel to the magnetic field line and perpendicular at 90°. Electrons, leaving the Source in rear direction follow their magnetic field line and are partially reflected if they are in the polar angle bin 95° to 90°. The other electrons hit the Rear-Wall, or valve V0, and are distributed

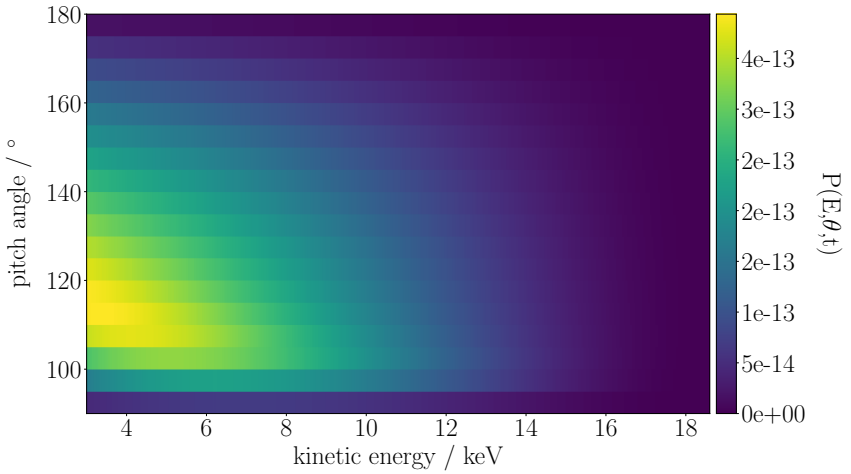

(a) The initial distribution at the rear-exit of the Source.

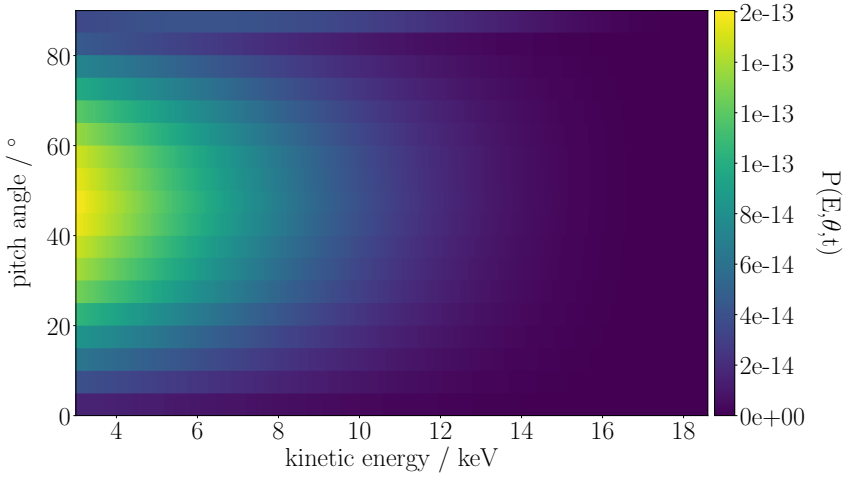

(b) The incoming electron distribution into the rear-end of the Source reflected in Rear-Section.

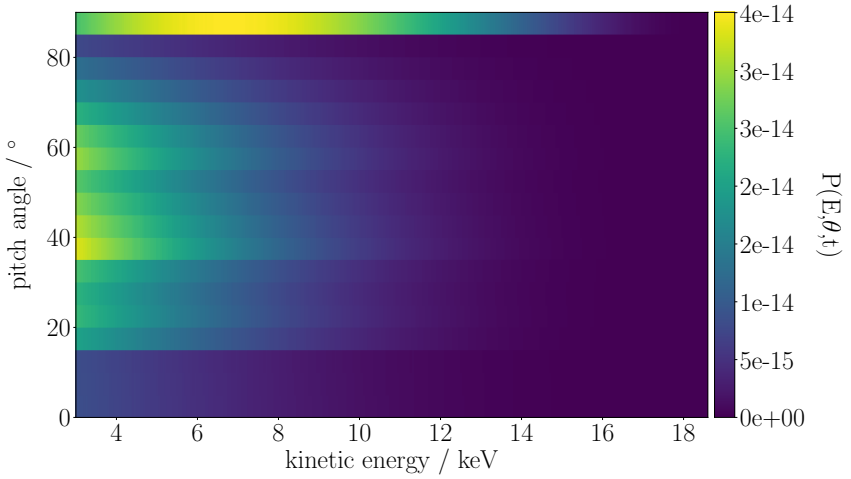

(c) The incoming electron distribution reflected in Rear-Section during First Tritium campaign.

Figure 6.1.: *The electron probability distribution in polar angle and energy after leaving the Source on the rear-side (a) and the electron probability distribution reflected in the Rear-Section of KATRIN during nominal KATRIN operation (b) and during First Tritium operation (c).*

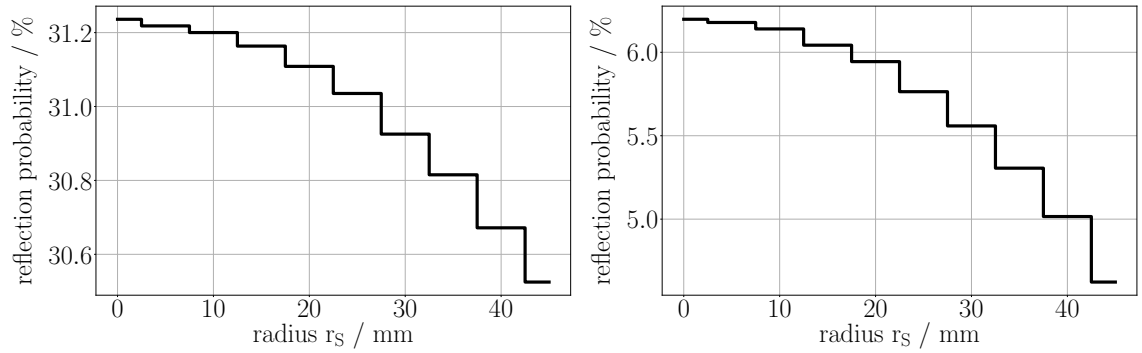

(a) Nominal KATRIN settings.

(b) First Tritium settings.

Figure 6.2.: *The radial dependence of the integrated electron reflection probability in the Rear-Section. The energy threshold for the integration is 3 keV.*

according to their pitch angle and inclination angle of the magnetic field line at the rear-end of the experiment.

The reflected electrons travel back to the Source or are magnetically reflected in the Rear-Section and hit the rear-end again until they are either transmitted, fall below the 3 keV threshold or return to the Source. The distribution of electrons returning to the Source is shown in figure 6.1 (b) for nominal KATRIN settings and in (c) for First Tritium settings.

The influence of the settings during First Tritium setup compared to the nominal settings can directly be seen. The z-axis of figure 6.1 (b) and (c), or the color-code respectively, is almost one order of magnitude smaller than during nominal settings. Hence, less electrons are reflected from the Rear-Section back into the Source. This is a result of the turned off Rear-Section magnet. The low magnetic field lowers the probability of electrons, scattered off valve V0, to re-enter the Source due to the very small acceptance angle. The largest contribution to the probability distribution in figure (c) have the pitch angle bins 85° to 90°. These electrons do not hit valve V0 but are magnetically reflected in the Rear-Section.

Other than that, the distribution at nominal settings in figure (b) is rather symmetric along the pitch angle axis with the largest probability for electrons at energies between 3 keV to 5 keV and pitch angles in the range from 20° to 70°. The initial probability distribution, with electrons leaving the Source in rear-direction, is also dominated by the same energy range, but the pitch angle probability is shifted to lower angles, i.e. a smaller transversal momentum component.

The initially assumed isotropic distribution of the pitch angle does not hold for electrons re-entering the Source and their pitch angle distribution needs to be described by binning them. Additionally, for large magnetic field changes, a finer pitch angle binning can be utilized to achieve a smoother transition in between pitch angle bins. This effect can be seen in figure (c) and is caused by the re-binning from the small magnetic field at valve V0 and the magnetic field in the Source. The reflection probability also depends on the the initial starting conditions of the electrons in the Source. The radial dependency is investigated in the next section.

6.2.2. Radial dependency

The acceptance angle from electrons leaving the Source towards the Rear-Section is radially independent. Nonetheless, as shown in section 5.2, the magnetic field and also the inclination

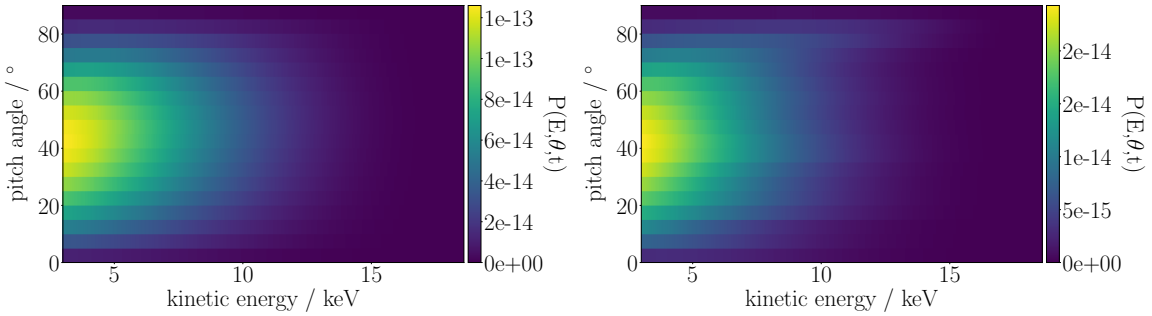

(a) Nominal KATRIN settings.

(b) First Tritium settings.

Figure 6.3.: *The distributions of electrons that are reflected in the Rear-Section and have traveled through the Source and are finally transmitted to the front-exit - at nominal KATRIN settings (a) and First Tritium settings (b).*

angle of the magnetic field line onto the Rear-Wall, or valve V0, is radially dependent. Hence, the magnetic field at the rear-end directly affects the reflection probability.

The integrated radial reflection probability is shown in figure 6.2. As described in the previous section, the probability of electrons returning to the Source is approximately five times larger at nominal KATRIN settings (a) than for First Tritium settings (b). Both reflection probabilities drop towards larger starting radii r_S in the Source. This is mainly caused by the decreasing magnetic field at the Rear-Wall or valve V0 for an increasing radius. The relative change at nominal KATRIN settings at the outermost radius at $r_S = 45\,\text{mm}$ compared to 0 mm is 2 % while it is 25 % at the First Tritium settings. Nevertheless, the total change during First Tritium is only on the order of 1.5 %.

6.3. Source transport stage

Electrons, that are reflected in the Rear-Section, need to pass the Source in forward direction to reach the FBM detector. They can scatter off the tritium molecules changing the pitch angle of the electrons, they can fall below the energy threshold of 3 keV or even get reflected back to the rear-exit of the Source. Besides the assumption of a symmetric Source response along the z-axis, the Source response is also assumed to be radially independent.

The utilized input probability distributions for this stage are shown in figure 6.1 (b) and (c). In nominal KATRIN operation 82 % of the electrons reach the front exit of the Source and 4.6 % are reflected back towards the rear-end of the Source. The remaining electrons are below the energy threshold due to interactions with the gas inside the Source.

In First Tritium configuration, only 74.5 % of electrons reach the front-exit of the Source and 11.8 % are reflected. The discrepancy between the two configurations arises mainly from pitch angle 85° to 90°. In the First Tritium input distribution 18 % of events are distributed in the bin with largest probability of being reflected while only 4.1 % of electrons are distributed in that bin during nominal operation.

The distributions at the front-exit of the Source are shown in figure 6.3. The contour of both distributions is comparable. The largest probability for electrons is to be distributed in the energy bins from 3 keV to 7.5 keV and pitch angle bins 20° to 60°. However, even electrons with an energy of 16.5 keV leave the Source in forward direction, but the probability is suppressed by one order of magnitude. The probability for electrons close to the tritium endpoint to leave the Source is suppressed by three orders of magnitude.

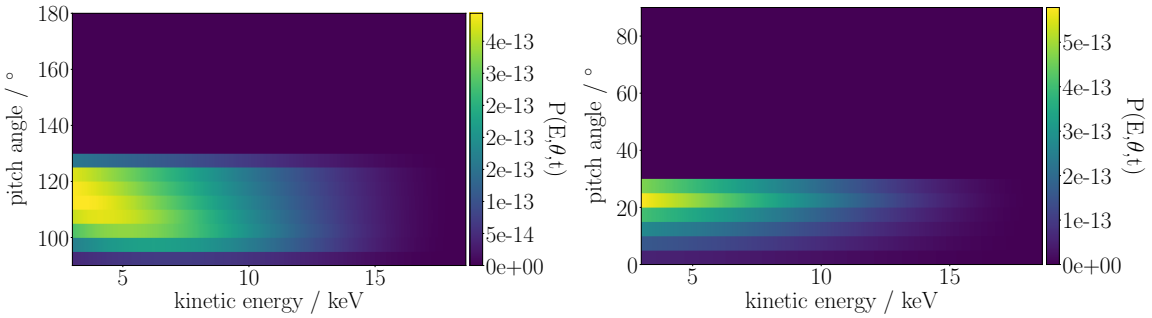

(a) Distribution at Source.

(b) Distribution at FBM.

Figure 6.4.: *The distributions of electrons that are magnetically reflected in the Transport-Section (a) or transmitted to the FBM (b).*

Although the transport through this stage is radially independent, the input distribution differ slightly due to the inclination angle of the magnetic field lines on the Rear-Wall/valve V0. Therefore, each response for the probability distributions at different Source radii r_{S}, emanating from the Rear-Section, is calculated individually.

6.4. Transport-Section stage

In this stage electrons are transmitted or reflected on their way from the front-exit of the Source to the FBM. The output of this stage is the final energy distribution at the detector as well as the back-reflected electrons into the Source. According to the previous stages, two electron distributions leave the Source in forward direction to the FBM. One originates from the initial tritium beta decay, the other from electrons reflected in the Rear-Section. These are generally combined at the Source exit in the simulation framework.

Nonetheless in this section, they are treated independently to investigate their individual contribution to the FBM signal. This stage is identical for the First Tritium and nominal KATRIN settings.

6.4.1. Electrons from initial decay

The electron spectrum, directly originating from tritium beta decay, is shown in figure 5.2 in the previous chapter. These electrons travel along their magnetic field line towards the FBM (compare figure A.IV in the appendix) or are magnetically reflected if they have a pitch angle larger than the acceptance angle of $\theta_{\mathrm{accept}} \approx 52.7°$. The acceptance angle is radially dependent. Following the magnetic field line in the center of the Source, i.e. $r_S = 0\,\mathrm{mm}$, about 43 % of electrons reach the FBM while 57 % are magnetically reflected back into the Source from the initial electron energy and polar angle distribution. The final distributions are shown in figure 6.4. The pitch angle of the electrons is shifted by 180° (absolute value) in figure (a), but distributed identically compared to the initial distribution (figure 5.2 (c)) down to the acceptance angle. This distribution represents the magnetically reflected electrons. The electron distribution at the FBM is compressed in the angular distribution from 0° to 30°, because the magnetic field drops down to $B_{\mathrm{final}} \approx 0.8\,\mathrm{T}$ at the FBM from $B_{\mathrm{S}} \approx 2.5\,\mathrm{T}$.

The radial transmission probability is shown in figure 6.5. As no electrons can be trapped or fall below the energy threshold in the Transport-Section, all electrons, that are not transmit-

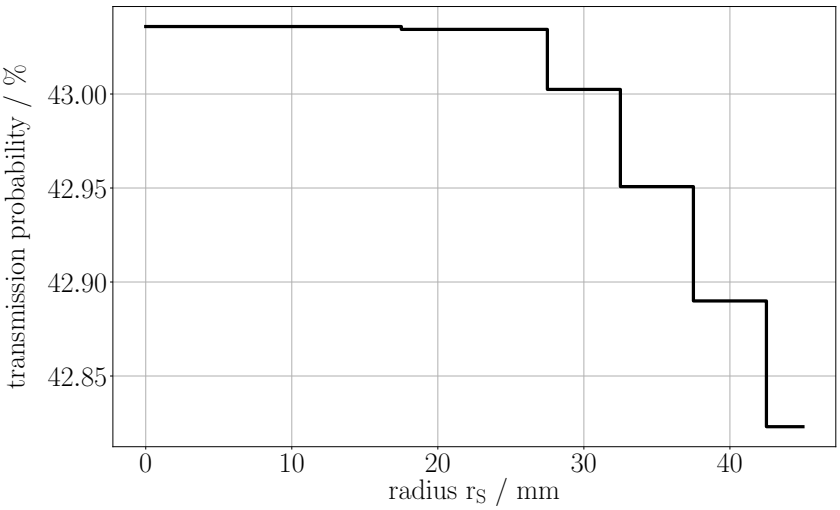

Figure 6.5.: *The integrated probability for electrons to be transmitted to the FBM detector at different radii r_S.*

ted, are reflected back to the Source. The transmission/reflection is almost radially independent as it only depends on the acceptance angles that are radially almost identical. The difference in transmission probability drops from the center of the Source towards the outer wall of the Source by approximately 0.2 %.

Electrons are not only magnetically reflected in the Transport-Section, but also have a non-negligible probability to get reflected off the diodes of the FBM detector. Those reflected electrons also need to surpass the magnetic field barrier in order to reach the Source again. As shown in section 5.3, the reflected electrons need to have a pitch angle in the range of 180° to 153.36° due to the low magnetic field at the FBM position. The remaining electrons hit the detector again and are not reflected back to the Source. This additional effect leads to a combined probability of 58.5 % from the initial distribution leaving the Source to be reflected back to the Source. This fraction also includes secondary electrons, originating from the primary electrons interacting with silicon atoms in the detector diode, which reach the Source with an energy threshold of 3 keV. The contribution of reflected electrons from the diode is therefore 1.5 %.

The reflected electrons travel through the Source and 75.9 % are transmitted to the rear-exit of the Source while 7.6 % are reflected back to the entrance of the Source. The remaining electrons are below the energy threshold. During the First Tritium configuration 5.9 % of electrons return from the Rear-Section back to the Source and 4.6 % of these electrons reflected in the RS reach the front-exit of the Source again. Therefore, in total, of the 58.5 % reflected electrons in the Transport-Section, 13.2 % are reflected in the Source or Rear-Section and enter the Transport-Section again.

During nominal KATRIN configuration the percentage of electrons re-entering the Transport-Section is more than two times higher of 30.4 %. Therefore, in order to calculate the FBM rate and spectral shape, it is necessary to include even higher-order stages. For instance, electrons that are reflected twice in the Transport-Section still have a chance to be detected by the FBM detector.

6.4.2. Electrons reflected in Rear-Section

As shown in the previous section, electrons that are reflected in the Transport-Section and travel back to the Source have to be considered in order to estimate the rate and spectral shape of the beta spectrum at the FBM detector. Those detected electrons are either reflected in the Source itself or in the Rear-Section.

After the electrons are reflected in the Source or Rear-Section and leave the Source in forward direction again, the polar angle distribution is not uniform in $\cos(\theta_{\text{pitch}})$. The probability distributions are shown in figure 6.6. Additionally, the probability distributions of electrons, that initially stem from beta decay of tritium and leave the Source at its rear-end where they are reflected back into the Source are shown in the same figure.

Unlike in the previous section, the configurations during nominal KATRIN configuration and First Tritium are separated as electrons entering the Rear-Section have different reflection probabilities. Figures (a) to (d) represent the nominal KATRIN configuration and (e) to (h) the configuration during First Tritium. In figure 6.6, the first two distributions of each configuration stem from the initial beta decay electrons that are reflected in the Rear-Section and the latter probability distributions from electrons initially reflected in the Transport-Section.

As the angular distribution of electrons leaving the Source differs compared to section 6.4.1, their summed probability of transmission differs as well. At nominal KATRIN configuration, 35.3 % of electrons, leaving the Source initially at the rear-end, reach the FBM plane from the front-exit of the Source. In total, 9 % of all electrons leaving the Source towards the Rear-Wall reach the FBM in first order. For the configuration during the First Tritium campaign the probability is 37.2 % and 1.7 % respectively.

Electrons, leaving the Source in forward direction that are reflected back into the Source again, still have a probability of 22.6 % to reach the FBM detector in nominal KATRIN configuration. The probability for electrons to reach the FBM plane during First Tritium configuration is 11.5 %. These electrons still need to pass the dead-layer of the detector in order to be detected.

6.4.3. Response of the p-i-n-diode

All the response matrices of the components of KATRIN constitute the final FBM detector signal. In the measured spectrum, all information about the initial pitch angle of the electron is lost and only the deposited energy of the electron is measured and stored into an energy histogram. In this section, the shape of the spectrum, the individual contributions to the shape of the spectrum and also the radial dependence in First Tritium configuration as well as in nominal KATRIN configuration is investigated.

6.4.3.1. Spectral shape

The shapes for the beta-spectrum of tritium, as simulated for the FBM, are shown in figure 6.7 for a centered diode in the experiment at $r_{\text{S}} = 0\,\text{mm}$. In figure (a) and (c), the simple and full model for the different setup configurations are shown.

The simple model consists of the undistorted tritium beta decay spectrum, i.e. without scattering effects in the Source. This probability distribution is forwarded, according to the response of the Transport-Section, towards the FBM detector and results in the spectrum shown in figure 6.7 after applying the simulated response of the diode. This simple model works well from the endpoint to approximately 15 keV by eye, but the relative difference at that energy is 19.5 % in count rate between the two models. The total difference in rate between the two models at a threshold of 5 keV is 62.2 %. Therefore, the complete model is required to simulate the expected

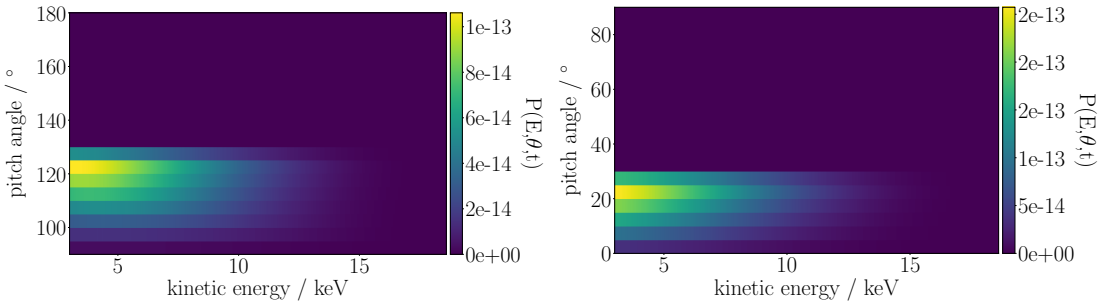

(a) NK: Source dist. from RW reflection.

(b) NK: FBM dist. from RW reflection.

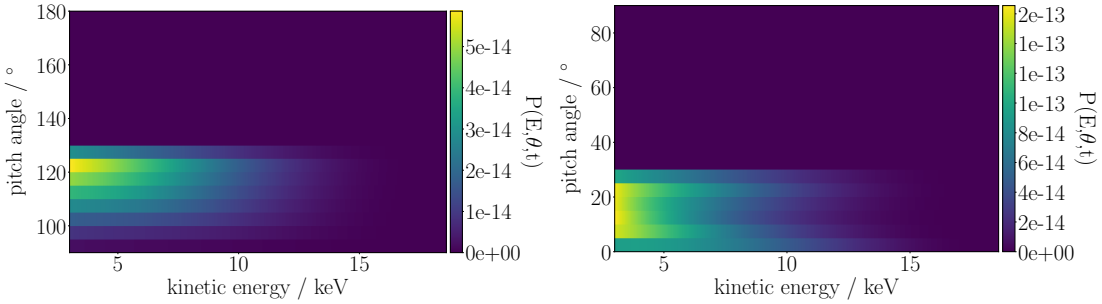

(c) NK: Source dist. from TS reflection.

(d) NK: FBM dist. from TS reflection.

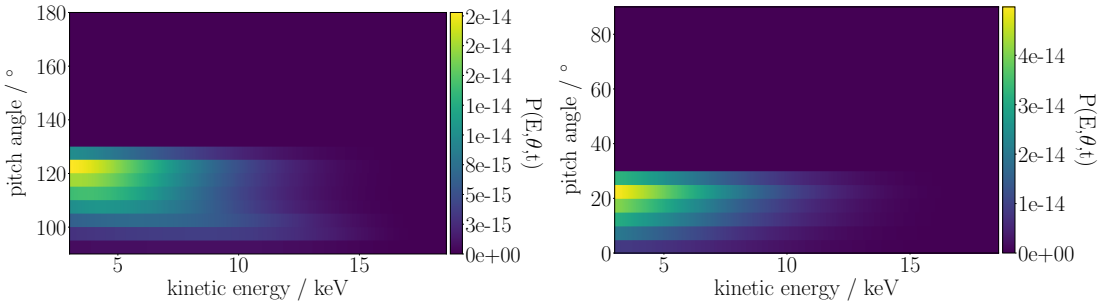

(e) FT: Source dist. from V0 reflection.

(f) FT: FBM dist. from V0 reflection.

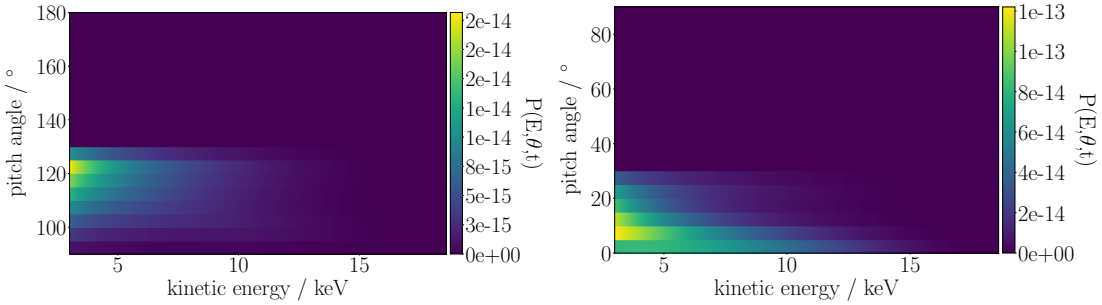

(g) FT: Source dist. from TS reflection.

(h) FT: FBM dist from TS reflection.

Figure 6.6.: *The acronyms NK and FT stand for nominal KATRIN configuration and the configuration during First Tritium campaign, TS for the Transport-Section and RW for Rear-Wall. The figures on the left side always represent the distributions at the front-entrance of the Source after reflection in the Transport-Section, and on the right side the distributions after transmission. The first row, figures (a) and (b), show the distributions of electrons from beta decay leaving the Source on the rear-side and being reflected in the Rear-Section. Figures (c) and (d) are distributions from electrons reflected in Transport-Section that get reflected again in the Source or Rear-Section and enter the Transport-Section again. Figures (e) through (h) are identical representations to the first four figures but in First Tritium configuration.*

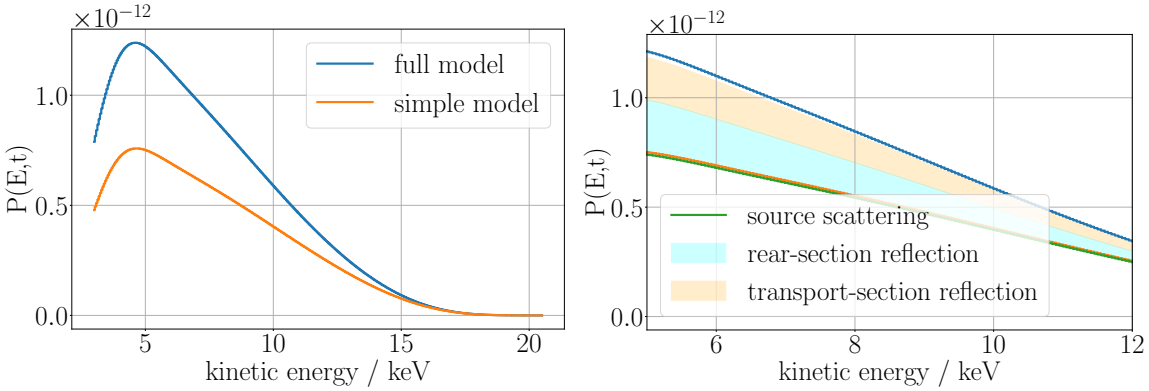

(a) NK: spectral shape full and simple model.

(b) NK: spectral shape contributions.

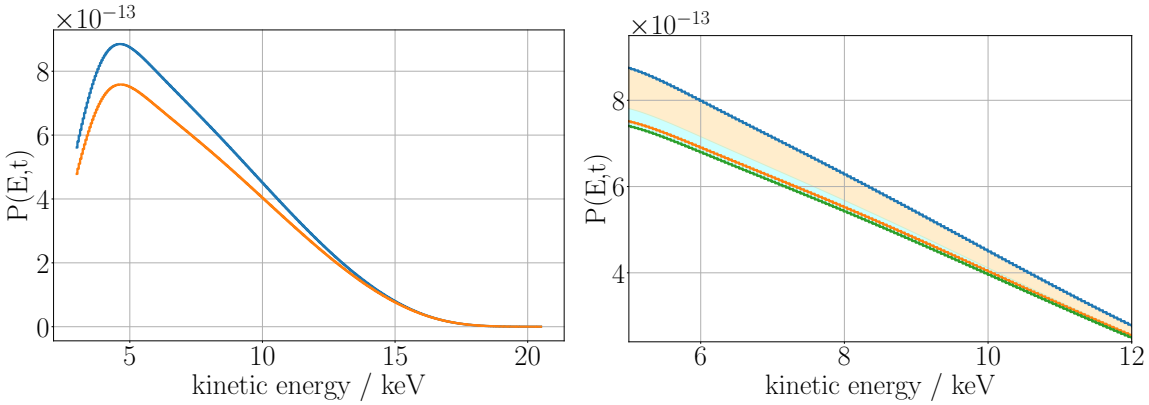

(c) FT: spectral shape full and simple model.

(d) FT: spectral shape contributions.

Figure 6.7.: *The expected energy distributions measured with the FBM detector in First Tritium and nominal KATRIN configuration. In figure (a), the distributions in nominal configuration for a simple model and the full response matrix model are shown. In figure (b), the same distributions zoomed into the energy range of 5 keV to 12 keV, with additional information on the contributions leading to the full model, are shown. Figure (c) is the equivalent to figure (a) and (d) to (b) in First Tritium configuration.*

	Nominal KATRIN	First Tritium
Simple model	66.7 %	88.6 %
Source scattering	65.5 %	87.1 %
Rear-Section reflection	17.9 %	3.7 %
Transport-Section reflection	14.3 %	9.2 %
Higher order processes	2.3 %	1 ‰

Table 6.1.: *Overview of the different constituents to the full model with an energy threshold of 5 keV and the comparison the simple model. The contributions from Source scattering, reflection in Rear-Section and Transport-Section, as well as higher order effects are normalized to 100 % and compared to the rate of the simple model. The simple model is given to demonstrate the effect of electrons scattering in the Source and its effect on the detected count rate.*

rate and spectral shape.

The different contributions leading to the full model distribution, in nominal KATRIN configuration, are shown in figure (b). In addition, compared to figure (a), the effect of the Source response, i.e. electrons scattering off the gas molecules in the Source, is indicated with the label *source scattering*. This distribution has a 1.5 % lower integrated probability than the simple model, at 5 keV threshold, to be detected with the FBM detector. Nevertheless, it is the basis for the additional contributions leading to the full model. The largest contribution, besides the electron distribution leaving the Source in forward-direction, are electrons leaving the Source at its rear-end that are reflected from the rear-end and finally reach the FBM detector. They contribute 17.9 % to the total rate with a 5 keV energy threshold in nominal KATRIN configuration.

Electrons, leaving the Source in forward direction that are reflected back into the Source still contribute 14.3 % to the total rate at the same energy threshold. These three constituents, electrons directly being detected at the FBM after leaving the Source, electrons reflected at the rear-end, and electrons reflected in the Transport-Section, together almost add up to the full model. However, a 2.3 % contribution to the rate in the full model originate from processes of higher order, for example electrons that are reflected in the Rear-Section and return into the Source, but scatter off the gas molecules and enter the Rear-Section again, but are still detected by the FBM detector.

The expected electron energy distributions of the FBM detector during the First Tritium campaign, with valve V0 closed, can be seen in figure 6.7 (c) and (d). Figure (c) is the equivalent to figure (a), and (d) to (b). Even without the influence of the total amount of tritium atoms (i.e. $\epsilon_{\mathrm{T}},\ \rho d$), the expected rate is larger in the nominal configuration due to the reflection probability in the Rear-Section. At a threshold of 5 keV, the rate in nominal configuration is 32.9 % higher than in the First Tritium configuration.

The graphs of the simple model are identical in all figures as the model is independent of the Rear-Section. Still, it only represents 88.6 % of the rate in the full model. The different contributions can be seen in figure (d). It can be seen that 3.7 % of the electron rate stems from electrons reflected in the Rear-Section from the initial beta decay and 9.2 % from electrons reflected in the Transport-Section. Due to the low reflection probability, the amount of the individual contributions has changed in ordering compared to nominal KATRIN configuration in figure (c). The contribution of higher order effects is in the 1 ‰ regime. All the individual contributions to the full model are additionally listed in table 6.1.

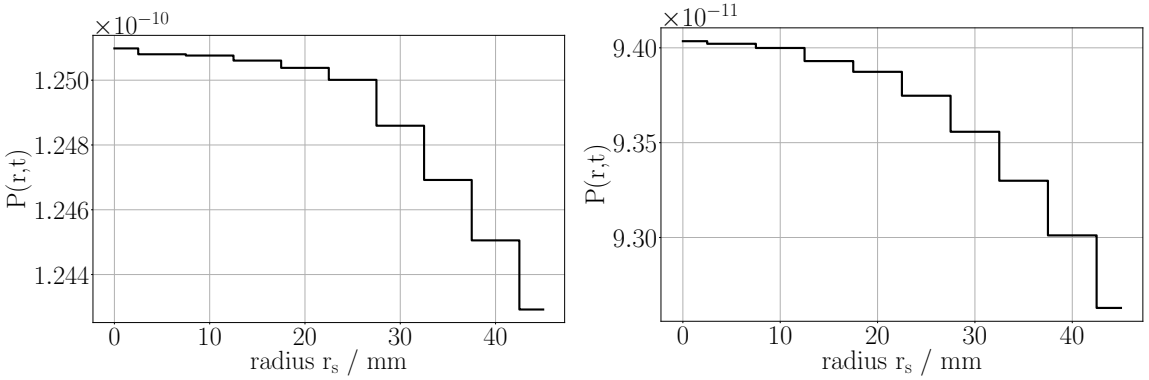

(a) NK: radial dependence of integrated probability. **(b)** FT: radial dependence of integrated probability.

Figure 6.8.: *The radial dependence of the integrated probability of a single tritium atom to decay and reach the FBM detector with a 5 keV energy threshold. On the left figure (a), the radial dependence at nominal KATRIN settings, and on the right figure (b), the dependence at First Tritium settings is shown.*

6.4.3.2. Radial dependency

The largest influence, resulting in a radial rate gradient at the position of the FBM detector, is the radially dependent magnetic field. The smaller the magnetic field is, the less tritium atoms are within the magnetic flux tube of the *p-i-n*-diodes - or in other words - the effective volume inside the Source shrinks proportionally to the field at the FBM detector. This is shown in figure 5.8. Nonetheless, independent of the amount of tritium atoms in the Source, by only considering a single atom to decay per second and for the emanated beta electron to reach the FBM and get detected, the radial dependent integral probability is shown in figure 6.8 with an energy threshold of 5 keV. One can see that even though the probability of a single tritium atom to decay per second is independent of the radius - the detection probability is dependent on it. Three effects lead to the different detection probabilities:

1. The acceptance angle in Transport-Section and Rear-Section.

2. The magnetic field strength at the FBM and Rear-Wall/valve V0 changes the pitch angle and therefore the scattering probability.

3. The inclination angle of the magnetic field line onto the Rear-Wall/valve V0 changes the reflection probability.

At nominal KATRIN settings, the relative difference in the integrated probability at $r_S = 0$ mm to 45 mm is 6 ‰ and 1.5 % for First Tritium settings. This radial effect adds an additional gradient onto the radial dependence of the magnetic flux tube on the magnetic field in the FBM plane, discussed in section 5.3.2.

6.5. Combined uncertainty estimation

The systematic uncertainties discussed in chapter 5 for the different components in the KATRIN setup assume a Gaussian distribution of the uncertainty around its mean. These effects contribute to the error of the spectra shown in figure 6.7. Not only do they contribute to the uncertainty of the kinetic energy axis, but also to the probability of an electron to be within

that bin with the corresponding energy distribution uncertainty. In this combined error estimation, the probability $P(E,t)$, which represents the probability of a single tritium atom of being detected in the 50 eV bin per second, is treated independently of the error caused by the energy uncertainty for the same bin. Both contributions are discussed in this section.

6.5.1. Combined uncertainty on detection probability

The total probability $P(E,t)$ of a single electron to be detected in a specific bin is the product of all the contributions, i.e. electrons directly transmitted in the Front-Section/Transport-Section (TS), electrons being reflected in the Transport-Section (refl. TS), in the Rear-Section (RS) and higher order processes (HO). Therefore the rate probability given in figure 6.7 is calculated as:

$$P(E,t) = \sum_{i=\mathrm{TS,RS,...}} p(E,t)_i = p(E,t)_{\mathrm{TS}} + p(E,t)_{\mathrm{RS}} + p(E,t)_{\mathrm{refl.\ TS}} + p(E,t)_{\mathrm{HO}} \tag{6.1}$$

The integral of the different contributions are listed in table 6.1 for a 5 keV threshold. But this equation is utilized for each energy bin separately. To calculate the uncertainty on the probability for each bin, Gaussian error propagation is utilized, which leads to a combined absolute variance of:

$$\sigma^2_{P(E,t)} = \sigma^2_{\mathrm{p(E,t)_{TS}}} + \sigma^2_{\mathrm{p(E,t)_{RS}}} + \sigma^2_{\mathrm{p(E,t)_{refl.\ TS}}} \tag{6.2}$$

Since higher order processes are not significant, especially during the First Tritium campaign, these are not considered in the uncertainty calculation.

The calculation of the variances σ^2 for the different contributions per bin is not straight-forward. The uncertainties of the different components of the experiment are given as relative deviations onto the probability distribution. Additionally, the uncertainties need to be weighted according to their contributions towards the total detection probability.

That means, the absolute uncertainty for each contribution $p(E,t)_i$ is calculated independently and summed according to equation 6.2. An example is the contribution of directly transmitted electrons. The uncertainty for the final probability distribution at the FBM detector depends on the relative uncertainty in the source, which is 1.5 % for each bin (compare section 5.1.2) and the uncertainty of the *p-i-n*-diode, which is given in section 5.5. The uncertainty of the *p-i-n*-diode each bin is treated separately according to figure 5.13.

The uncertainties of the other components are also given as the relative standard deviation σ_{rel} on the detection probability. The relative uncertainty in the Source is 1.5 % and 0.5 % for electrons scattering off the rear-end of KATRIN. All uncertainties are treated only in first order, for example the uncertainty on the detection probability of electrons leaving the Source towards the rear-side is a convolution of the uncertainties of the Source, the Rear-Wall/valve V0, a second time the uncertainty of passing the Source and the diode response uncertainty.

Two different methods can be used to calculate the uncertainty. The first describes the maximum uncertainty by calculating the output probability distribution for each contribution $p(E,t)_i$ and to apply the relative uncertainties onto it to retrieve the absolute uncertainties. This is called the *basic* uncertainty and its relative value to $P(E,t)$ is given in figure 6.9 (b). The second approach is to calculate the uncertainty for each component and to propagate the uncertainties until the final distribution. This approach is called the *extended* uncertainty, shown in the same figure. The main contribution on the uncertainty comes from the response of the diode. The graph denoting *no detector* describes the uncertainty of the extended model with the detector response.

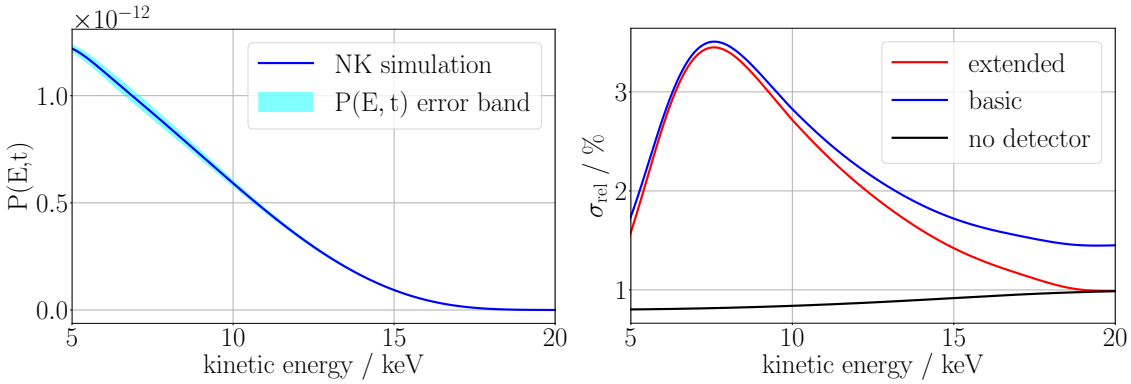

(a) NK: error band. **(b)** Relative uncertainty.

Figure 6.9.: *In the left figure (a), the simulated tritium spectrum in nominal KATRIN configuration with the probability P(E,t) and its error-band is shown. In the right figure (b), the relative uncertainty per energy bin is shown for the different methods. The basic method results into the error-band given in figure (a).*

The combined error for the nominal KATRIN configuration is shown in figure 6.9 (a). As the uncertainty from scattering off the Rear-Wall or V0 is identical, but the contributions from reflections in the Rear-Section or Transport-Section are smaller, the uncertainty is also an upper estimate for the First Tritium configuration. In the following the basic model for the uncertainty is used.

6.5.2. Combined uncertainty on kinetic energy

The combined uncertainty on the energy needs to be treated different to the uncertainty on the detection probability. Due to the used methods, the electrons are always binned in 50 eV intervals and therefore the uncertainty for each energy bin needs to be calculated. The contribution of each stage and path the electron is taking before it is detected, differs and thereby the path defines the energy uncertainty. Electrons, directly leaving the Source in front direction, which are transmitted to the FBM and get detected, have a smaller energy uncertainty than electrons scattering off the Rear-Wall before they get detected at the FBM. The method on how-to estimate the uncertainty is shown in figure 6.10. The variance of the contributions from equation 6.1 differs for each. Therefore, the energy uncertainty distribution $f(E)_{\mathrm{TS,RS,refl.\ TS}}$ differs for each contribution as well.

As an example and illustration, the standard deviation σ is assumed to be 2 eV for directly transmitted electrons, 3 eV for electrons from the Rear-Section and 4 eV for electrons reflected in the Transport-Section. The integral of the initial normal distributions $f'(E)_i$ with i representing the different contributions, is - by definition - normalized to one. The respective normal distributions $f(E)_i$ given in figure 6.10 are normalized to their contributions w_i listed in table 6.1 for the nominal KATRIN configuration.

$$\int_{-\infty}^{\infty} f'(E)_i \cdot dE \stackrel{!}{=} 1 \qquad \text{for}: \quad i = \mathrm{TS, RS, refl.\ TS} \tag{6.3}$$

$$\Rightarrow \; w_i \cdot \int_{-\infty}^{\infty} f'(E)_i \cdot dE = w_i \tag{6.4}$$

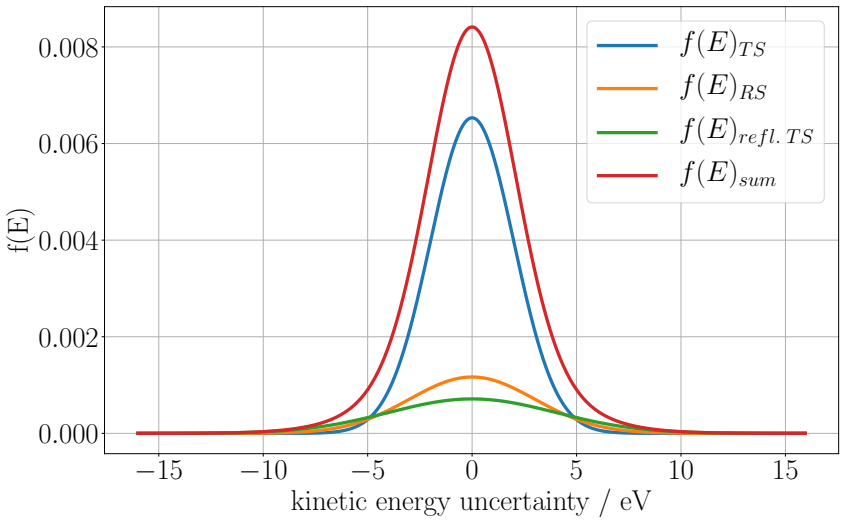

Figure 6.10.: *The method used to calculate the variance of the energy. The x-axis displays the energy uncertainty and the center at 0 eV is equivalent to the bin center and the y-axis gives the probability for each bin. All the contributions are normalized to their respective detection probability. The sum of all contributions results in the total energy uncertainty f(E).*

with:

$$f(E)_i \stackrel{!}{=} w_i \cdot f'(E)_i \qquad \text{for}: \quad i = \text{TS}, \text{RS}, \text{refl. TS} \tag{6.5}$$

$$f(E)_{\text{sum}} = \sum_i f(E)_i \tag{6.6}$$

Therefore the sum in figure 6.10 leads to the distribution $f(E)_{\text{sum}}$, which is not a normal distribution. Its integral is set to one, which is equivalent of an electron being detected and needs to have an energy uncertainty given by the distribution $f(E)_{\text{sum}}$. The variance for this distribution can be calculated via:

$$\sigma^2_{\text{sum}} = \int_{-\infty}^{\infty} (E-\mu)^2 \cdot f(E)_{\text{sum}} \cdot dE \tag{6.7}$$

with μ being the mean value, which is the center of the bin. For each bin this is calculated numerically according to the independent weights which are calculated the following:

$$w_i = \frac{p_i(E,t)}{\sum_i p_i(E,t)} = \frac{p_i(E,t)}{P(E,t)} \qquad \text{for}: \quad i = \text{TS}, \text{RS}, \text{refl. TS} \tag{6.8}$$

with:

$$\sum_i w_i = 1 \tag{6.9}$$

This results in a standard deviation σ of 2.58 eV in the given example. Nevertheless, the calculation can also be done analytically:

$$\sigma^2_{sum} = \sum_i w_i \cdot \sigma_i^2 \qquad \text{for}: \quad i = \text{TS}, \text{RS}, \text{refl. TS} \tag{6.10}$$

This can be derived from equation 6.7 as in the case of a binned energy spectrum each bin gets the same weight w_i, which is derived from equation 6.4. The weighting is independent of the

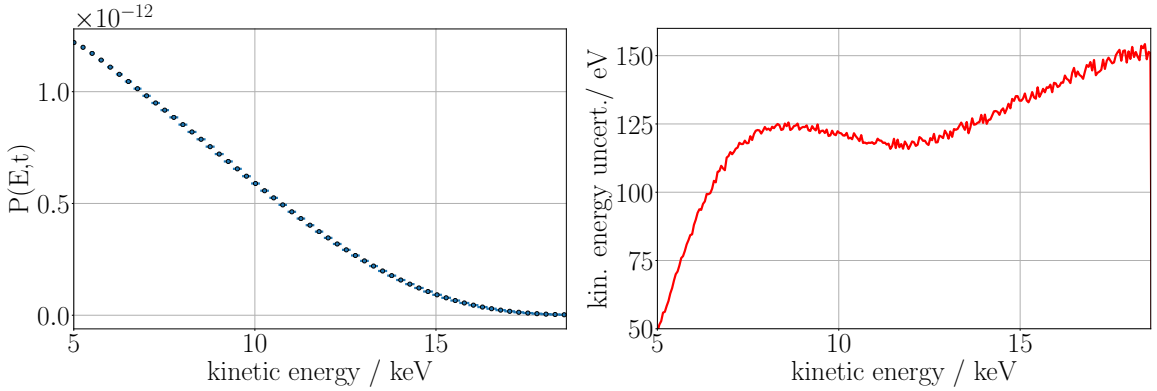

(a) NK: error on kinetic energy.

(b) NK: absolute uncertainty on energy.

Figure 6.11.: *In the left figure (a) the simulated tritium spectrum in nominal KATRIN configuration P(E,t) and its uncertainty σ on the kinetic energy is shown. Due to constraints in the visualization and the small error-bars, only every fifth simulation data point is shown. In the right figure (b) the absolute uncertainty per energy bin is given which are the hallmarks of the left figure.*

energy and can be pulled out of the integral resulting in the final equation 6.10.

The result for the energy uncertainty calculation, in nominal KATRIN operation, can be seen in figure 6.11. Although the weighting differs for nominal KATRIN settings and the settings during the First Tritium campaign, the uncertainty is dominated by the diode response. Therefore, only the nominal KATRIN kinetic energy uncertainty is shown. The energy uncertainty from the Source is set to be 16.5 eV for each bin, and 2 ‰ relative uncertainty for each bin due to Rear-Wall scattering. Uncertainties, or energy losses induced due to synchrotron radiation are not considered. Because of its large effect, the average energy loss due to the diode response uncertainty is applied bin-wise. As stated in the previous section, only first order processes are considered in the error calculation.

The result is shown in figure 6.11 (a). In the figure only every fifth data point is shown as the simulated data points may have an uncertainty up to the width of four bins. The absolute uncertainty is visualized in figure (b). In the appendix, in figure A.I, the uncertainties on the detection probability and energy are visualized.

6.6. Investigating the endpoint region

The complete model, described in this chapter, can also be used to investigate effects of scattering in the Rear-Section onto the detected integrated spectrum at the Focal Plane Detector. Therefore, it needs to be extended to incorporate the MAC-E-filter, the post-acceleration and the FPD detector response.

However, these additional components are not considered in this work. The different contributions can also be investigated at the position of the FBM by removing the FBM detector response. As figure 6.7 suggests by eye, the simple model and full model agree well down to an energy of approximately 15 keV, below that energy both models begin to deviate.

In this section only the nominal KATRIN configuration is investigated as the contribution of secondary effects is larger due to its magnetic field configuration in the Rear-Section. The expected spectrum down to 2 keV below the endpoint is shown in figure 6.12.

It can be seen that 2 keV below the endpoint, the reflection in the Rear-Section and Transport-

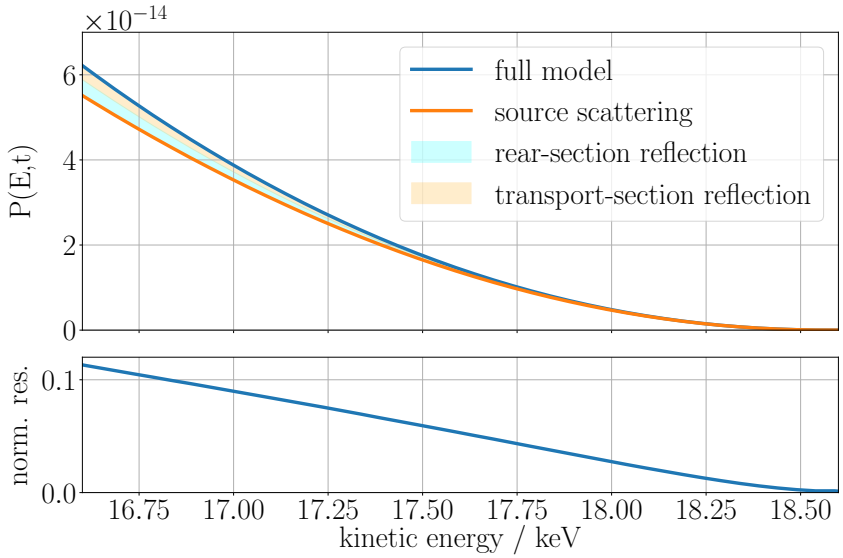

Figure 6.12.: *The expected beta decay spectrum at the position of the FBM 2 keV below the endpoint. At the bottom the normalized residuals of the full model and the model only incorporating Source scattering is shown.*

Section still contribute about 10 % to the expected signal. As expected, the contribution of Rear-Section reflection is larger than the Transport-Section reflection. At 0.2 keV below the endpoint the contribution is still at half a percent off the total probability $P(E, t)$.

The contribution of electrons that scattered off the Rear-Wall or in the Transport-Section get the more apparent the deeper a scan for the neutrino mass is. Therefore, these effects must be taken into account, for example they can be modelled with an energy dependent background or the settings in the Rear-Sections need to be changed for deep scans by lowering the magnetic field or by replacing the Rear-Wall with a material absorbing the electrons.

6.6.1. Effect of Source scattering

Modelling the scattering of the electrons in the Source at the tritium endpoint is important in order to fit the neutrino mass. Therefore, electrons leaving the Source in forward direction towards the FBM are compared with and without scattering in the Source. The FBM detector response is not incorporated in this comparison. The result down to 2 keV below the endpoint is shown in figure 6.13.

It can be seen that the absolute difference increases between the models with and without scattering the lower the kinetic energy of the electron is. However, the normalized residuals (simple model subtracted from full model normalized to full model) increase towards larger kinetic energies. Therefore, it is crucial to model the scattering processes close to the endpoint in order to fit the neutrino mass.

At 2 keV below the endpoint, the difference is 4 % while close to the endpoint it is in the order of 41 %. The kink in the spectrum of the residuals at the endpoint is enforced due to the normalization to prevent a division by zero.

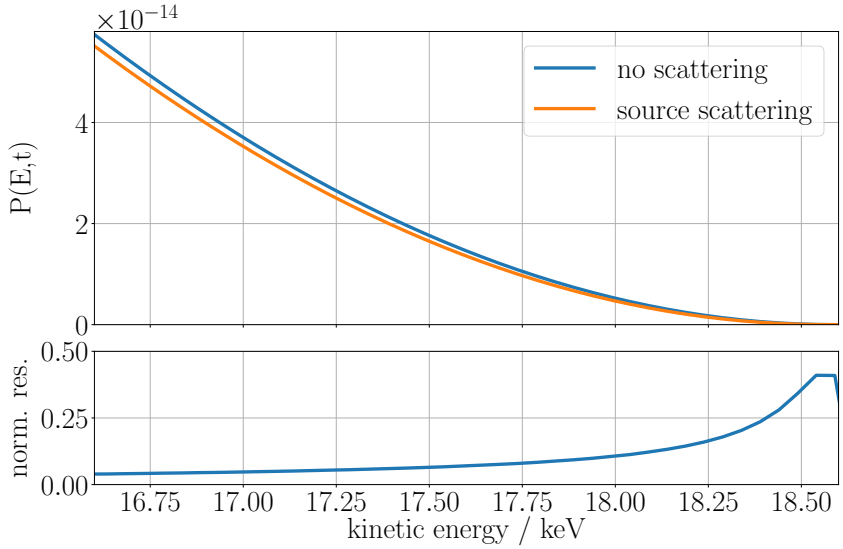

Figure 6.13.: *Visualization of the expected beta decay spectrum at the position of the FBM 2 keV below the endpoint with and without scattering in the Source. At the bottom the normalized residuals of the scattering and no-scattering model is shown.*

CHAPTER 7
FIRST TRITIUM

On 18th of May 2018 tritium was injected for the first time into the Source of the KATRIN experiment. At this time, the FBM detector board was replaced by a Faraday cup to measure the ion- and electron-flux in the CPS before they enter the Pre-Spectrometer.

Initially, the valve in between the CPS and Pre-Spectrometer was closed to perform ion retention tests [Kle18] in the KATRIN setup. After these tests were successful, the valve was opened and additional ion-retention tests were performed with the Pre-Spectrometer (method described in reference [KG17]). First scans of the tritium beta spectrum were performed and the results were presented at the Neutrino 2018 conference [Par18].

After this initial phase, the Faraday cup was replaced by the FBM detector board and a new measurement phase of KATRIN with tritium started at approximately 1 % purity of DT in the Source. This phase is called "First Tritium". The first tritium beta spectrum was measured on the 5th June 2018 with the FBM detector. This measurement phase was followed by the official inauguration of KATRIN on 11th June 2018. This chapter refers to data measured with the FBM during the "First Tritium" campaign.

Section 7.1 discusses the expected and measured rate as well as corrections applied to the systematics of the setup. This is followed by section 7.2, which compares the measured tritium spectra with the simulated spectra presented in the previous chapter.

The FBM also performed scans in the flux tube. The observed magnetic field and measured electron rate is discussed in section 7.3 and 7.4. Additionally, as the FBM is in scanning mode, the FPD (Focal Plane Detector) is recording the imprint of the electron shadow caused by the FBM. This can be used to estimate the relative position between the FPD and FBM. This is discussed in section 7.5.

7.1. Estimating FBM rate

The main purpose of the FBM is to measure the electron rate in the CPS in order to monitor changes of the column density and tritium purity. Since the FBM cannot disentangle fluctuations of these two quantities, the latter needs to be monitored by the LARA setup and the column density is calculated from the Source properties. During the First Tritium campaign only DT with a purity of approximately 1 % was inserted into the Source which is equivalent to a total tritium purity of $\epsilon_{\mathrm{T}} = 0.5\,\%$.

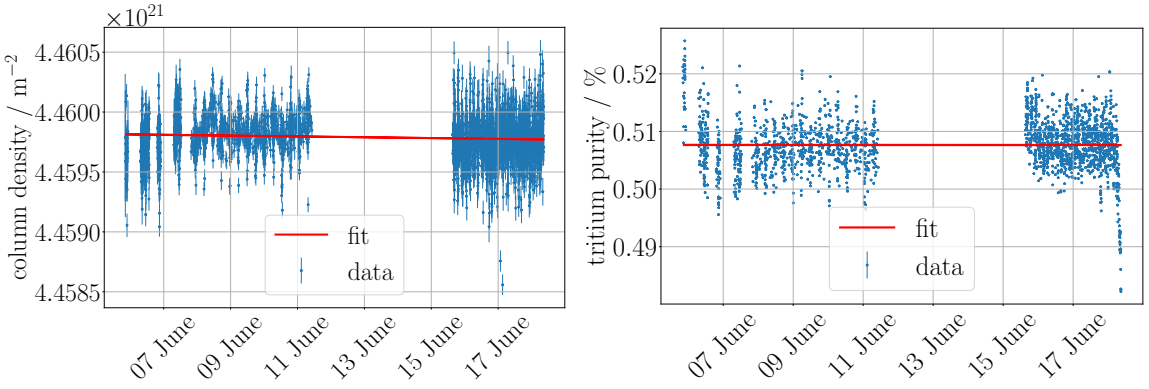

(a) Column density. **(b)** Tritium purity.

Figure 7.1.: *The stability of the column density during the First Tritium campaign (a), and the tritium purity (b).*

7.1.1. Stability of column density and purity

While the tritium purity is an output of the LARA setup, the column density has either to be calculated from the inlet pressure into the WGTS or the throughput. However, the stability can quickly be calculated using the FBM detector. The interested reader can be find more information on the calculation of the column density in [Hei18; Kuc+18a] and [Kuc+18b]. Currently, there are two ways of accessing the tritium purity data, first the raw output stored to the database of KATRIN, or the re-analyzed tritium purity data utilized for neutrino mass analyses. This work utilizes the re-analyzed data given in the run-summaries of the FPD runs. The column density and tritium purity data are shown in figure 7.1.

Both parameters show drifts during the First Tritium campaign. A linear fit results in a slope of the column density of $-3.44 \cdot 10^{15}\,\mathrm{m^{-2}\,d^{-1}}$ with an average column density of $4.46 \cdot 10^{21}\,\mathrm{m^{-2}}$. The tritium purity has a slope of $-6.06\,\%\,\mathrm{d^{-1}}$ with an average purity of 0.51 %. Even though the slopes of both quantities are small, fluctuations on smaller timescales (hours) can be seen in the data.

7.1.2. Calculation of the expected FBM rate

From each timestamp, shown in figure 7.1 on the x-axis, the measured rate of the FBM can be estimated. The measured rate of the FBM detector is also given in the run-summaries of KATRIN, a threshold at channel 180 was chosen which is equivalent to an energy threshold of 5.3 keV and far away from the noise peak in the spectrum. This threshold is also used for the rate estimation. The estimation of the detection probability of a single electron from tritium decay per second is shown in figure 6.8 in the previous chapter. However, an energy threshold of 5 keV is used in this calculation. As can be seen from this figure, the integrated probability is also radially dependent.

During the First Tritium campaign channel 2 of the FBM was situated at the position of approximately $x = 67\,\mathrm{mm}$ and $y = 3\,\mathrm{mm}$. This results in an integrated probability of $P(t) = 8.82 \cdot 10^{-11}\,\mathrm{s^{-1}}$ for a tritium atom to decay per second and to be detected with the FBM detector with an energy larger than 5.3 keV.

In order to calculate the rate, the number of tritium atoms in the magnetic flux tube to the FBM, needs to be known. An example calculation is given in section 5.3.2. To calculate the

effective diode size equivalent in the Source A_{S}, equation 5.7 is used:

$$A_{\mathrm{S}} = \frac{0.82\,\mathrm{T}}{2.52\,\mathrm{T}} \cdot 1.35\,\mathrm{mm}^2 = 0.44\,\mathrm{mm}^2 \tag{7.1}$$

Hence, the magnetic flux at the FBM with a diode size of $1.35\,\mathrm{mm}^2$ in a magnetic field of approximately $0.82\,\mathrm{T}$ spans an area equivalent to $0.44\,\mathrm{mm}^2$ in the Source.
To calculate the number of tritium atoms $\mathcal{N}$ in the Source per effective area A_S, the average Source column density ρd and tritium purity ϵ_{T} has to be utilized.

$$\begin{aligned}\mathcal{N} &= A_{\mathrm{S}} \cdot 2\rho d \cdot \epsilon_{\mathrm{T}} \\ &= 4.4 \cdot 10^{-7}\,\mathrm{m}^2 \cdot 2 \cdot 4.46 \cdot 10^{21}\,\mathrm{m}^{-2} \cdot 0.0051 \\ &= 199\,716 \cdot 10^8 \text{ atoms}\end{aligned} \tag{7.2}$$

The rate can therefore be calculated as:

$$R(t) = P(t) \cdot \mathcal{N} = 1761.50\,\mathrm{s}^{-1}. \tag{7.3}$$

This can be done separately for each timestamp with the column density and tritium purity for the same timestamp. The simulated result is compared to the measured rate in figure 7.2.

The measured FBM rate with channel 2 agrees within a 5 % uncertainty with the simulated rate. By eye, the trend of both look similar, but the spread of the measured data points is larger due to the spread of the tritium purity. This is shown in figure 7.1. In the following discussion of the rate trend, the First Tritium measurement campaign is split into three phases shown in figure 7.2 (a). The phase before 7th June is called first phase, and the second/third before/after 15th June 2018. In the first phase, the slope of the rate can be explained by a comparable trend within the tritium purity data during that time. The measured data fits the expected rate rather well with a small offset in the second phase. During the first phase, the FBM additionally cooled down which is not considered so far in this calculation. A detailed look at the influence of the temperature is taken in section 7.1.3.

While the difference of the simulated and measured rate in the second phase is positive, it is inverted in the third phase. Systematics in the FBM setup must have changed to cause this behavior. However, the difference in both phases at each data point can be considered constant. A zoom into phase II and III is shown in figure 7.2 (b) and (c). The slope of the measured rate in phase II is $0.33\,\%\,\mathrm{d}^{-1}$ and $-0.16\,\%\,\mathrm{d}^{-1}$ in phase III. In both figures, a structure can be seen in the measured rate that is also apparent in the simulated rate. Therefore, this is an artifact of tritium purity or column density.

7.1.3. Influence of the temperature

During phase I, the FBM was situated at its monitoring position and started to cool down from room temperature. To investigate the influence of the temperature onto the measured rate, the data needs to be cleaned, i.e. effects of tritium purity fluctuations and column density fluctuations have to be removed. This is done utilizing equation 7.2. Each measured data point per timestamp is divided by the measured tritium purity and column density in the same interval. Afterwards, the averaged column density and tritium purity is multiplied again. This method implies that the tritium purity measured with the LARA setup is identical to that in the Source at the same timestamp. There could be an offset in time leading to a systematic offset. The temperature as well as the cleaned FBM data is shown in figure 7.3. As a downside of this approach, the fluctuation of the tritium purity leads to a larger fluctuation of the cleaned FBM

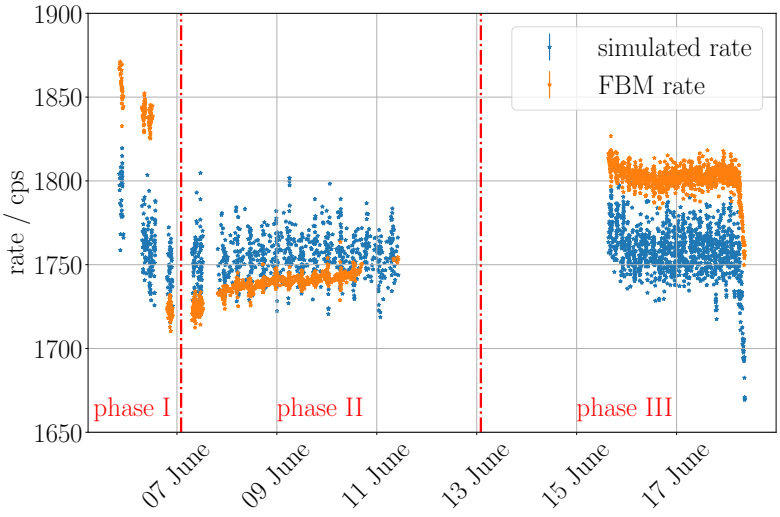

(a) FBM rate during First Tritium.

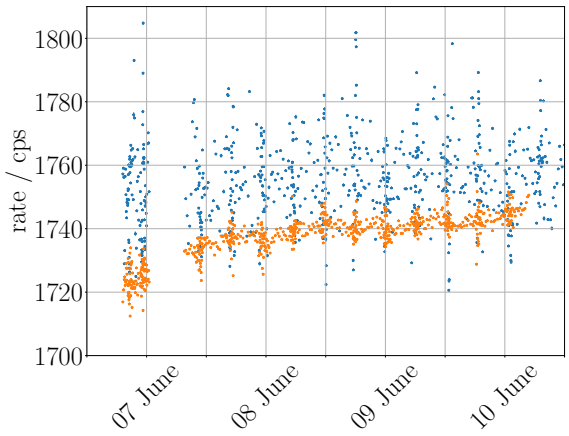

(b) Zoom on 7th to 11th of June (phase II).

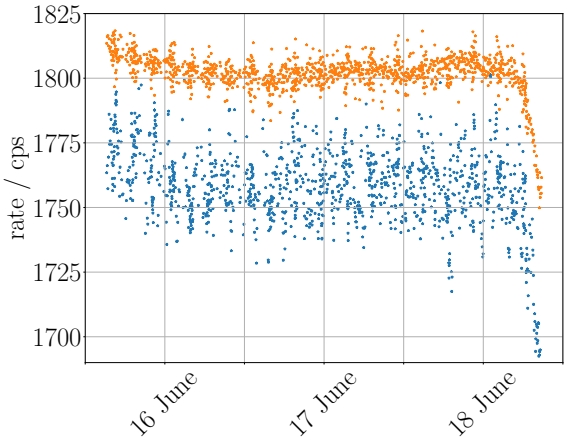

(c) Zoom on 15th to 18th of June (phase III).

Figure 7.2.: *Rate trend of the FBM during the First Tritium phase. Each data point represents the averaged rate during a sub-run of the FPD. The simulated rate is calculated using equation 7.3 for each tritium purity and column density data point. The two bottom figures are zoomed on the time axis to visualize the structure of the rate trend. Theses figures do not have error-bars for a better visibility of the trend.*

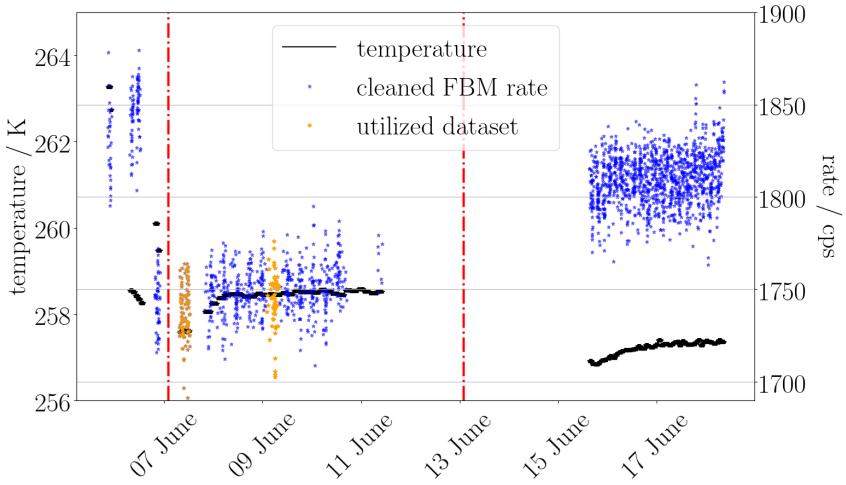

Figure 7.3.: *Temperature trend during the First Tritium campaign of the FBM and also the cleaned FBM rate trend during the campaign. Additionally, the utilized data to calculate the temperature effect on the rate is shown.*

data (compare figure 7.2). During phase I the FBM cooled down to approximately 258.5 K. The large cooling gradient could be responsible for the drop in rate if the rate and temperature are correlated. During phase II, the FBM heats up by approximately 1 K and also the rate increases slightly. During phase III, the offset increased between temperature and rate compared to the previous phases, which also hints towards a systematic change in the setup. The cleaned FBM data has a slope of $0.24\,\%\,\mathrm{d}^{-1}$ in phase II and $0.18\,\%\,\mathrm{d}^{-1}$ in phase III.

As phase II and I point towards a correlation of the temperature and measured rate, a correction factor can be calculated from phase II. The utilized dataset is marked in figure 7.3 and the average temperature and rate in that time slot can be calculated. This calculation leads to 8.02 additional counts per second at a base temperature of 258.5 K. In other words, if the temperature rises by 1 K compared to the base temperature, the rate increases by 8.02 cps and vice versa. The model can be motivated by a moving offset in the calibration due to temperature changes as described in reference [Ell19]. The Pearson correlation factor for temperature and measured FBM rate is 0.86 in phase II and therefore a correlation can be assumed even though reference [Ell19] suggests an anti-correlation. This linear model fails for large temperature differences as the rate of a tritium beta spectrum does not change linearly for large changes of the offset.

The result of the additional temperature correction on the data is shown in figure 7.4. Both phases still have an increasing rate over time with a slope of $(0.13 \pm 0.03)\,\%\,\mathrm{d}^{-1}$ in phase II and $(0.10 \pm 0.03)\,\%\,\mathrm{d}^{-1}$ in phase III. Both slopes are reduced by considering the effect of tritium purity, column density, and temperature. The large increase in rate in between phase II and III cannot be explained by the methods investigated in this work. Additionally, phase II still has an underlying structure, which could be an effect of the offset in time discussed earlier. The tritium concentration measured with LARA might not be identical to the current concentration in the Source. To utilize the stability of the FBM, especially on short-time, and to decrease large fluctuations of the tritium purity measurement, ideas were developed to utilize the FBM data to enhance stability of the tritium purity analysis during the First Tritium phase. More information about the rate trend can be found in [Ell19].

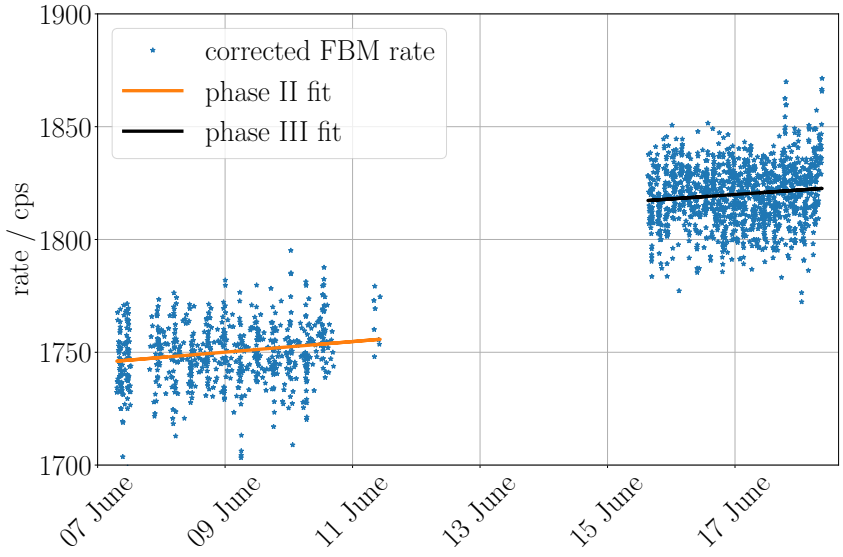

Figure 7.4.: *Fully corrected FBM data in phase II and III and its corresponding fit.*

7.1.4. Influence of the threshold

It is of interest if the rate trend with a slope of approximately $0.1\,\%\,\mathrm{d}^{-1}$ is identical for all energy thresholds. So far, the threshold of 5.3 keV was investigated. This threshold is the default setting for First Tritium data analysis. In order to investigate the slope, a time window with a constant temperature is chosen in order to only correct for tritium purity and column density fluctuations. The time window is from 8th June to 11th June and hence in phase II. The result can be seen in figure 7.5.

Although the slopes at different thresholds are compatible within their error bars at low energy thresholds, it appears that a minimum of the slope is to be found at approximately 7.5 keV. With increasing energy thresholds, the slope rises up to approximately $3\,\%\,\mathrm{d}^{-1}$ and starts to shrink at an energy larger than 16.5 keV. This hints towards a systematic change of the FBM detector and therefore the spectral shape. This is investigated in the next section. If it was a change in the tritium purity or column density the slope should be equal at all energy thresholds. The slightly changing scattering probabilities due to the changing column density can be neglected.

7.2. Measured tritium spectra

The main purpose of utilizing the response matrix approach is to be able to describe the measured tritium beta electron spectra in order to check for variations of the column density or tritium purity as well as other systematics. It can also be used for future sterile neutrino mass investigations with the FBM.

The previous section has shown that a drift of the FBM, even after all corrections are applied, is still apparent. In this section a look into the change of spectral shape is taken and its possible influence on the rate drift.

7.2.1. Comparison to the simulated spectrum

The comparison of the simulated and measured spectra is given in figure 7.6. The left hand picture (a) visualizes the different spectra and their respective error bars on the rate while the right hand picture (b) visualizes the residuals and normalized residuals. To calculate the rate of

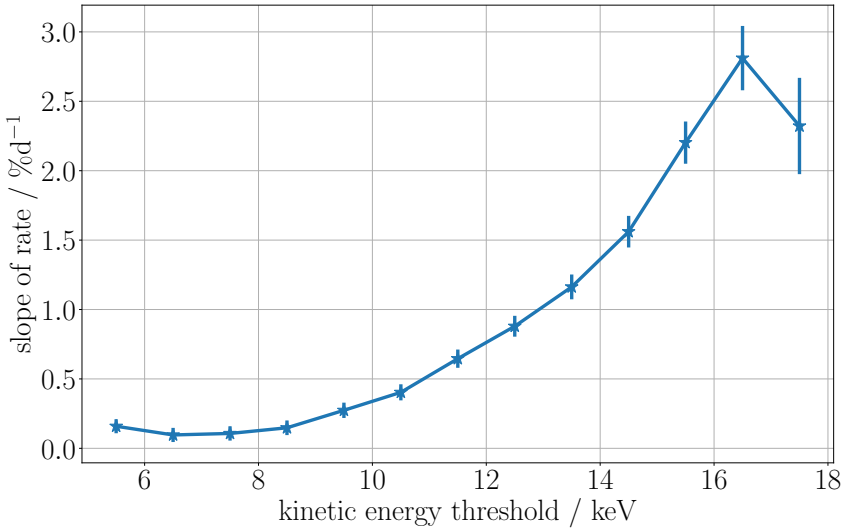

Figure 7.5.: *Rate in percent per day at different energy thresholds. Additionally, the error of the fit on the slope is shown.*

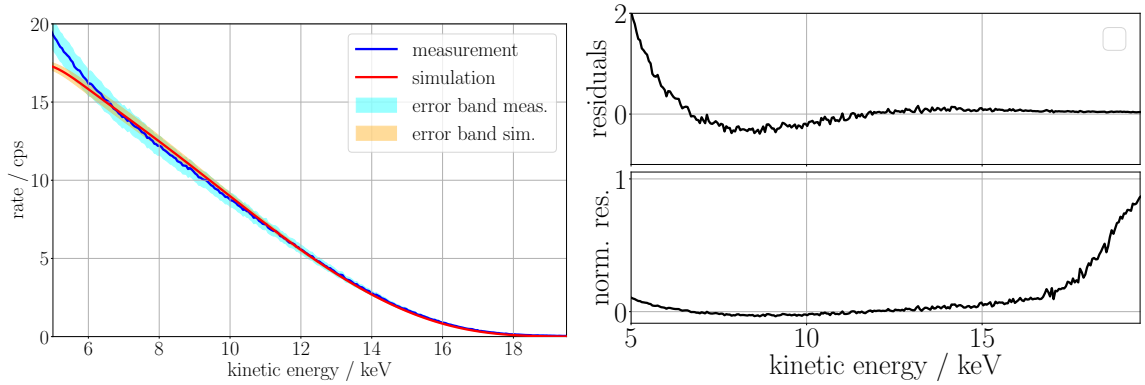

(a) Spectra. **(b)** Residuals.

Figure 7.6.: *The simulated spectrum including all necessary Source properties to calculate the rate for each bin in red and its error band in orange in figure (a). The measured data is shown in blue and its error band in cyan. In the right hand figure (b), the corresponding residuals of the measured and simulated spectrum on the top and the normalized residuals at the bottom are shown.*

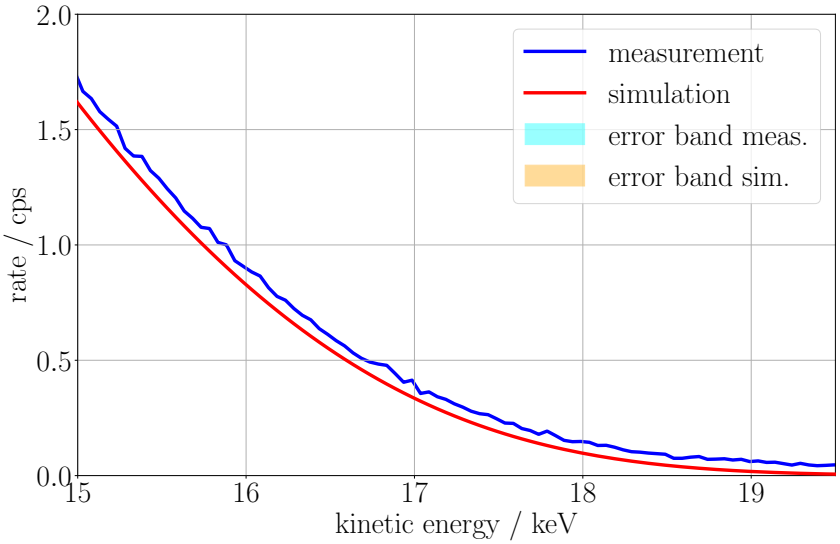

Figure 7.7.: *The endpoint region of figure 7.6 (a).*

each bin of the simulated spectrum the corresponding column density and tritium for that run are used. The calculation of the rate of each bin works analogous to the calculation presented in the previous section 7.1. The data is well described by the simulation above 10 keV (see figure 7.6 left), which can also be seen from the residuals. The increasing deviation close to the endpoint could arise from a drifted energy calibration, which means the spectrum shifts to lower energies due to changes of the hardware since the last energy calibration. Another effect, which is the probable cause of this difference, is pile-up in the detector which is not considered in the simulation by only utilizing a Gaussian convolution for the detector response. This effect should be investigated in future as it will become more prominent with full tritium purity in the Source.

Between 7 keV to 10 keV the simulation overestimates the measured data while it underestimates it below 7 keV. Without performing a simulation of the full detector response, the model does not have a noise peak in the low energy regime. A small amount of the noise peak can reach into the 5 keV to 7 keV energy regime. Another role below 10 keV comes from the numerical model for the diode introduced in section 5.5.2, which also underestimates measured data below 10 keV. However, the simulated spectrum agrees well with the data within its error bars between approximately 5 keV to 15 keV. The error on the data is dominated by the uncertainty of the column density, which is 5 % per bin [Hei18]. The estimation of uncertainty of the simulated data is presented in section 6.5.1. Uncertainties on the kinetic energy are not show in this figure. The reduced χ^2 between 5 keV to 19 keV is comparably large with $\chi^2/d.o.f = 26.0$ while it is 0.51 between 5 keV to 15 keV. Therefore, the error is overestimated in the low energy regime and underestimated in the high energy regime close to the endpoint. The high energy region is shown in figure 7.7. It shows that the simulated and measured spectral shape agree, but there is an offset not covered by the error bars, which results in a high reduced χ^2 test result. In this comparison, the uncertainty on the kinetic energy is not considered. For a full treatment of the endpoint region with the FBM detector, the detector response needs to be fully simulated including pile-up effects.

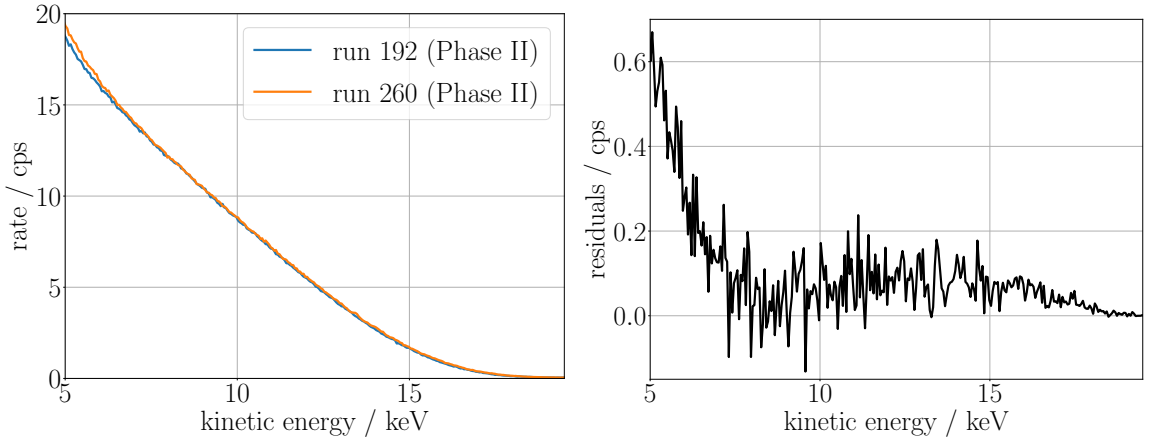

(a) Spectra. **(b)** Residuals.

Figure 7.8.: *The measured spectra at the beginning and at the end of phase II on the left (a). A change of the rate can be observed in the low energy regime. In the figure on the right (b), the residuals of both spectra, shown on the left, are shown.*

7.2.2. Change of the spectral shape

As it was found in [Ell19] the shape of the spectrum measured with the FBM changes over time. The change during phase II is shown in figure 7.8. In figure (a) it can be seen that the count rate in the low energy (below 7 keV) regime increased, while the residuals (b) also indicate a difference in the shape between 10 keV to 15 keV resulting in a plateau like structure. The change of the shape of the spectrum could explain the drift found in the previous section 7.1. In order to check and understand the shape of the spectra, the different FBM runs as shown in figure (a) need to be corrected by the tritium purity and column density. However, in order to observe and detect the residuals as seen in figure (b) an integration time of approximately 1 h is necessary, and during that time the tritium purity changes by up to 1 %, which does not allow for a correction. Therefore, it is challenging to simulate the effect of the residuals because it is superimposed by different effects which cannot be disentangled.

However, the noise peak of the spectra is moving towards larger energies while the amplitude becomes smaller and the FWHM increases. A detailed analysis of the noise peak can be found in [Ell19]. For this work, the noise peak was fit in order to extract the FWHM and to see if a decreasing energy resolution causes the change of the spectral shape. The width of the noise peak is assumed to be the energy resolution of the detector during the specific run. During run 192, the mean of the noise peak was situated at 0.56 keV with a FWHM of 1.95 keV and during run 260 at 0.67 keV with a FWHM of 2.14 keV. These energy resolutions are applied to the simulated tritium spectrum at the FBM before the data acquisition simulation as a convolution with the corresponding width of the Gaussian distribution. The result is shown in figure 7.9.

The simulated spectral change in the low energy range below 13 keV predicts negative residuals, which is in contradiction to the measured residuals (figure 7.8 on the right). As shown in figure 7.6, the simulation underestimates the count rate at low energies. And a broader energy resolution leads to even less counts in the spectrum in the energy range close to the simulation threshold < 7.5 keV.

However, by moving the energy threshold by 3σ of the energy resolution, with $\sigma \approx 1$ keV, towards higher energies to approximately 10.5 keV, the shape of the residuals should agree to the simulation if the assumption of a worsened energy resolution, which changes the shape of the

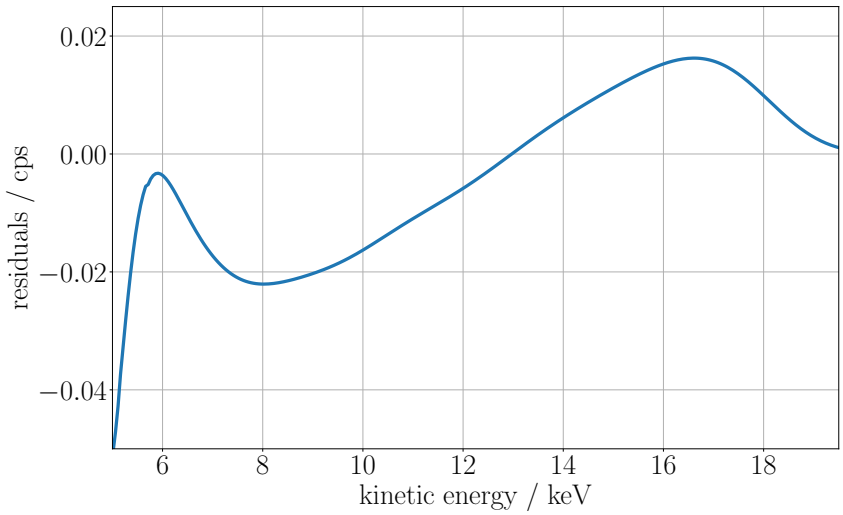

Figure 7.9.: *The residuals of the simulated FBM spectrum at two different energy resolutions. The spectrum with a resolution of 1.95 keV is subtracted from the spectrum convolved with a Gaussian of 2.14 keV FWHM.*

spectrum, is correct. This can be checked by looking at the expected slope of the rate change, due to the worsened energy resolution, of the simulation at different energy thresholds. Thereby, figure 7.10 (a) is identical to figure 7.5, but based on simulation.

The residuals of the measured and simulated slope at the same threshold can be read from figure (b). The residuals are increasing towards larger energies with a minimum at approximately 6 keV. The difference between measured and simulated slope is at its maximum at 15.5 keV with more than 1.06 % and drops to 0.53 % at 16.5 keV threshold.

Since the slopes of measured and simulated spectral change do not agree above 10 keV, the drift cannot be fully explained by the change in energy resolution. In future - for full tritium measurements - the FBM calibration should be checked with an electron-gun on a regular basis to exclude changes in gain or offset factor, which could also induce a drift in the rate.

7.3. Magnetic field

So far, the magnetic field at the position of the FBM is always assumed to be identical to the simulated field. The FBM board is equipped with a one-dimensional Hall-sensor that can measure the magnetic field in z-direction. During the First Tritium campaign radial scans with the FBM were performed, which as well as the rate at each position for each diode also maps the magnetic field at each position of the Hall-sensor. The measured magnetic field can therefore be compared to the simulated field. This work focuses on the scans performed during the First Tritium campaign, complete scans of the entire magnetic flux tube were performed before and after the campaign and are investigated in detail in [Ell19].

The diodes and the Hall-sensor are situated at different positions on the detector board, therefore the magnetic field always slightly differs between the diodes and the Hall-sensor. In order to get the actual magnetic field at the diodes, magnetic field simulation is used. As the simulated and measured magnetic field have a small deviation, the simulated field is corrected by the measured magnetic field. The result of a cross-scan of the magnetic flux tube can be seen in figure 7.11 (a). On the right, figure (b) the relative deviation from the simulation magnetic field

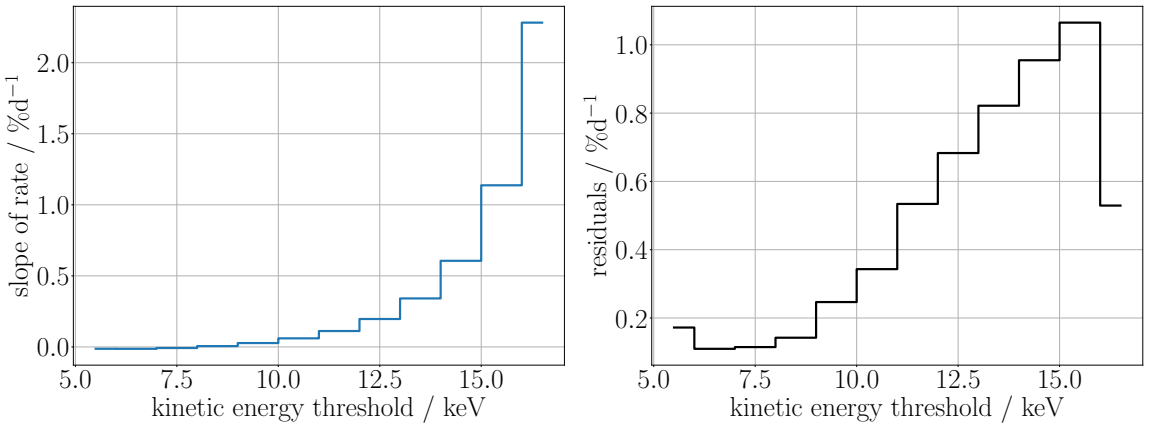

(a) Simulated slope threshold dependency.

(b) Residuals of measured and simulated slope.

Figure 7.10.: *The simulated slope of the rate for a drifting energy resolution at different thresholds on the left. On the right, the residuals of the left figure subtracted from the measured slope at different thresholds, as shown in figure 7.9, is shown.*

in z-direction to the measured magnetic field is stated. For figure (b), the simulated magnetic field positions are shifted by $y = -3.4\,\text{mm}$ and $x = 1.3\,\text{mm}$ to incorporate the correction factors found in [Ell19]. The deviation of the simulated magnetic field is 5 ‰ at maximum. This is in agreement with the uncertainties found for the Hall-sensor in [Sch17]. Although it is small, the deviation affects the detected count rate equivalently according to equation 5.7 and 7.2. In the next section 7.4 the radial rate dependency is investigated. Since the diodes have a positional offset to the Hall-sensor, the magnetic field at their position relies on simulation.

For the rate correction of a horizontal scan, i.e. a constant y-position, correction factors for the uncertainties of the measured to the simulated field are calculated. For positive x-coordinates, the relative deviation is shown in figure 7.12 including the error bars of the measured data. The relative deviation can be approximated by a linear fit at each x-position. The deviation is utilized in the next section for the calculation of the radial rate dependency.

7.4. Radial rate dependency

One could expect that the rate at the FBM is radially constant as neither the systematic parameters of the FBM nor the size of the diodes change, but the magnetic field determines the effective Source volume and therefore the number of tritium atoms in the magnetic flux tube of the FBM. While the magnetic field in the Source is radially constant, it changes radially in pump port 2, where the FBM is situated as shown in the previous section. The rate is proportional to the effective magnetic field at the diode position due to the conservation of the magnetic flux:

$$R_{FBM}(r) \propto B_{FBM}(r) \tag{7.4}$$

This comparison was already done in [Ell19] and a deviation of approximately 1 % was found at $x = 60\,\text{mm}$ for a normalized magnetic field and rate. In the previous chapter, in section 6.4.3.2, it is shown that independently of the magnetic field strength at the FBM, a radial gradient to lower electron rates with an increasing radius is to be expected. This is caused by varying acceptance angles and different scattering probabilities.

For each position of the diode, the magnetic field at that position is simulated. As stated in the previous section, small deviations between the measured and simulated magnetic field are

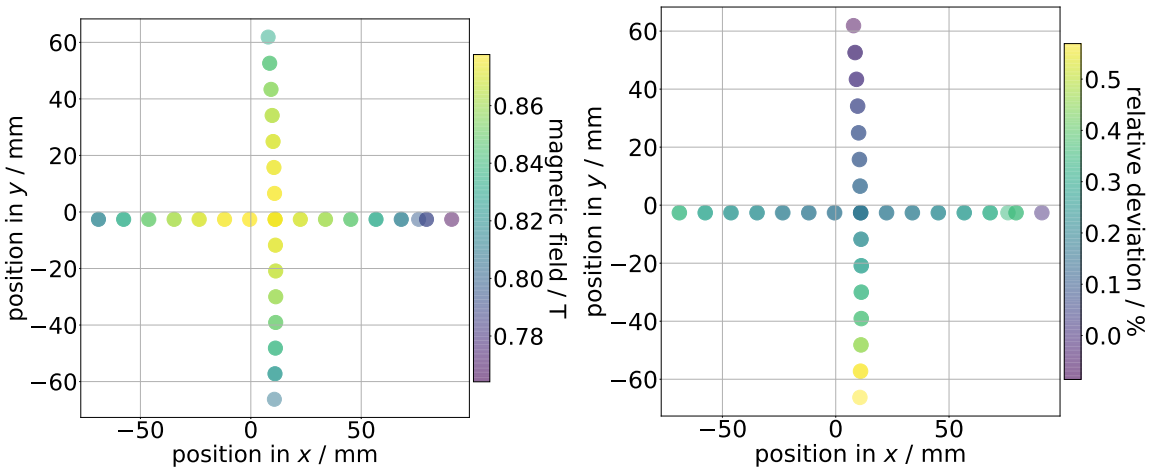

(a) Measured magnetic field.

(b) Relative field deviation to simulation.

Figure 7.11.: *In figure (a) the measured magnetic field in x/y coordinates from a cross-scan through the magnetic flux tube is shown. The agreement of simulation and measurement is shown in figure (b), which shows the relative deviation from the simulated spectrum at each position.*

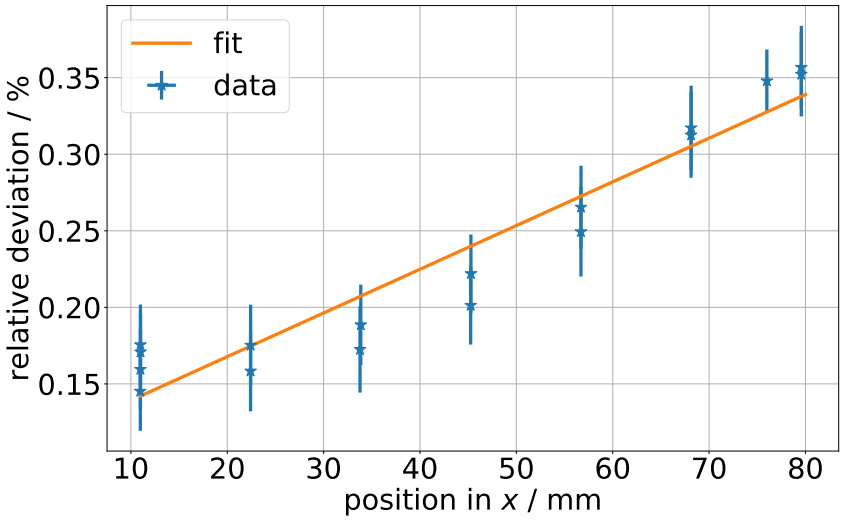

Figure 7.12.: *The relative deviation of the magnetic field as measured by the Hall-sensor during a scan in positive x-direction and a linear fit to the data. The scan went back and forth. Except for the staring position there are two measurement points per position.*

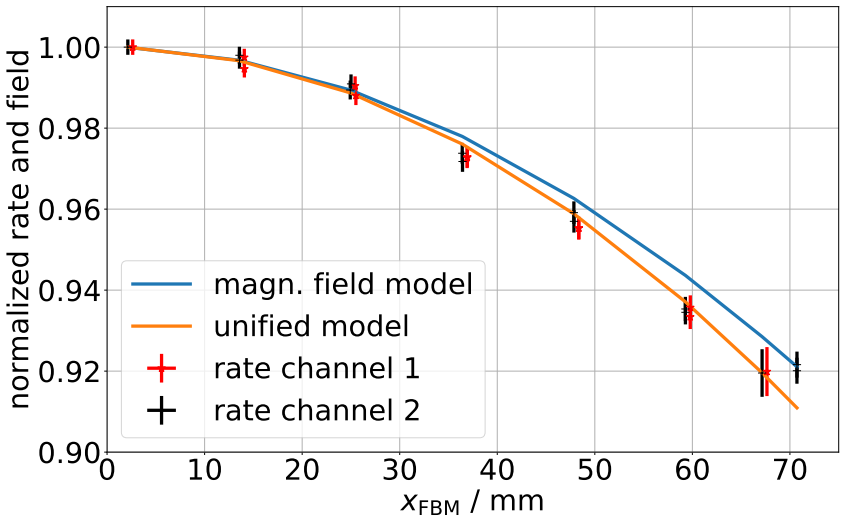

Figure 7.13.: *The radial rate measured by channel 1 and 2 as well as the simulated radial magnetic field (magnetic model) and the magnetic field including the corrections, introduced for First Tritium in section 6.4.3.2, (unified model) are shown. The simulations for the magnetic field and unified model are done for the position of channel 2. The rates and fields are normalized to one regarding their largest measured/simulated value. For a better visibility, the position of channel 1 is shifted by 0.5 mm on the x-axis.*

	magnetic field model	unified model
channel 1	3.46	0.77
channel 2	2.68	1.98

Table 7.1.: *The χ^2/d.o.f. values for channel 1 and 2 to the two models shown in figure 7.13 are given. Both channels are compared to the same magnetic field model.*

found which are within the uncertainties of the Hall-sensor. Nevertheless, as the rate is directly proportional to the magnetic field and variations in the field directly translate into the measured rate. Therefore, the rate is corrected by a fit, as shown in figure 7.12, and visualized as the error bar in figure 7.13 on the rate for both diodes.

In this figure one can see, that the detected rate to magnetic field increasingly deviates for increasing x-positions. The unified model, including the magnetic field and the overall radially dependent detection probability of a single tritium atom decay, describes the data well up to 70 mm. The reduced χ^2/d.o.f. is found in table 7.1 for all rate data shown in this figure.

For both channels, the unified model describes the radial rate gradient better than the magnetic field gradient suggests. Therefore, for the analysis of scans the unified model should be used and potentially be extended to also describe the azimuthal behavior for scans of the entire flux tube. The model only works at $x \leq 70$ mm. This is discussed in the next section.

Deviations of the rate to the model

As can be seen in figure 7.13, the unified model fails to describe the behavior of the rate at approximately 71 mm of channel 2, which also causes a χ^2/d.o.f. of approximately two. The rate of channel 1 at that position drops to zero and is therefore not shown in the figure. Both behaviors indicate a systematic effect not considered so far. Channel 1 is situated approxi-

mately 5.6 mm below channel 2 and is supposedly blocked in the Transport-Section causing the drop to rate of zero. The simulation of the respective magnetic field line with the expected setup configuration during the First Tritium campaign of channel 1 indicates no collision in the Transport-Section. Therefore, this needs to be checked with an electron-gun in the forthcoming measurement campaigns. The situation for channel 2 behaves differently, the rate does not drop to zero, but rather increases compared to the previous position and is approximately the same as at position $x = 59\,\text{mm}$. Simulation of the magnetic field line suggest no collision in the Transport-Section, WGTS, nor Rear-Section up to valve V0 and the distance to the WGTS wall is about 4.5 mm minimum. There are several reasons which might cause the increase in rate by 1 %:

- **Random behavior:** This can be ruled out as the discrepancy is seen on all scans that were performed.

- **Systematics of FBM:** Some systematic might cause an change in rate at the FBM, for example an increase or decrease of the temperature or the stepper motors change the noise behavior. But by taking the difference of the two comparable spectra at 59 mm and 71 mm no feature in the spectrum is found and no change in noise. Additionally a change temperature can ruled out as it fluctuates by 0.03 K.

- **Collision in the Rear-Section:** It might happen that the magnetic field lines intersect with the setup well before valve V0 and therefore in a higher magnetic field which could cause a larger fraction of electrons being reflected. But simulations indicate no collision in the Rear-Section.

- **Fluctuations in the source:** The magnetic field line is rather close to the wall within the WGTS, but the column density fluctuations are two orders of magnitude smaller than the detected increase in rate [Höt12].

- **Increased exposure to tritium:** As the magnetic field line of large radii follows a longer track through pump ports which is not covered with a magnet than smaller radii, the effective volume enlarges and it might be exposed to more tritium. If this model was true, a steady increase in rate to larger radii should be seen in the FBM spectrum, as the effective volume in the pump port increases.

So far, none of the explanations can account for the increase in the electron rate at that specific position. As for channel 1, collisions should be checked within the beam-line to exclude magnetic field lines intersecting with the wall in the WGTS or Rear-Section.

7.5. Covering the FPD with the FBM

During normal tritium operation the FBM must not cover any pixel of the FPD. Therefore, it should be situated in the outer-rim, which is outside of the flux tube hitting the FPD. In scanning mode, the FBM is able to scan the entire flux tube and thereby covers the FPD pixels. Due to the structure of the FPD with 148 pixel a FBM shadow can be seen. The area of the flux tube covered by the FBM detector board and its components attached to it can be seen on the FPD detector pixel. An example simulation is illustrated in figure 7.14. The shadow of the FBM onto the FPD can be fit and one method to fit the shadow is explained in this section.

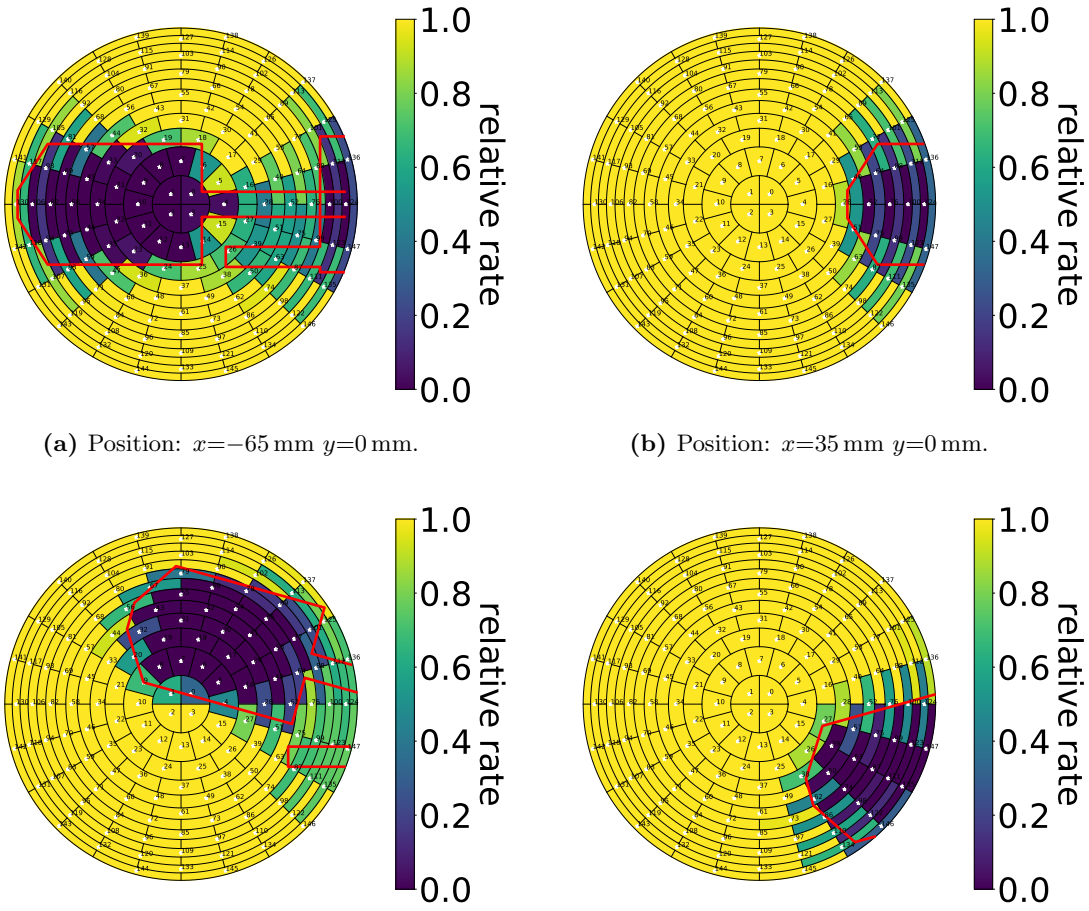

(a) Position: x=−65 mm y=0 mm.

(b) Position: x=35 mm y=0 mm.

(c) Position: x=−20 mm y=35 mm.

(d) Position: x=20 mm y=−35 mm.

Figure 7.14.: *Example relative rate distributions (color-code) on the FPD pixel if the FBM is at the locations indicated in the respective caption. The relative rate is identical to the covered area of the pixel.*

7.5.1. Prerequisites for a fit routine

The result of the analysis presented in this section is shown in figure 7.14. The idea is to model the FBM front-end. As can be seen in the referenced figure, the shape of the front-end does not follow an analytical function. Therefore, the model of the shape is hard-coded, which is according to the hardware specifications. The board and the lever-arm need to be rotatable according to the rotation axis of the toothed-wheel, which is connected to the toothed-bar. This toothed-bar also moves according to the vertical position of the board. If the board moves down vertically, the toothed-bar is retracted and vice versa.

Besides modelling the FBM front-end, the pixel of the FPD need to be modelled. As the fit is done at the position of the FBM, the FPD pixel need to be virtually moved towards the FBM. The FPD is situated in a magnetic field which is approximately three times larger than at the FBM location. Due to the conservation of the magnetic flux (compare 5.6), the effective area is three times larger at the FBM. But, as shown in figure 7.13 the magnetic field depends on the radial position. Therefore, each ring of the FPD pixel is scaled according to the simulated magnetic field it is experiencing. This model assumes that the magnetic field is symmetric and the FPD pixel are centered. Nevertheless, if the FPD is not centered the so-called offset is a free parameter in the fit, but the magnetic field change is not considered then.

With all this information implemented into the routine, figure 7.14 can be simulated. The FBM is placed according to the position of the board tip which can be chosen randomly or set as in the example figures and the FBM as well as the pixel dimension can visualized according to its position. The relative rate is defined as the rate measured for the individual pixel while the FBM covers this pixel divided by the uncovered pixel rate. If the systematic conditions do not change and for a sufficiently large number of events the ratio/relative rate for an uncovered pixel is 1 and for a fully covered pixel 0 Assuming the events are distributed uniformly on the pixels and the number of events N per pixel going towards infinity, the relative rate is equivalent to the covered area of the pixel:

$$R_{\text{relative}}(\text{pixel}) \overset{N\to\infty}{=} A_{\text{covered}}(\text{pixel}) \tag{7.5}$$

Simulations indicate that a reasonable number of events to get a good estimate on the covered pixel area is on the order of 10^3 events. For this low number of events, no routine was developed to calculate the relative area or covered area by the FBM, but 5000 events are randomly and uniformly distributed inside each pixel and a routine checks if each event hit the detector or the FBM front-end.

7.5.2. The fit routine

In the previous section the model of creating relative rates or, equivalently, the ratio of covered pixel calculation is presented. The fit routine relies on that model. As input parameters it requires the relative rate of each pixel. This is calculated from the rates of a covered FPD pixel divided by the rate of the uncovered pixel. The fit routine tries to find the best fit by looking for the left-most pixel with less than a relative rate of 0.8 which is equivalent of a pixel being covered by more than 20 % of its area. The center of that pixel is used as the starting parameters of the fit routine. The square deviation of the relative rate for each pixel is calculated and summed over all pixels. The fit routine tries to minimize this square deviation. As the number of utilized pixels may differ, as pixels can be deactivated, no normalization to the number of pixel is performed. The fit routine has three free parameters, the x,y position of the tip of the FBM board and an offset in y, which is equivalent of the FPD pixel being moved

vertically up or down compared to the FBM. To ease the fit only horizontal positions of the FBM are investigated and therefore only the x position of the tip and the relative offset remain as fit parameters. Starting from the initial position, the fit routine searches for smaller square deviations by virtually shifting the board by 30 mm radially and azimuthally while also shifting the offset in y. As the FBM is only horizontally positioned, the azimuth is either 0° or 180° and therefore the FBM is only shifted along the x-axis. Measurements with the FBM during the 2017 Krypton phase indicate that the FBM is shifted downwards compared to the FPD, hence the y-offset parameter is fit from 0 mm to −10 mm in 0.1 mm steps. If a smaller deviation is found by shifting the FBM (initially by 30 mm) on the x-axis the FBM is moved to that position and the search starts from the beginning. Otherwise the radius is divided by two and the search continues in a closer range. This routine runs until the radial shift is smaller than 0.1 mm.

7.5.3. Verification of the fit routine

The fit routine can be tested in simulation. This is done by placing the FBM randomly on the x-axis in between −70 mm to 60 mm and 0 mm to −10 mm for the offset in vertical y position and trying to fit this position. The range above 60 mm is excluded as not a sufficient amount of information can be provided to the fitter to get a reasonable result. This verification assumes perfect systematic and statistical conditions. That means, the dimension of the front-end is perfectly known as well as the magnetic field and excludes statistical fluctuations of the rate. The result can be seen in figure 7.15.

This figure proves that the fit routine is able to find the true position of the board with the accuracy of ≈ 0.1 mm (mean: $\mu = (0.08 \pm 0.05)$ mm). This is restricted by the minimum step-size of 0.1 mm. The spikes in the combined spectrum stem from fits above 45 mm in x and above −8 mm in the relative offset as the fit routine is less precise for large x and offset positions as the FBM creates less of a shadow onto the FPD pixel.

7.5.4. Fit First Tritium data

During First Tritium several scans with the FBM were performed, but the runs of the FPD and FBM were not optimized for performing a fit of the FBM position with FPD pixel data. Therefore, an FPD run is chosen with a sufficient number of events to calculate the pixel rate for an uncovered detector and several positions of the FBM board in between −80 mm to 0 mm. The rate per pixel was about 150 cps. An integration time of approximately 200 s creates a sufficient number of events for the fit routine. Some pixel are deactivated, including the two outer rings as the rate on those pixels is too low. Pixel, which are not affecting the positional fit, because they are far outside the FBM shadow are also deactivated. This enables a faster fit routine and removes statistical fluctuations of those pixels. However, the pixels covered by the FBM board need to be enabled for a more stable fit routine. That means, even the outer-most pixels are used as well as pixels covered by the FBM board at run start (especially pixel 100, 112, and 123). In the fit routine, the rate is not corrected for fluctuations of the column density or tritium purity. The result is shown in figure 7.16

It can be seen in figure 7.16 (a), that the deviation in x-direction between the measured and and fit value differs by 0.2 mm and the offset in y-direction is −6.8 mm. At first glance, the fit looks reasonable, however pixels 141 and 129 show a decrease in the relative rate. They could be covered by the FBM board or these are statistical fluctuations. This cannot be disentangled. The largest discrepancy shows pixel 64 on the figure, the pixel is not covered by the FBM board shadow, but according to the data it should be covered by more than 50 %. Along the lever-arm of the FBM the cabling of the FBM board to the support structures is guided. The cabling is attached to the Peek-connector of the board and therefore wires can explain the drop on pixels

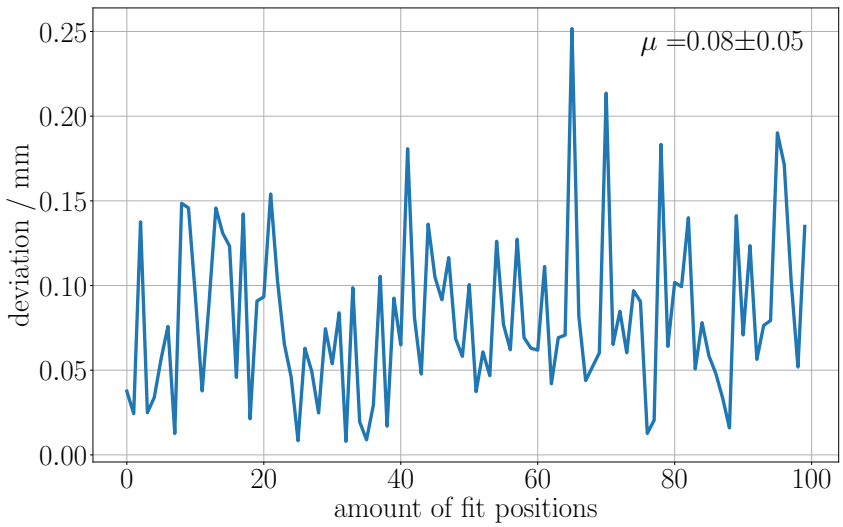

(a) Total deviation.

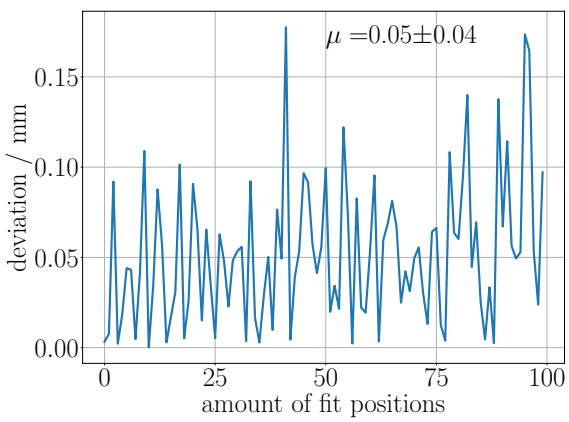

(b) Deviation in x-position.

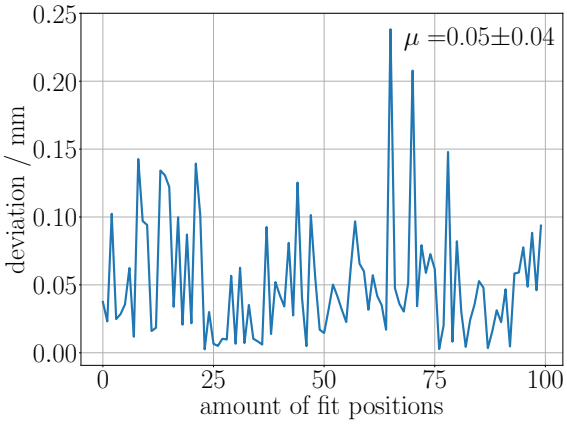

(c) Deviation of the relative y-offset.

Figure 7.15.: *The deviations of the fit position to the true position. In figure (a) the total deviation, in (b) the deviation on the x-position and in (c) the deviation on the offset is given. Additionally, the mean deviations μ are shown with their respective standard deviations.*

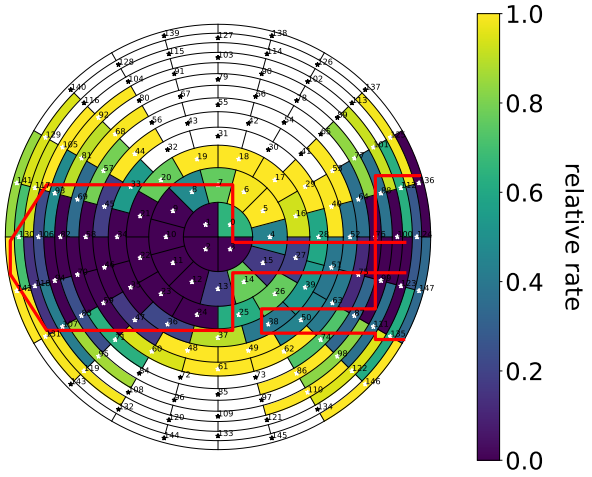

(a) Measured position: $x_{\mathrm{enc}} = -68.7\,\mathrm{mm}$, fit position: $x = -68.5\,\mathrm{mm}$, $y_{\mathrm{offset}} = -6.8\,\mathrm{mm}$.

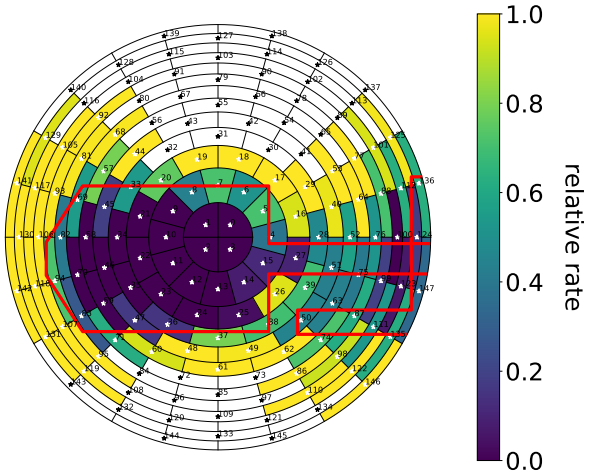

(b) Measured position: $x_{\mathrm{enc}} = -57.3\,\mathrm{mm}$, fit position: $x = -56.6\,\mathrm{mm}$, $y_{\mathrm{offset}} = -7.1\,\mathrm{mm}$.

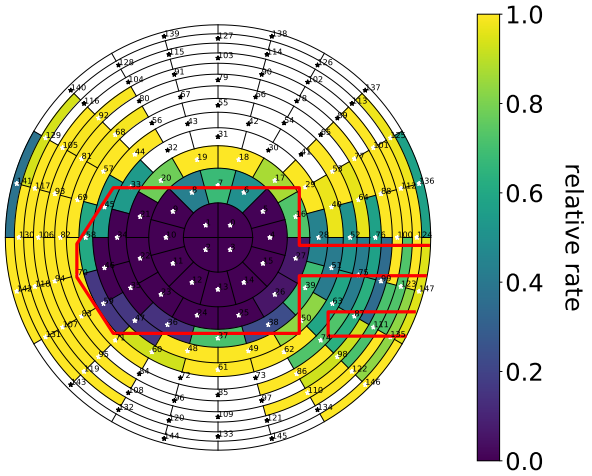

(c) Measured position: $x_{\mathrm{enc}} = -45.8\,\mathrm{mm}$, fit position: $x = -46.5\,\mathrm{mm}$, $y_{\mathrm{offset}} = -7.6\,\mathrm{mm}$.

Figure 7.16.: *The fit results of three different FBM locations and their respective FPD rate plot. The measured FBM position in x-direction is given in the label as well as the fit position. The total diameter of the FPD at the FBM location is about 140 mm.*

0 and 7 if the FBM is positioned further left (smaller x position). This could explain the drop in rate of pixel 64. The second figure (b) has a larger difference in x of 0.7 mm and the y-offset increased by 0.3 mm absolute. Pixel 88 sees a drop in the relative rate while it is not covered by the FBM front-end. This could be explained by the cabling attached to the lever-arm. Figure (c) results in a difference of -0.7 mm in x and a further shift of the FPD downwards compared to the FPD by 0.5 mm. This fit shows the same behavior of pixels 141 and 129 as in the first fit. Therefore, the drop is explained by statistical fluctuations. Additionally, the problem of covering the FPD at the start of the run can be seen on pixel 100 and 124. They have a relative rate of about one although they are covered by the lever-arm.

Discussion and outlook

Unfortunately, no FPD data is available at larger x-position values, of $x > -45$ mm. The influence of the cabling decreases for larger x-positions. Additionally, the potential trend of decreasing y-offset, or in other words a tilted FPD pixel distribution, could have been investigated at larger x-positions. In the future, the cabling should be modelled and the real magnetic field should be considered for each FPD pixel in the fit. Nonetheless, simulations indicate a working fit routine with high accuracy for known systematic properties.

Besides all the potential improvements in future, the fit results of the x-position match to the encoder values by less than 1 mm. This suggests that the relative horizontal alignment of the FBM and FPD agree during the First Tritium campaign.

CONCLUSION AND OUTLOOK

The task of the Forward Beam Monitor (FBM) is to measure the beta electron rate from the KATRIN tritium Source with 0.1 % precision in the timescale of 1 min. Although, the beta electron rate during the First Tritium campaign was low, due to a tritium purity of about 0.5 % in the Source, the FBM did prove a rate stability of approximately 0.1 % per day. This is better than required for neutrino mass analysis.

In this thesis, the expected correlation of the tritium purity and column density was shown. It was also shown that the FBM is stable on short time scales when taking the fluctuations of tritium purity and column density into account.

The goal of this thesis specifically was to create a simulation model in order to estimate the beta electron rate at the *p*-*i*-*n*-diode detectors and to simulate the shape of the beta electron spectrum. To do that, a new approach utilizing graphics cards, designed for highly-parallel calculations, were used and allowed a significant increase in speed (a factor of approximately 100) of Monte-Carlo simulations of beta electrons interacting with the tritium gas in the Source compared to available Monte-Carlo frameworks (Kassiopeia) on conventional processors (CPUs). It was also shown that the simulation output on graphic cards is identical to Kassiopeia simulations.

Hence, the approach on graphics cards was successful and proved that electrons can be tracked in parallel through the Source of KATRIN efficiently on GPUs. In future, this method should be refined, i.e. it should be utilized to investigate the tritium endpoint region, not only in dependence of energy loss functions and cross-sections, but also by implementing the real magnetic field settings to investigate the effect of small disturbances in the magnetic field onto the beta electron spectrum endpoint region.

The FBM is able to measure almost the entire beta spectrum from approximately 5 keV to 18.6 keV. Therefore, effects, which are negligible in neutrino mass analysis, have to be considered besides scattering in the Source. Specifically, beta electrons that leave the Source upstream towards the Rear-Section of the experiment need to be considered. These have a backscattering probability of almost 50 % for vertically impinging electrons and, of all the electrons hitting the Rear-Wall, these have the smallest backscattering probability. The electrons can then be transmitted through the Source and guided to the FBM. Although the probability of a change in kinetic energy and polar angle is high due to the interactions, the electron may still be above the FBM detection threshold and therefore needs to be accounted for.

Additionally, electrons leaving the Source upstream towards the FBM can be magnetically reflected, transmitted through the Source and backscattered off the Rear-Wall. This work has shown that all of these effects need to be considered, especially in nominal KATRIN operation

as upstream electrons going directly from the Source to the Rear-Wall contribute about 18 % and electrons reflected in the Transport-Section about 14 % to the total FBM rate at a 5 keV energy threshold.

In order to simulate the beta spectrum at the FBM, the experiment cannot be simulated as one component, but has to be split into several smaller components. To do that the response matrix approach is used. In this thesis, it has proven to work successfully. In future, the method can be refined, meaning the energy bin width can be decreased, but also the polar angle bin width should be decreased. This work has shown that a polar angle bin width of 5° may cause problems at varying magnetic field strengths, as the electrons from several polar angle are compressed into one bin.

Nevertheless, the measured spectrum was reproduced by the simulation above 8 keV and also the radial rate behavior was predicted by the simulation. One of the biggest challenges was the simulation of the *p-i-n*-diode response. Electron-gun measurements have shown that the diode does not produce the same results depending on the electron-gun spot position on the diode. Hence, the simulation of the dead-layer of the diode had to be complemented by a numerical model based on measurements. Therefore, it is recommended to measure the diode response instead of simulating it to include edge effects of the diode which could not be reproduced in simulation. The electron-gun rate to measure the response should be rather low (recommendation < 2000 cps) to have less pile-up in the spectrum, and to add the expected electron-electron pile-up by simulation at different rates.

However, the response matrix approach should also be tested for neutrino mass fitting as a small binning on the order of 1 eV or lower close to the endpoint can be used and a single response matrix can be calculated for the entire experiment. Hence, a single response matrix might be sufficient to represent the entire experiment and the neutrino mass shift only affects the initial beta spectrum. But this method requires a stable column density and tritium purity or different matrices for different Source settings.

The next measurement phase of KATRIN will be performed at nominal KATRIN Source settings with a tritium purity of about 95 % and therefore a ten times smaller diode at the FBM is used. The previous measurements have shown that the FBM is ready and stable enough for the hunt of the neutrino mass in the KATRIN experiment. The next goal is to upgrade and exchange the detector by a silicon drift detector called Tristan. It has an energy resolution of several hundred electronvolt and would enable the FBM to look for sterile neutrinos in the kilo-electronvolt range. In order to achieve that, the presented method in this work becomes even more crucial and can easily be extended by the response of the silicon drift detector.

APPENDIX A

APPENDIX

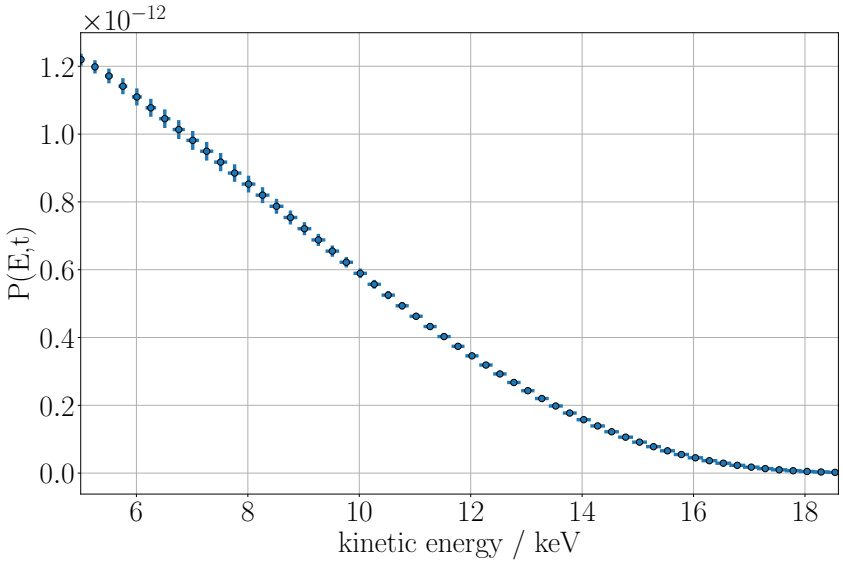

Figure A.I.: *The error on the nominal KATRIN configuration simulation on the detection probability as well as the energy uncertainty. For a better visualization only every fith simulated data point is shown.*

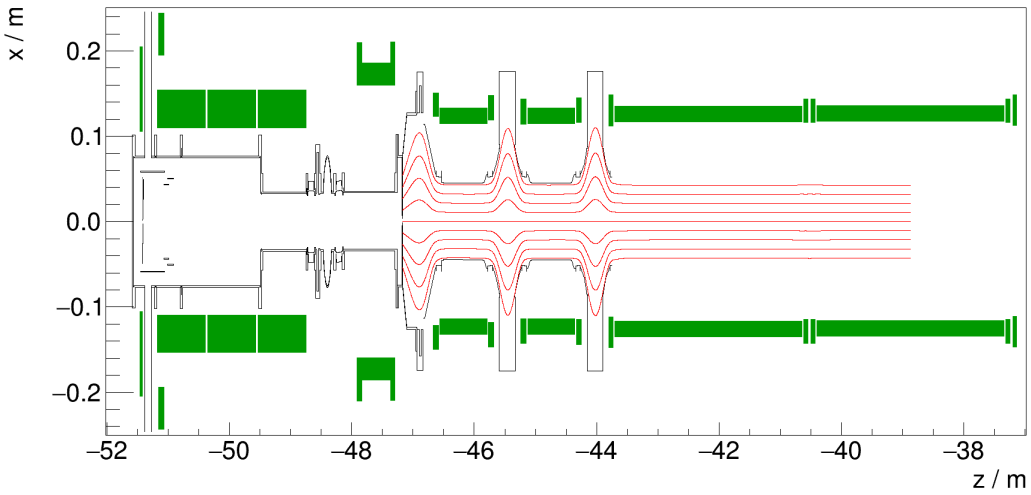

Figure A.II.: *The magnetic field lines in nominal KATRIN operation in red color. Their origin is in the center of the WGTS at $z \approx -39\,\mathrm{m}$. Electrons, neglecting interactions with the gas inside of the Source, follow these lines if their momentum has a longitudinal component pointing to negative z. These electrons hit the rear-wall at $z \approx -47\,\mathrm{m}$.*

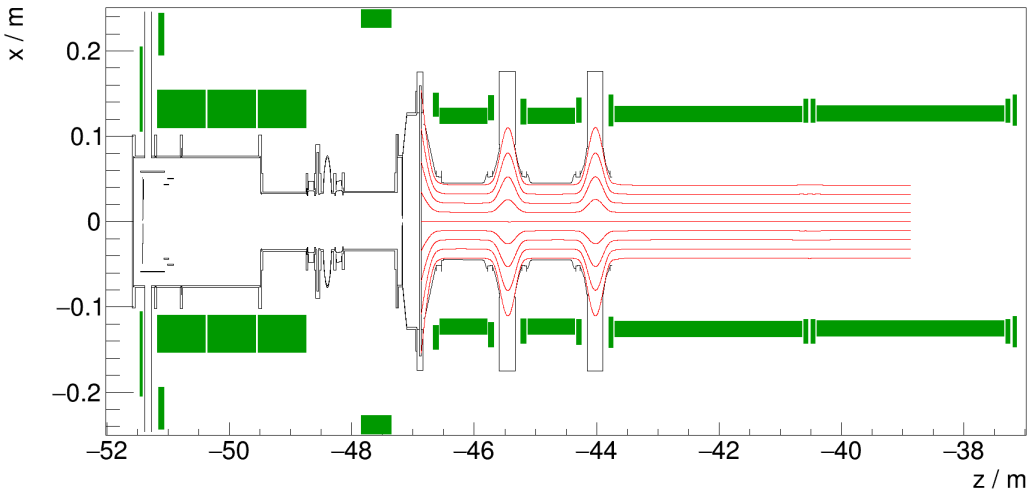

Figure A.III.: *The magnetic field setup during First Tritium. It can be compared to the nominal KATRIN configuration in figure A.II. During First Tritium, valve V0 was closed and also the Rear-Section magnets were off. Therefore, electrons are not able to reach the rear-wall, but hit valve V0 instead.*

r_S / mm	Φ_S / °	B_S / T	B_{max} / T	x(B_{max}) / mm	y(B_{max}) / mm	z(B_{max}) / m	θ_{accept} / °	fraction	B_{final} / T	x_{final}/ mm	y_{final} / mm	z_{final} / m	θ_{pitch} / °	θ_{inc} / °
0	0	2.5217	2.527	-0.0004	0.0002	-41.293	92.527	0.960	1.588	0.130	-0.344	-47.170	127.562	179.905
5	0	2.5217	2.527	4.9947	0.0002	-41.293	92.527	0.960	1.587	6.432	-0.343	-47.170	127.569	178.667
10	0	2.5217	2.527	9.9898	0.0002	-41.293	92.527	0.960	1.586	12.739	-0.341	-47.170	127.601	177.357
15	0	2.5217	2.527	14.985	0.0002	-41.293	92.527	0.960	1.584	19.055	-0.338	-47.170	127.646	176.038
20	0	2.5217	2.527	19.9801	0.0002	-41.292	92.527	0.960	1.581	25.391	-0.333	-47.170	127.729	174.708
25	0	2.5217	2.527	24.9752	0.0002	-41.292	92.527	0.960	1.577	31.744	-0.327	-47.170	127.820	173.366
30	0	2.5217	2.527	29.9704	0.0002	-41.291	92.527	0.960	1.571	38.130	-0.319	-47.170	127.945	172.005
35	0	2.5217	2.527	34.9655	0.0002	-41.291	92.527	0.960	1.565	44.541	-0.309	-47.170	128.081	170.623
40	0	2.5217	2.527	39.9606	0.0002	-41.290	92.527	0.960	1.558	51.002	-0.297	-47.170	128.255	169.215
45	0	2.5217	2.527	44.9558	0.0002	-41.289	92.528	0.960	1.550	57.505	-0.282	-47.170	128.449	167.778
5	180	2.5217	2.527	-4.9956	0.0002	-41.293	92.527	0.960	1.588	-6.172	-0.343	-47.170	127.562	178.708
10	180	2.5217	2.527	-9.9907	0.0002	-41.293	92.527	0.960	1.586	-12.480	-0.341	-47.170	127.601	177.397
15	180	2.5217	2.527	-14.9859	0.0002	-41.293	92.527	0.960	1.584	-18.794	-0.338	-47.170	127.640	176.079
20	180	2.5217	2.527	-19.981	0.0002	-41.292	92.527	0.960	1.581	-25.127	-0.333	-47.170	127.718	174.749
25	180	2.5217	2.527	-24.9761	0.0002	-41.292	92.527	0.960	1.577	-31.483	-0.326	-47.170	127.819	173.406
30	180	2.5217	2.527	-29.9713	0.0002	-41.291	92.527	0.960	1.572	-37.859	-0.318	-47.170	127.927	172.046
35	180	2.5217	2.527	-34.9664	0.0002	-41.291	92.527	0.960	1.566	-44.276	-0.308	-47.170	128.077	170.663
40	180	2.5217	2.527	-39.9615	0.0002	-41.290	92.527	0.960	1.559	-50.728	-0.296	-47.170	128.240	169.256
45	180	2.5217	2.527	-44.9567	0.0002	-41.289	92.528	0.960	1.551	-57.223	-0.281	-47.170	128.427	167.820

Table A.I.: *Detailed overview of the properties of the setup for electrons traveling from the Source to the Rear-Section and hitting the Rear-Wall. It gives a representation of the properties of the Rear-Section at different radii and mirrored by 180° in azimuth. It completes table 5.1 by stating the position of the maximum magnetic field, by the fraction how many electrons are transmitted and the final position of the tracks.*

r_S / mm	Φ_S / °	B_S / T	B_{max} / T	$x(B_{max})$ / mm	$y(B_{max})$ / mm	$z(B_{max})$ / m	θ_{accept} / °	fraction	B_{final} / T	x_{final}/ mm	y_{final} / mm	z_{final} / m	θ_{pitch} / °	θ_{inc} / °
0	0	2.5216	2.526	-0.0005	0.0001	-41.270	92.487	0.960	0.246	0.233	-0.977	-46.866	161.807	179.617
5	0	2.5216	2.526	4.9948	0.0001	-41.270	92.487	0.960	0.245	16.254	-0.977	-46.866	161.840	176.308
10	0	2.5216	2.526	9.9901	0.0001	-41.270	92.487	0.960	0.243	32.410	-0.977	-46.866	161.938	172.543
15	0	2.5216	2.526	14.9854	0.0001	-41.270	92.487	0.960	0.238	48.849	-0.977	-46.866	162.105	168.713
20	0	2.5216	2.526	19.9807	0.0001	-41.269	92.488	0.960	0.233	65.724	-0.976	-46.866	162.342	164.790
25	0	2.5216	2.526	24.9759	0.0001	-41.269	92.488	0.960	0.224	83.250	-0.976	-46.866	162.660	160.740
30	0	2.5216	2.526	29.9712	0.0001	-41.268	92.488	0.960	0.214	101.671	-0.977	-46.866	163.065	156.530
35	0	2.5216	2.526	34.9665	0.0001	-41.267	92.488	0.960	0.202	121.309	-0.977	-46.866	163.565	152.119
40	0	2.5216	2.526	39.9618	0.0001	-41.267	92.488	0.960	0.188	142.630	-0.978	-46.866	164.175	147.467
45	0	2.5216	2.526	44.9571	0.0001	-41.266	92.488	0.960	0.171	166.312	-0.980	-46.866	164.913	142.523
5	180	2.5216	2.526	-4.9958	0.0001	-41.270	92.487	0.960	0.245	-15.791	-0.977	-46.866	161.842	176.165
10	180	2.5216	2.526	-9.9911	0.0001	-41.270	92.487	0.960	0.243	-31.955	-0.977	-46.866	161.943	172.399
15	180	2.5216	2.526	-14.9864	0.0001	-41.270	92.487	0.960	0.238	-48.406	-0.976	-46.866	162.113	168.565
20	180	2.5216	2.526	-19.9816	0.0001	-41.269	92.488	0.960	0.232	-65.297	-0.976	-46.866	162.352	164.638
25	180	2.5216	2.526	-24.9769	0.0001	-41.269	92.488	0.960	0.224	-82.860	-0.976	-46.866	162.676	160.582
30	180	2.5216	2.526	-29.9722	0.0001	-41.268	92.488	0.960	0.214	-101.307	-0.976	-46.866	163.082	156.365
35	180	2.5216	2.526	-34.9675	0.0001	-41.267	92.488	0.960	0.202	-120.995	-0.976	-46.866	163.586	151.946
40	180	2.5216	2.526	-39.9628	0.0001	-41.267	92.488	0.960	0.187	-142.372	-0.977	-46.866	164.199	147.285
45	180	2.5216	2.526	-44.9581	0.0001	-41.266	92.488	0.960	0.171	-166.141	-0.979	-46.866	164.941	142.330

Table A.II.: *Detailed overview of the properties of the setup for electrons traveling from the Source to the Rear-Section with V0 closed. It gives a representation of the properties of the Rear-Section at different radii and mirrored by 180° in azimuth. It completes table 5.3 by stating the position of the maximum magnetic field, by the fraction how many electrons are transmitted and the final position of the tracks.*

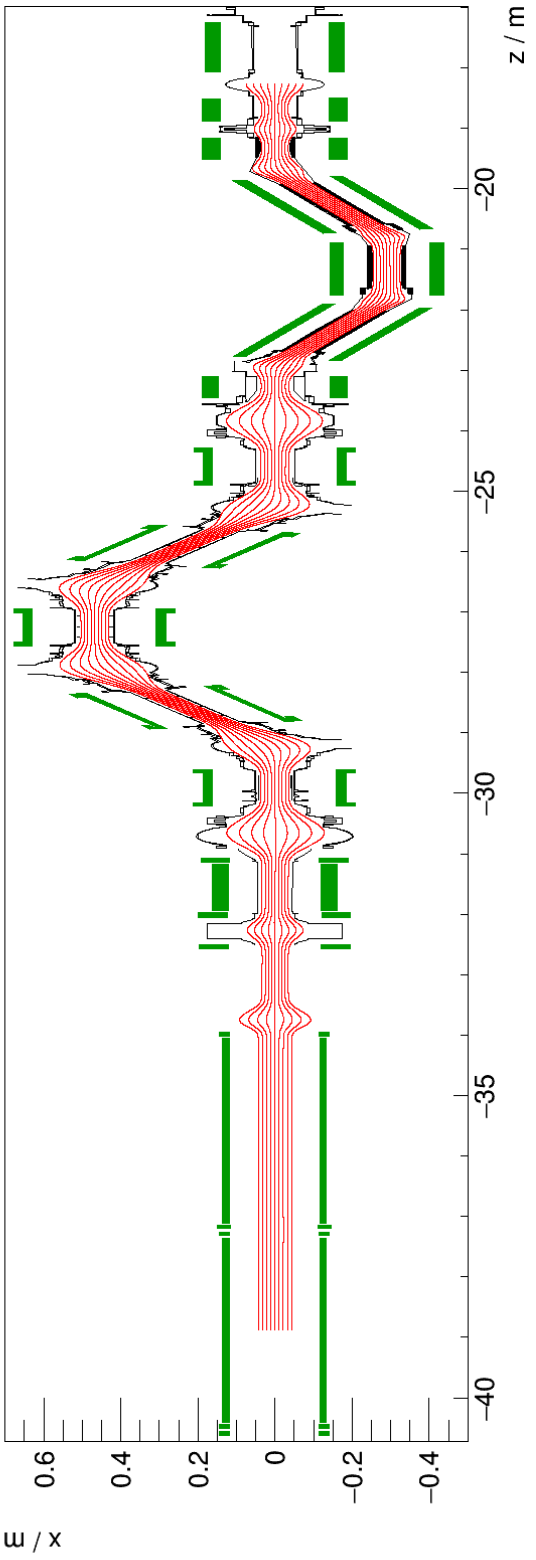

Figure A.IV.: *The magnetic field line from the center of the Source at $z \approx -39\,m$ towards the location of the FBM in pump-port 2 of the CPS at $z \approx -18\,m$. Electrons with a component of their longitudinal momentum in positive z direction follow these magnetic field lines. They undergo different magnetic field strengths and electrons with a large pitch angle are reflected in this Transport-Section before they can be detected at the FBM. An overview about the acceptance angles is given in table 5.5*

r_S / mm	Φ_S / °	B_S / T	B_{max} / T	$x(B_{max})$ / mm	$y(B_{max})$ / mm	$z(B_{max})$ / m	θ_{accept} / °	fraction	B_{final} / T	x_{final}/ mm	y_{final} / mm	z_{final} / m	θ_{pitch} / °	θ_{inc} / °
0	0	2.5216	3.976	-0.4096	-1.2197	-32.775	52.781	0.400	0.879	1.091	6.121	-18.271	28.053	0.071
5	0	2.5216	3.976	3.572	-1.22	-32.775	52.781	0.400	0.878	9.558	6.136	-18.271	28.031	0.075
10	0	2.5216	3.976	7.5535	-1.2208	-32.775	52.781	0.400	0.875	18.041	6.148	-18.271	27.974	0.079
15	0	2.5216	3.977	11.5349	-1.2222	-32.774	52.781	0.400	0.870	26.555	6.157	-18.271	27.882	0.082
20	0	2.5216	3.977	15.5161	-1.2241	-32.773	52.780	0.400	0.862	35.114	6.163	-18.271	27.755	0.087
25	0	2.5216	3.977	19.4972	-1.2266	-32.772	52.780	0.400	0.853	43.734	6.165	-18.271	27.592	0.089
30	0	2.5216	3.979	24.2771	2.9802	-18.686	52.759	0.390	0.842	52.431	6.164	-18.271	27.385	0.091
35	0	2.5216	3.982	28.2511	2.9658	-18.686	52.725	0.390	0.829	61.223	6.160	-18.271	27.136	0.094
40	0	2.5216	3.987	32.2216	2.9476	-18.686	52.685	0.390	0.813	70.130	6.151	-18.271	26.848	0.094
45	0	2.5216	3.991	36.1883	2.9252	-18.686	52.641	0.390	0.796	79.172	6.137	-18.271	26.518	0.090
5	180	2.5216	3.976	-4.3913	-1.22	-32.775	52.781	0.400	0.879	-7.376	6.102	-18.271	28.041	0.067
10	180	2.5216	3.976	-8.3731	-1.2208	-32.775	52.781	0.400	0.876	-15.856	6.080	-18.271	27.993	0.064
15	180	2.5216	3.977	-12.355	-1.2221	-32.774	52.781	0.400	0.871	-24.363	6.054	-18.271	27.912	0.061
20	180	2.5216	3.977	-16.337	-1.2241	-32.773	52.781	0.400	0.865	-32.913	6.024	-18.271	27.794	0.057
25	180	2.5216	3.977	-20.319	-1.2266	-32.772	52.780	0.400	0.856	-41.522	5.990	-18.271	27.642	0.055
30	180	2.5216	3.978	-23.518	2.8841	-18.686	52.764	0.390	0.845	-50.206	5.951	-18.271	27.447	0.052
35	180	2.5216	3.982	-27.4971	2.852	-18.686	52.730	0.390	0.832	-58.982	5.905	-18.271	27.207	0.051
40	180	2.5216	3.986	-31.4737	2.8151	-18.686	52.692	0.390	0.818	-67.870	5.854	-18.271	26.929	0.050
45	180	2.5216	3.990	-35.4476	2.7731	-18.686	52.648	0.390	0.801	-76.889	5.794	-18.271	26.610	0.049

Table A.III.: *Detailed overview of the properties of the setup for electrons traveling from the Source to the FBM. It gives a representation of the properties of the Transport-Section at different radii and mirrored by 180° in azimuth. It completes table 5.5 by stating the position of the maximum magnetic field, by the fraction how many electrons are transmitted and the final position of the tracks.*

BIBLIOGRAPHY

[Abd+02] J. N. Abdurashitov et al. "Solar neutrino flux measurements by the Soviet-American gallium experiment (SAGE) for half the 22-year solar cycle". In: *Journal of Experimental and Theoretical Physics* 95.2 (Aug. 2002), pp. 181–193. ISSN: 1090-6509. DOI: 10.1134/1.1506424. URL: https://doi.org/10.1134/1.1506424.

[Agh+18] N. Aghanim et al. "Planck 2018 results. VI. Cosmological parameters". In: (2018). arXiv: 1807.06209 [astro-ph.CO].

[Ago+03] S. Agostinelli et al. "Geant4—a simulation toolkit". In: *Nuclear Instruments and Methods in Physics Research Section A: Accelerators, Spectrometers, Detectors and Associated Equipment* 506.3 (2003), pp. 250–303. ISSN: 0168-9002. DOI: https://doi.org/10.1016/S0168-9002(03)01368-8. URL: http://www.sciencedirect.com/science/article/pii/S0168900203013688.

[Ago+16] M. Agostini et al. "Search of Neutrinoless Double Beta Decay with the GERDA Experiment". In: *Nuclear and Particle Physics Proceedings* 273-275 (2016). 37th International Conference on High Energy Physics (ICHEP), pp. 1876–1882. ISSN: 2405-6014. DOI: https://doi.org/10.1016/j.nuclphysbps.2015.09.303. URL: http://www.sciencedirect.com/science/article/pii/S2405601415007920.

[Ago+18] M. Agostini et al. "Improved Limit on Neutrinoless Double-β Decay of ^{76}Ge from GERDA Phase II". In: *Phys. Rev. Lett.* 120 (13 Mar. 2018), p. 132503. DOI: 10.1103/PhysRevLett.120.132503. URL: https://link.aps.org/doi/10.1103/PhysRevLett.120.132503.

[Aha+05] B. Aharmim et al. "Electron energy spectra, fluxes, and day-night asymmetries of ^{8}B solar neutrinos from measurements with NaCl dissolved in the heavy-water detector at the Sudbury Neutrino Observatory". In: *Phys. Rev. C* 72 (5 Nov. 2005), p. 055502. DOI: 10.1103/PhysRevC.72.055502. URL: https://link.aps.org/doi/10.1103/PhysRevC.72.055502.

[Ahm+02] Q. R. Ahmad et al. "Direct Evidence for Neutrino Flavor Transformation from Neutral-Current Interactions in the Sudbury Neutrino Observatory". In: *Phys. Rev. Lett.* 89 (1 June 2002), p. 011301. DOI: 10.1103/PhysRevLett.89.011301. URL: https://link.aps.org/doi/10.1103/PhysRevLett.89.011301.

[All+16] J. Allison et al. "Recent developments in Geant4". In: *Nuclear Instruments and Methods in Physics Research Section A: Accelerators, Spectrometers, Detectors and Associated Equipment* 835 (2016), pp. 186–225. ISSN: 0168-9002. DOI: https://

doi.org/10.1016/j.nima.2016.06.125. URL: http://www.sciencedirect.com/science/article/pii/S0168900216306957.

[Alt+05] M. Altmann et al. "Complete results for five years of GNO solar neutrino observations". In: *Physics Letters B* 616.3 (2005), pp. 174–190. ISSN: 0370-2693. DOI: https://doi.org/10.1016/j.physletb.2005.04.068. URL: http://www.sciencedirect.com/science/article/pii/S0370269305005149.

[Ams+15] J.F. Amsbaugh et al. "Focal-plane detector system for the KATRIN experiment". In: *Nucl. Instrum. Meth. A* 778 (2015), pp. 40–60. DOI: 10.1016/j.nima.2014.12.116. eprint: 1404.2925.

[Are+18] M. Arenz et al. "First transmission of electrons and ions through the KATRIN beamline". In: *Journal of Instrumentation* 13.04 (Apr. 2018), P04020–P04020. DOI: 10.1088/1748-0221/13/04/p04020. URL: https://doi.org/10.1088%2F1748-0221%2F13%2F04%2Fp04020.

[Ase+00] V.N. Aseev et al. "Energy loss of 18 keV electrons in gaseous T and quench condensed D films". In: *The European Physical Journal D - Atomic, Molecular, Optical and Plasma Physics* 10.1 (Mar. 2000), pp. 39–52. ISSN: 1434-6079. DOI: 10.1007/s100530050525. URL: https://doi.org/10.1007/s100530050525.

[Ase+11] V.N. Aseev et al. "Upper limit on the electron antineutrino mass from the Troitsk experiment". In: *Phys. Rev. D* 84 (11 2011), p. 112003. DOI: 10.1103/PhysRevD.84.112003. eprint: 1108.5034.

[Bab10] Martin Babutzka. "Untersuchung eines verfahrbaren Monitordetektors zur Überwachung der Aktivität des β-Zerfalls in der kryogenen Pumpstrecke des KATRIN-Experiments". Diploma Thesis. Karlsruher Institut für Technologie (KIT), 2010. URL: http://www.katrin.kit.edu/publikationen/dth-babutzka.pdf.

[Bab14] Martin Babutzka. "Design and development for the Rearsection of the KATRIN experiment". PhD thesis. 2014.

[Bah64] John N. Bahcall. "Solar Neutrinos. I. Theoretical". In: *Phys. Rev. Lett.* 12 (11 Mar. 1964), pp. 300–302. DOI: 10.1103/PhysRevLett.12.300. URL: https://link.aps.org/doi/10.1103/PhysRevLett.12.300.

[Bec01] Henri Becquerel. "The Radio-Activity of Matter". In: *Nature* 63 (1901), pp. 396–398. DOI: 10.1038/063396d0. URL: https://doi.org/10.1038/063396d0.

[Bil10] Samoil Bilenky. *Introduction to the Physics of Massive and Mixed Neutrinos*. Lecture Notes in Physics, Teil 817. Berlin, Heidelberg: Springer-Verlag Berlin Heidelberg, 2010. ISBN: 978-3-642-14043-3. DOI: 10.1007/978-3-642-14043-3.

[Bog+00] J Boger et al. "The Sudbury Neutrino Observatory". In: *Nuclear Instruments and Methods in Physics Research Section A: Accelerators, Spectrometers, Detectors and Associated Equipment* 449.1 (2000), pp. 172–207. ISSN: 0168-9002. DOI: https://doi.org/10.1016/S0168-9002(99)01469-2. URL: http://www.sciencedirect.com/science/article/pii/S0168900299014692.

[BP78] S.M. Bilenky and B. Pontecorvo. "Lepton mixing and neutrino oscillations". In: *Physics Reports* 41.4 (1978), pp. 225–261. ISSN: 0370-1573. DOI: https://doi.org/10.1016/0370-1573(78)90095-9. URL: http://www.sciencedirect.com/science/article/pii/0370157378900959.

[BPT80] G Beamson, H Q Porter, and D W Turner. "The collimating and magnifying properties of a superconducting field photoelectron spectrometer". In: *Journal of Physics E: Scientific Instruments* 13.1 (Jan. 1980), pp. 64–66. DOI: 10.1088/0022-3735/13/1/018. URL: https://doi.org/10.1088%2F0022-3735%2F13%2F1%2F018.

[BR97] R. Brun and F. Rademakers. "ROOT - An object oriented data analysis framework". In: *Nuclear Instruments and Methods in Physics Research Section A: Accelerators, Spectrometers, Detectors and Associated Equipment* 389.1–2 (1997), pp. 81–86. DOI: 10.1016/S0168-9002(97)00048-X.

[Cha14] J Chadwick. "Intensitätsverteilung im magnetischen Spectrum der β-Strahlen von radium B + C". In: *Verhandl. Dtsc. Phys. Ges.* 16 (1914), p. 383. URL: https://cds.cern.ch/record/262756.

[Cha32] J Chadwick. "Possible Existence of a Neutron". In: *Nature* 129 (1932), p. 312. DOI: 10.1038/129312a0. URL: https://doi.org/10.1038/129312a0.

[Dan+62] G. Danby et al. "Observation of High-Energy Neutrino Reactions and the Existence of Two Kinds of Neutrinos". In: *Phys. Rev. Lett.* 9 (1 July 1962), pp. 36–44. DOI: 10.1103/PhysRevLett.9.36. URL: https://link.aps.org/doi/10.1103/PhysRevLett.9.36.

[Dav94] Raymond Davis. "A review of the homestake solar neutrino experiment". In: *Progress in Particle and Nuclear Physics* 32 (1994), pp. 13–32. ISSN: 0146-6410. DOI: https://doi.org/10.1016/0146-6410(94)90004-3. URL: http://www.sciencedirect.com/science/article/pii/0146641094900043.

[Dec+90] D. Decamp et al. "A precise determination of the number of families with light neutrinos and of the Z boson partial widths". In: *Physics Letters B* 235.3 (1990), pp. 399–411. ISSN: 0370-2693. DOI: https://doi.org/10.1016/0370-2693(90)91984-J. URL: http://www.sciencedirect.com/science/article/pii/037026939091984J.

[Dre+13a] G. Drexlin et al. "Current Direct Neutrino Mass Experiments". In: *Advances in High Energy Physics* 2013 (2013). DOI: 10.1155/2013/293986.

[Dre+13b] G. Drexlin et al. "Current direct neutrino mass experiments". In: *Adv. High Energy Phys.* 2013 (2013), p. 293986. DOI: 10.1155/2013/293986. arXiv: 1307.0101 [physics.ins-det].

[DSc03] E. Rutherford M.A. D.Sc. "XV. The magnetic and electric deviation of the easily absorbed rays from radium". In: *The London, Edinburgh, and Dublin Philosophical Magazine and Journal of Science* 5.26 (1903), pp. 177–187. DOI: 10.1080/14786440309462912. eprint: https://doi.org/10.1080/14786440309462912. URL: https://doi.org/10.1080/14786440309462912.

[Ell18] Enrico Ellinger. *CAD drawing of board shielding*. CAD drawing. 2018.

[Ell19] Enrico Ellinger. "Development and investigation of the Forward Beam Monitor for the KATRIN experiment". Unpublished doctoral dissertation. 2019.

[Fer34] E. Fermi. "Versuch einer Theorie der β-Strahlen. I". In: *Zeitschrift für Physik* 88.3 (Mar. 1934), pp. 161–177. ISSN: 0044-3328. DOI: 10.1007/BF01351864. URL: https://doi.org/10.1007/BF01351864.

[Fuk+96] Y. Fukuda et al. "Solar Neutrino Data Covering Solar Cycle 22". In: *Phys. Rev. Lett.* 77 (9 Aug. 1996), pp. 1683–1686. DOI: 10.1103/PhysRevLett.77.1683. URL: https://link.aps.org/doi/10.1103/PhysRevLett.77.1683.

[Fuk+98] Y. Fukuda et al. "Evidence for Oscillation of Atmospheric Neutrinos". In: *Phys. Rev. Lett.* 81 (8 Aug. 1998), pp. 1562–1567. DOI: 10.1103/PhysRevLett.81.1562. URL: https://link.aps.org/doi/10.1103/PhysRevLett.81.1562.

[Fur+17] Daniel Furse et al. "Kassiopeia: a modern, extensible C++ particle tracking package". In: *New J. Phys.* 19.5 (2017), p. 053012. DOI: 10.1088/1367-2630/aa6950. arXiv: 1612.00262. URL: http://stacks.iop.org/1367-2630/19/i=5/a=053012.

[Fur15] Daniel Furse. "Techniques for direct neutrino mass measurement utilizing tritium β-decay". PhD thesis. Massachusetts Institute of Technology, 2015. URL: http://hdl.handle.net/1721.1/99313.

[Gan+16] A. Gando et al. "Search for Majorana Neutrinos Near the Inverted Mass Hierarchy Region with KamLAND-Zen". In: *Phys. Rev. Lett.* 117 (8 Aug. 2016), p. 082503. DOI: 10.1103/PhysRevLett.117.082503. URL: https://link.aps.org/doi/10.1103/PhysRevLett.117.082503.

[GGS58] M. Goldhaber, L. Grodzins, and A. W. Sunyar. "Helicity of Neutrinos". In: *Phys. Rev.* 109 (3 Feb. 1958), pp. 1015–1017. DOI: 10.1103/PhysRev.109.1015. URL: https://link.aps.org/doi/10.1103/PhysRev.109.1015.

[Gro15] Stefan Groh. "Modeling of the response function and measurement of transmission properties of the KATRIN experiment". PhD thesis. Karlsruher Institut für Technologie (KIT), 2015. URL: http://nbn-resolving.org/urn:nbn:de:swb:90-465464.

[Hac17] Moritz Thomas Hackenjos. "KATRIN "First Light" - Commissioning and Modelling of the Beamline". PhD thesis. Karlsruher Institut für Technologie (KIT), 2017. 170 pp. DOI: 10.5445/IR/1000078933.

[Ham+99] W. Hampel et al. "GALLEX solar neutrino observations: results for GALLEX IV". In: *Physics Letters B* 447.1 (1999), pp. 127–133. ISSN: 0370-2693. DOI: https://doi.org/10.1016/S0370-2693(98)01579-2. URL: http://www.sciencedirect.com/science/article/pii/S0370269398015792.

[Ham11] Hamamatsu. *Si PIN photodiode S5971, S5972, S5973 series*. 2011. URL: https://www.hamamatsu.com/resources/pdf/ssd/s5971_etc_kpin1025e.pdf (visited on 10/08/2018).

[Hei15] Johannes Heizmann. "Modeling of inelastic electron-hydrogen scattering and of the energy loss function of 18.6 keV electrons for the KATRIN experiment". Bachelor Thesis. Karlsruher Institut für Technologie (KIT), 2015.

[Hei18] Florian Heizmann. "Analysis tools and methods for tritium data taking with the KATRIN experiment". PhD thesis. Karlsruhe Institut für Technologie, 2018. URL: tbd.

[HH76] T. Hsu and J. L. Hirshfield. "Electrostatic energy analyzer using a nonuniform axial magnetic field". In: *Review of Scientific Instruments* 47.2 (1976), pp. 236–238. DOI: 10.1063/1.1134594. URL: https://doi.org/10.1063/1.1134594.

[Höt12] Markus Hötzel. "Simulation and analysis of source-related effects for KATRIN". PhD thesis. Karlsruhe Institut für Technologie, 2012. URL: http://nbn-resolving.org/urn:nbn:de:swb:90-312594.

[Hug08] Karen Hugenberg. "Design of the electrode system of the KATRIN main spectrometer". Diploma Thesis. Westfälische Wilhelms-Universität Münster, 2008. URL: http://www.uni-muenster.de/Physik.KP/AGWeinheimer/theses/Diplom_Karen_Hugenberg.pdf.

[Jun15] Thiago Junqueira de Castro Bezerra. *Double Chooz and Reactor Neutrino Oscillation Elektronische Ressource: θ_{13} Improvement and First Effective Δm^2_{31} Measurement*. Springer Theses, Recognizing Outstanding Ph.D. Research. Tokyo: Springer Japan, 2015. ISBN: 978-4-431-55375-5. DOI: 10.1007/978-4-431-55375-5.

[KAT05] KATRIN collaboration. *KATRIN Design Report*. FZKA scientific report 7090. 2005. arXiv: hep-ex/0109033. URL: http://bibliothek.fzk.de/zb/berichte/FZKA7090.pdf.

[KG17] M. Klein and F. Glück. "Tritium ion blocking and detection in the KATRIN experiment". In: *J. Phys: Conf. Ser.* 888 (2017), p. 012073. DOI: 10.1088/1742-6596/888/1/012073.

[Kle+18] M. Kleesiek et al. "β-Decay Spectrum, Response Function and Statistical Model for Neutrino Mass Measurements with the KATRIN Experiment". In: (2018). arXiv: 1806.00369 [physics.data-an].

[Kle14] Marco Kleesiek. "A Data-Analysis and Sensitivity-Optimization Framework for the KATRIN Experiment". PhD thesis. Karlsruhe Institut für Technologie, 2014. URL: https://publikationen.bibliothek.kit.edu/1000043301/3232293.

[Kle18] Manuel Klein. "Tritium ions in the KATRIN experiment: detection, blocking and removal". Unpublished doctoral dissertation. 2018.

[Kod+01] K. Kodama et al. "Observation of tau neutrino interactions". In: *Physics Letters B* 504.3 (2001), pp. 218–224. ISSN: 0370-2693. DOI: https://doi.org/10.1016/S0370-2693(01)00307-0. URL: http://www.sciencedirect.com/science/article/pii/S0370269301003070.

[KR83] P Kruit and F H Read. "Magnetic field paralleliser for 2π electron-spectrometer and electron-image magnifier". In: *Journal of Physics E: Scientific Instruments* 16.4 (Apr. 1983), pp. 313–324. DOI: 10.1088/0022-3735/16/4/016. URL: https://doi.org/10.1088%2F0022-3735%2F16%2F4%2F016.

[Kra+05] C. Kraus et al. "Final results from phase II of the Mainz neutrino mass search in tritium β decay". In: *Eur. Phys. J. C* 40.4 (2005), pp. 447–468. DOI: 10.1140/epjc/s2005-02139-7. arXiv: hep-ex/0412056.

[Kuc+18a] Laura Kuckert et al. "Modelling of gas dynamical properties of the KATRIN tritium source and implications for the neutrino mass measurement". In: (2018). arXiv: 1805.05313 [physics.ins-det].

[Kuc+18b] Laura Kuckert et al. "Modelling of gas dynamical properties of the Katrin tritium source and implications for the neutrino mass measurement". In: *Vacuum* 158 (2018), pp. 195–205. ISSN: 0042-207X. DOI: https://doi.org/10.1016/j.vacuum.2018.09.036. URL: http://www.sciencedirect.com/science/article/pii/S0042207X18310972.

[Kuc16] Laura Kuckert. "The Windowless Gaseous Tritium Source of the KATRIN Experiment - Characterisation of Gas Dynamical and Plasma Properties". 51.03.01; LK 01. PhD thesis. Karlsruher Institut für Technologie (KIT), 2016. 296 pp. DOI: 10.5445/IR/1000065077.

[KZ97] Hans V. (1942-) Klapdor-Kleingrothaus and Kai (1963-) Zuber. *Teilchenastrophysik: mit Tabellen*. Teubner-Studienbücher. Physik. Stuttgart: Teubner, 1997. ISBN: 3-519-03094-2.

[LP00] L L. Lucas and M P. Unterweger. "Comprehensive Review and Critical Evaluation of the Half-Life of Tritium". In: *Journal of Research of the National Institute of Standards and Technology* 105 (July 2000). DOI: 10.6028/jres.105.043.

[LS85] V.M. Lobashev and P.E. Spivak. "A method for measuring the electron antineutrino rest mass". In: *Nuclear Instruments and Methods in Physics Research Section A: Accelerators, Spectrometers, Detectors and Associated Equipment* 240.2 (1985), pp. 305–310. ISSN: 0168-9002. DOI: https://doi.org/10.1016/0168-9002(85)90640-0. URL: http://www.sciencedirect.com/science/article/pii/0168900285906400.

[Mat18] MatWeb. *Material Property Data*. 2018. URL: http://www.matweb.com (visited on 09/01/2018).

[MS87] Stanislav P Mikheev and A Yu Smirnov. "Resonance oscillations of neutrinos in matter". In: *Soviet Physics Uspekhi* 30.9 (Sept. 1987), pp. 759–790. DOI: 10.1070/pu1987v030n09abeh002961.

[NVI19] NVIDIA. *NVIDIA Tesla Series*. 2019. URL: https://www.nvidia.com/en-us/data-center/tesla/ (visited on 03/17/2019).

[OW08] E. W. Otten and C. Weinheimer. "Neutrino mass limit from tritium beta decay". In: *Rept. Prog. Phys.* 71 (2008), p. 086201. DOI: 10.1088/0034-4885/71/8/086201. arXiv: 0909.2104 [hep-ex].

[PAC15] L. Pandola, C. Andenna, and B. Caccia. "Validation of the Geant4 simulation of bremsstrahlung from thick targets below 3MeV". In: *Nuclear Instruments and Methods in Physics Research Section B: Beam Interactions with Materials and Atoms* 350 (2015), pp. 41–48. ISSN: 0168-583X. DOI: https://doi.org/10.1016/j.nimb.2015.03.033. URL: http://www.sciencedirect.com/science/article/pii/S0168583X15002335.

[Par08] Stephen J. Parke. "CP Violation in the Neutrino Sector". In: *Proceedings, 6th Conference on Flavor Physics and CP Violation (FPCP 2008): Taipei, Taiwan, May 5-9, 2008*. 2008. arXiv: 0807.3311 [hep-ph]. URL: http://lss.fnal.gov/cgi-bin/find_paper.pl?conf-08-248.

[Par18] Diana Parno. *KATRIN: Toward a High-Precision Neutrino-Mass Determination with Tritium*. 2018. URL: https://doi.org/10.5281/zenodo.1287933.

[Pau30] Wolfgang Pauli. "Offener Brief an die Gruppe der Radioaktiven bei der Gauvereins-Tagung zu Tübingen". In: *Physikalisches Institut der Eidg. Technischen Hochschule* (Dec. 1930). URL: http://www.symmetrymagazine.org/sites/default/files/legacy/pdfs/200703/logbook_letter.pdf.

[Pic+92] A. Picard et al. "A solenoid retarding spectrometer with high resolution and transmission for keV electrons". In: *Nuclear Instruments and Methods in Physics Research Section B: Beam Interactions with Materials and Atoms* 63.3 (1992), pp. 345–358. ISSN: 0168-583X. DOI: https://doi.org/10.1016/0168-583X(92)95119-C. URL: http://www.sciencedirect.com/science/article/pii/0168583X9295119C.

[Pon68] B. Pontecorvo. "Neutrino Experiments and the Problem of Conservation of Leptonic Charge". In: *Sov. Phys. JETP* 26 (1968), pp. 984–988. URL: http://jetp.ac.ru/cgi-bin/dn/e_026_05_0984.pdf.

[Rei+60] F. Reines et al. "Detection of the Free Antineutrino". In: *Phys. Rev.* 117 (1 Jan. 1960), pp. 159–173. DOI: 10.1103/PhysRev.117.159. URL: https://link.aps.org/doi/10.1103/PhysRev.117.159.

[Ren11] Pascal Renschler. "KESS - A new Monte Carlo simulation code for low-energy electron interactions in silicon detectors". PhD thesis. Karlsruhe Institut für Technologie, 2011. URL: http://nbn-resolving.org/urn:nbn:de:swb:90-249597.

[Rod11] Werner Rodejohann. "Neutrino-less Double Beta Decay and Particle Physics". In: *Int. J. Mod. Phys.* E20 (2011), pp. 1833–1930. DOI: 10.1142/S0218301311020186. arXiv: 1106.1334 [hep-ph].

[Sch+11] M. Schlösser et al. "Design Implications for Laser Raman Measurement Systems for Tritium Sample-Analysis, Accountancy or Process-Control Applications". In: *Fusion Science and Technology* 60.3 (2011), pp. 976–981. URL: http://www.ans.org/pubs/journals/fst/a_12579.

[Sch16] Kerstin Schönung. "Development of a Rear Wall for the KATRIN Rear Section and investigation of tritium compatibility of Rear Section components". PhD thesis. Karlsruher Institut für Technologie, 2016. URL: http://nbn-resolving.org/urn:nbn:de:swb:90-560776.

[Sch17] Simon Schubotz. "Untersuchung des Magnetfeldes der kryogenen Pumpstrecke des KATRIN-Experiments mittels des Forward Beam Monitors". Bachelor Thesis. Bergische Universität Wuppertal (BUW), 2017.

[Sco35] F. A. Scott. "Energy Spectrum of the Beta-Rays of Radium E". In: *Phys. Rev.* 48 (5 Sept. 1935), pp. 391–395. DOI: 10.1103/PhysRev.48.391. URL: https://link.aps.org/doi/10.1103/PhysRev.48.391.

[SFS06] Francesc Salvat, José Fernández-Varea, and Josep Sempau. "PENELOPE2008: A Code System for Monte Carlo Simulation of Electron and Photon Transport". In: (July 2006).

[SL18a] Martin Slezák and Alexey Lokhov. *A model for a keV-scale sterile neutrino search with KATRIN: SSC-sterile*. 2018. URL: https://doi.org/10.5281/zenodo.1300735.

[SL18b] Martin Slezák and Alexey Lokhov. *Discussion on Response-Matrix method*. personal communication. 2018.

[Stu18] Michael Sturm. *Built-in Valve V0 in WGTS*. personal communication. 2018.

[Sue15] Fumihiko Suekane. *Neutrino Oscillations Elektronische Ressource: A Practical Guide to Basics and Applications*. Lecture Notes in Physics, Teil 898. Tokyo: Springer Japan, 2015. ISBN: 978-4-431-55462-2. DOI: 10.1007/978-4-431-55462-2.

[Tan+18] M. Tanabashi et al. "Review of Particle Physics". In: *Phys. Rev. D* 98 (3 Aug. 2018), p. 030001. DOI: 10.1103/PhysRevD.98.030001. URL: https://link.aps.org/doi/10.1103/PhysRevD.98.030001.

[Taw+90] H. Tawara et al. "Cross Sections and Related Data for Electron Collisions with Hydrogen Molecules and Molecular Ions". In: *Journal of Physical and Chemical Reference Data* 19.3 (1990), pp. 617–636. DOI: 10.1063/1.555856. eprint: https://doi.org/10.1063/1.555856. URL: https://doi.org/10.1063/1.555856.

[VAT18] VAT. *UHV gate valve, Series 108, DN 250 (ID 10")*. 2018. URL: http://www.vatvalve.com/business/valves/product?id=10848-CE24 (visited on 09/01/2018).

[Ver78] J. Verner. "Explicit Runge–Kutta Methods with Estimates of the Local Truncation Error". In: *SIAM Journal on Numerical Analysis* 15.4 (1978), pp. 772–790. DOI: 10.1137/0715051. eprint: https://doi.org/10.1137/0715051. URL: https://doi.org/10.1137/0715051.

[Wal+14] B. L. Wall et al. "Dead layer on silicon p–i–n diode charged-particle detectors". In: *Nucl. Instrum. Meth.* A744 (2014), pp. 73–79. DOI: 10.1016/j.nima.2013.12.048. arXiv: 1310.1178 [physics.ins-det].

[Wan13] Nancy Wandkowsky. "Study of background and transmission properties of the KATRIN spectrometers". PhD thesis. Karlsruher Institut für Technologie (KIT), 2013. URL: http://nbn-resolving.org/urn:nbn:de:swb:90-366316.

[Wol78] L. Wolfenstein. "Neutrino oscillations in matter". In: *Phys. Rev. D* 17 (9 May 1978), pp. 2369–2374. DOI: 10.1103/PhysRevD.17.2369. URL: https://link.aps.org/doi/10.1103/PhysRevD.17.2369.

[Zub04] Kai (1963-) Zuber. *Neutrino physics*. Series in high energy physics, cosmology and gravitation. New York u.a.: Taylor and Francis, 2004. ISBN: 0-7503-0750-1;; 978-07503-0750-5.

LIST OF FIGURES

LIST OF TABLES

ACRONYMS AND ABBREVIATIONS

CKrS Condensed Krypton Source

CPS Cryogenic Pumping Section

CPU Central Processing Unit

DPS Differential Pumping Section

FBM Forward Beam Monitor

FPD Focal Plane Detector

FSD Final State Distribution

FT First Tritium (configuration)

GEANT Geometry and Tracking

GPGPU General Purpose Computation on Graphics Processing Unit

GPU Graphics Processing Unit

KASPER KATRIN analysis and simulation package

KATRIN Karlsruhe Tritium Neutrino

KESS KATRIN Electron Scattering in Silicon

KIT Karlsruhe Institute of Technology

MAC-E Magnetic-Adiabatic-Collimation with an Electrostatic filter

MC Monte-Carlo

MS Main-Spectrometer

MoS Monitor-Spectrometer

NK Nominal Katrin (configuration)

***p*-*i*-*n*-diode** positive intrinsic negative diode

PMNS Pontecorvo-Maki-Nakagawa-Sakata

PS Pre-Spectrometer

RS Rear-Section

RSCM Rear-Section Magnet

RW Rear-Wall

SSC Source and Spectrum Calculations

SM Standard Model

Source Windowless Gaseous Tritium Source

TLK Tritium Laboratory Karlsruhe

TS Transport-Section

WGTS Windowless Gaseous Tritium Source